# Study of Proton Irradiated 56/44 mol% P(VDF-TrFE) and P(VDF-TrFE) MEMS Transducers

Submitted by

**Lam Tin Yan**

A thesis submitted in partial fulfilment of the requirements for the Degree of Master of Philosophy in Applied Physics

At

Department of Applied Physics

The Hong Kong Polytechnic University

June 2005

# Certificate of Originality

I hereby declare that this thesis is my own work and that, to the best of my knowledge and belief, it reproduces no material previously published or written, nor material that has been accepted for the award of any other degree or diploma, except where due acknowledgement has been made in the text.

_____(Signed)

_____LAM TIN YAN_____(Name of student)

# Abstract

Polyvinylidene fluoride-trifluoroethylene [P(VDF-TrFE)] is a well-known ferroelectric polymer. As it is easily processed, lightweight, mechanically flexible and can conform to any shapes and surfaces, it has been studied for nearly three decades for applications in electromechanical devices. In recent years, irradiation treatment in polymeric materials has attracted considerable interest as it can change both the structures and properties of the materials significantly and makes them useful for specific applications.

In this project, proton irradiation with doses of 10-50 Mrad was carried out to investigate the potential for modifying the properties of P(VDF-TrFE). Copolymer films with VDF contents of 56 mol% were prepared by hot pressing. The effects of irradiation on both structures and properties of the copolymer were investigated by studying the change in lattice spacing, phase transitional behaviour, relative permittivity and electric field induced strain. It was found that irradiation can convert the copolymer from a ferroelectric to a relaxor material and the improved electrostrictive coefficients $M_{33}$ made the proton irradiated P(VDF-TrFE) a potential candidate for sensor and actuator applications.

The application of P(VDF-TrFE) films in the fabrication of microelectromechanical systems (MEMS) devices was investigated. 56/44 mol%

P(VDF-TrFE) was spin-coated on a silicon wafer containing a layer of thermally oxidized silicon dioxide. The $SiO_2$/Si was back-etched to produce a membrane structure. Some of the 56/44 mol% P(VDF-TrFE) MEMS were also subjected to proton irradiation with doses of 10-50 Mrad and their effective electrostrictive coefficient $M_{33}$ was compared with that of free bulk P(VDF-TrFE) thick films. The clamping effect of substrate reduces the $M_{33}$ but the bending effect of the Si membrane enhances the mechanical properties.

Micromachined piezoelectric 70/30 mol% P(VDF-TrFE) MEMS for air transducer application was prepared. The mechanical behaviour of the MEMS was analysed by means of a laser vibrometer. The resonance frequency was found to depend on the structure and the thickness of the membrane. Both the transmitting and receiving acoustic responses of the copolymer MEMS were studied. The result suggested that the piezoelectric P(VDF-TrFE) has potential applications as actuators and in monitoring ultrasound emission.

# Publications

Lam, T.Y., Lau, S.T., Chan, H.L.W., Choy, C.L., Cheung, W.Y. and Wong, S.P. "Modification of the structure and properties of P(VDF-TrFE) 56/44 mol% copolymer by proton irradiation treatment", *Journal of Polymer Science Part B: Polymer Physics*, *43*(17), pp. 2334-2339 (2005).

Lam, T.Y., Lam, K.H. and Chan, H.L.W. "Micromachined piezoelectric polymer membrane acoustic sensor", *Integrated Ferroelectrics*, submitted (2005).

# Acknowledgements

First of all, I would like to express my gratitude to my supervisor Prof. H. L. W. Chan for giving me an opportunity to study on this project. It has been thoroughly enjoyable and a great learning experience. Her guidance, valuable comments on my work and encouragement have helped me overcome many difficulties in my study. I would like to thank Prof. C. L. Choy for providing me with valuable suggestions and comments on my paper.

I would like to thank Dr. W. Y. Cheung, Department of Electronic Engineering, The Chinese University of Hong Kong, for his assistance in the proton irradiation of copolymer samples.

I also wish to express my appreciation for the help provided by all my colleagues, namely Dr. S.T. Lau, Mr. K.H. Lam, Mr. S.H. Choy, Ms. Y.L. Cheng and Ms. M.K. Cheung.

The financial support provided by Hong Kong Research Grants Council is gratefully acknowledged. Finally, I would like to thank my parents and friends for their support and encouragement over the past two years.

# Table of Contents

# List of Figures

# List of Tables

# Chapter 1

# Introduction

## 1.1 Motivation

Airborne ultrasonic transducers are widely used in many measurement tasks in automation, surveillance, gas flow measurement, and distance measurement [Manthey et al., 1992]. Recently, silicon micromachining technology has been explored to fabricate various ultrasonic devices based on microelectromechanical systems (MEMS) as it has the following advantages: potentially low cost due to the batch processing nature, possibility of integrating transducers and circuits on a single chip, amenable to size miniaturization, etc.

In existing ultrasonic measurement systems for industrial purposes, piezoelectric ceramics, such as lead zirconate titanate (PZT) and zinc oxide are often used. However, some distinct properties of the piezoelectric polymers (Table 1.1) make them uniquely qualified when ceramics is incapable of performing as effectively, for example, use polymer to fill hollow areas. As noted in Table 1.1, for polymers such as polyvinylidene fluoride (PVDF) and polyvinylidene fluoride-trifluoroethylene [P(VDF-TrFE)], the piezoelectric strain coefficient $d_{31}$ is lower than that of piezoelectric ceramics. However, piezoelectric polymers have much higher piezoelectric voltage

coefficient $g_{31}$ indicating that they are much better receiving sensors than ceramics. Piezoelectric polymeric sensors and actuators offer the advantage of processing flexibility because they are lightweight, tough and can be readily manufactured into large area and complex shapes. Polymers also feature in low dielectric constant, low elastic stiffness, and low density, giving rise to a high voltage sensitivity (excellent sensor characteristics), and low acoustic and mechanical impedance (crucial for medical and underwater applications). Polymers also typically possess a high dielectric breakdown and high operating field strength, which means that they can withstand a much higher driving field than ceramics. Hence, there is an interest in extending the study to modified P(VDF-TrFE) and attempt to incorporate the copolymer into MEMS devices.

Table 1.1 Comparison of some properties in PVDF, P(VDF-TrFE) and PZT [Ohigashi et al., 1984; Manthey et al., 1992; Ito, Y. et al., 1999; Furukawa, T. et al., 1990].

| | **75/25 mol% P(VDF-TrFE)** | **PVDF** | **PZT-4** |
|---|---|---|---|
| **Piezoelectric coefficient $d_{31}$ (pC/N)** | 12.5 | 25 | -123 |
| **Piezoelectric coefficient $g_{31}$ (Vm/N)** | 0.24 | 0.24 | 0.011 |
| **Piezoelectric coefficient $d_{33}$ (pC/N)** | 33 | 39 | 289 |
| **Piezoelectric coefficient $g_{33}$ (Vm/N)** | 0.38 | 0.32 | 0.025 |
| **Elastic constant $c_{33}^{D}$ ($10^9$ N/m$^2$)** | 11.3 | 9.1 | 159 |
| **Electrostrictive coefficient $Q_{33}$ (m$^4$/C$^2$)** | -2.5 * | -2.4 + | 0.03 |

* 65/35 mol% P(VDF-TrFE), + drawn PVDF

## 1.2 Background

Piezoelectric and electrostrictive materials are important constituents of electromechanical sensors and actuators. Actuators make use of the strain response of ferroelectric materials under high electric fields. Hence, a short introduction to piezoelectricity and electrostriction will be given.

### 1.2.1 Piezoelectricity and Electrostriction

Piezoelectricity was discovered by the brothers Pierre Curie and Paul-Jacques Curie in 1880.

Piezoelectric materials can become electrically charged when subjected to a mechanical stress. These materials also show the converse piezoelectric effect and undergo mechanical deformation upon the application of an electric field. The discovery of electromechanical properties in piezoelectric materials allowed for their utilization in transducer applications.

In transducer applications, the direct piezoelectric effect which relates polarization to stress is used in sensors while the converse piezoelectric effect which relates strain to electric field is used in actuators.

For a piezoelectric disc of a given thickness $t$, the voltage $V$ generated across the electrodes of the disc when subjected to a stress $T$ is:

$$V = gtT \tag{1. 1}$$

where $g$ is the piezoelectric voltage coefficient, which shows the ability of the material to generate a charge or electric field when subjected to a stress. Piezoelectric sensing is

mostly used in sensors such as pressure sensors, force sensors, velocity and accelerometers, hydrophones, microphones, etc. [Jones et al., 1996].

In actuator applications, the converse piezoelectric effect is utilized. For a piezoelectric disc with a polarization direction along the thickness direction of the disc, the change in diameter ($\Delta D_{disc}$) under a given applied voltage $V$ is expressed as follows:

$$\Delta D_{disc} = d_{31} V \frac{D_{disc}}{t} \qquad (1.2)$$

where $d$ is the piezoelectric coefficient denoted by the change in strain of the piezoelectric material as a function of the applied electric field. These changes in dimension can be utilized in actuators, underwater transducer, air transducer, ink jet printers, etc.

The electrostrictive effect is, as with piezoelectricity, a means by which an electrical input can be converted into a mechanical output. Electrostriction is present in all solid state substances.

The main difference between electrostrictive and piezoelectric material is that piezoelectric materials display a strain which is directly proportional to the applied field. Piezoelectricity is a third-rank tensor that relates strain and electric field. In electrostrictive materials, the strain is proportional to the square of the applied field.

Electrostriction is a fourth-rank tensor that relates strain to the square of electric field, and is defined by the following relationship:

$$x_{ij} = M_{ijmn} E_m E_n \tag{1. 3}$$

or

$$x_{ij} = Q_{ijmn} P_m P_n \tag{1. 4}$$

where $E_m E_n$ and $P_m P_n$ are components of the electric field and polarization, respectively. $M_{ijmn}$ are elements of the fourth rank field related electrostriction tensor, and $Q_{ijmn}$ are elements of the fourth rank polarization related electrostriction tensor. Conversion between the two coefficients are carried out using the field polarization relationships $P_m = \eta_{mn} E_n$ and $E_n = \chi_{mn} P_m$ where $\eta_{mn}$ is the dielectric susceptibility tensor, and $\chi_{mn}$ is the inverse dielectric susceptibility tensor.

The $M$ coefficient is defined in unit of $m^2/V^2$. Their values range from about $10^{-24}$ $m^2/V^2$ in low-permittivity materials to $10^{-16}$ $m^2/V^2$ in high-permittivity actuator materials including relaxor ferroelectrics such as lead magnesium niobate-lead titanate. $Q$ coefficients are defined in units of $m^4/C^2$. $Q$ ranges from $10^{-3}$ $m^4/C^2$ in relaxor ferroelectrics to greater than the order of $10^3$ $m^4/C^2$ in polyurethane films [Newnham et al., 1997].

### 1.2.2 Microelectromechanical Systems (MEMS)

#### 1.2.2.1 Background

Success in the semiconductor industry has introduced a new type of sensor and actuator based on the microelectromechanical systems (MEMS) technology. The term MEMS has become synonymous with many types of micro-fabricated devices. It is fabricated like integrated circuits with micro-mechanical structures which can act as sensing and actuating components.

#### 1.2.2.2 Classification of MEMS Devices

Before the realization of adapted user-defined designs, the technological feasibility is usually demonstrated by making some generic structures, which can be modeled by analytical methods. The most common MEMS structures are cantilever beams (clamped only at one side), bridges (clamped at two sides) and the diaphragms (clamped on all the periphery) as shown in Figure 1.1. The square diaphragm is easy to make on anisotropic silicon, especially by wet etching. Each structure has its own displacement pattern and resonance frequency. Each mode type may have several higher order resonance frequencies.

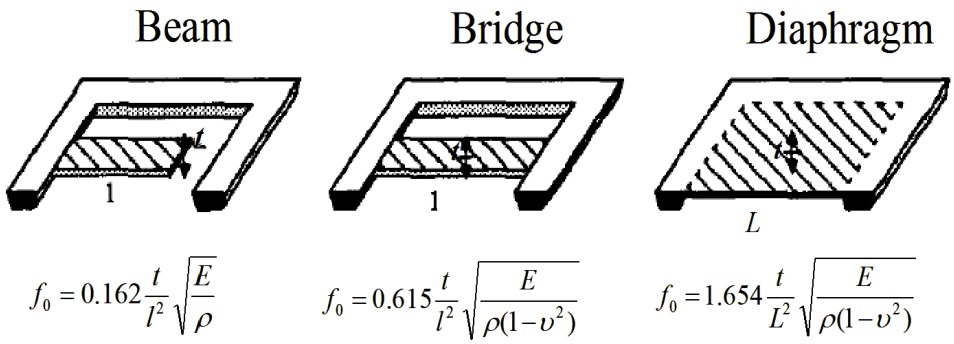


Figure 1.1 The 3 generic structures for MEMS [Stemme, 1991] and their fundamental flexural resonance frequencies, where $E$ is the Young's modulus, $\rho$ the density and $\nu$ is the Poisson's ratio.

These three structures provide some feasible designs for microsensors and actuators which can perform the desired task in most smart structures. Bulk micromachined pressure sensors represent one of the most successful silicon sensors on the market. They are usually fabricated using a simple membrane. Microphones are a particular type of MEMS pressure sensor designed to convert acoustic signals into electrical output. The distinction between various types of microphones is typically based upon the sensing technology used to detect the membrane displacements. They can be classified into capacitive [Kronast et al., 2001], electret [Hsieh et al., 1997], piezoresistive [Kälvesten et al., 1995] and piezoelectric microphones.

Piezoelectric microphones utilize a thin-film piezoelectric layer deposited on the top surface of a structure sensitive to acoustic pressure. The strain obtained in a piezoelectric material is relatively small (with strain of ~ 0.1-0.2 % in one direction).

With the use of a flexible backing plate, it can generate a considerable displacement, especially at resonance. The principle of operation is as follows: If the piezoelectric material is driven by an electrical signal, it expands and contracts in the rhythm of the driving signal, if it is free. As the piezoelectric material is attached to a backing plate, it exerts forces and moments, which bends and elongates or contracts the plate. For example, the transverse extension of the piezoelectric material (using $d_{31}$ mode) generates a flexing movement in the structure, allowing a contribution to the induced charge through strain in the membrane. If it is driven at the fundamental resonance frequency of the diaphragm, the output signal becomes very large.

Microphones can be designed based on piezoelectric sensing techniques. In recent years, there is increased interest in integrating ferroelectric films on silicon substrates for potential applications in MEMS. Ko et al. [2003] fabricated a membrane based device containing a bulk etched silicon nitride membranes with thin film ZnO and Al electrodes. Bernstein et al. [1997] fabricated a micromachined ferroelectric transducer using a boron-doped etch stop defined diaphragm coated with a sol-gel layer of PZT. For piezoelectric polymer, Schellin et al. [1994] used a spin-coating technique to fabricate a membrane-based P(VDF-TrFE) microphone.

## 1.3 Literature Review

A piezoelectric thin film is at the heart of the piezoelectric MEMS sensor or actuator. An understanding of the development of the properties of the P(VDF-TrFE) copolymer is necessary.

In 1969 Professor Kawai reported a large piezoelectric effect in stretched polyvinylidene fluoride (PVDF), [Kawai, 1969] which is a well-known semicrystalline polymer with approximately equal proportions of random stacks of amorphous and crystalline lamellae. The crystal structure of PVDF is dependent on the molecular conformation and packing mode. Four types of crystal structures designated as forms β,α, δ and γ (or forms I, II, $II_p$ and III) were found (as shown in Figure 1.2), where *T* and *G* denote the trans planar isomer and gauche non-planar isomer, respectively. Melt-crystallization of PVDF produces the most stable structure: nonpolar α phase which consists of $TGT\overline{G}$ molecules packed in an antiparallel fashion. The morphology of α-PVDF consists of crystallites dispersed within amorphous regions as shown in Figure 1.3. Mechanical orientation, thermal annealing and high voltage treatments have shown to be effective in inducing crystalline phase transformations. For example, polar β-PVDF which contains all-trans conformation and exhibits ferroelectric behaviour, can be induced by mechanical stretching [Furukawa, 1989].

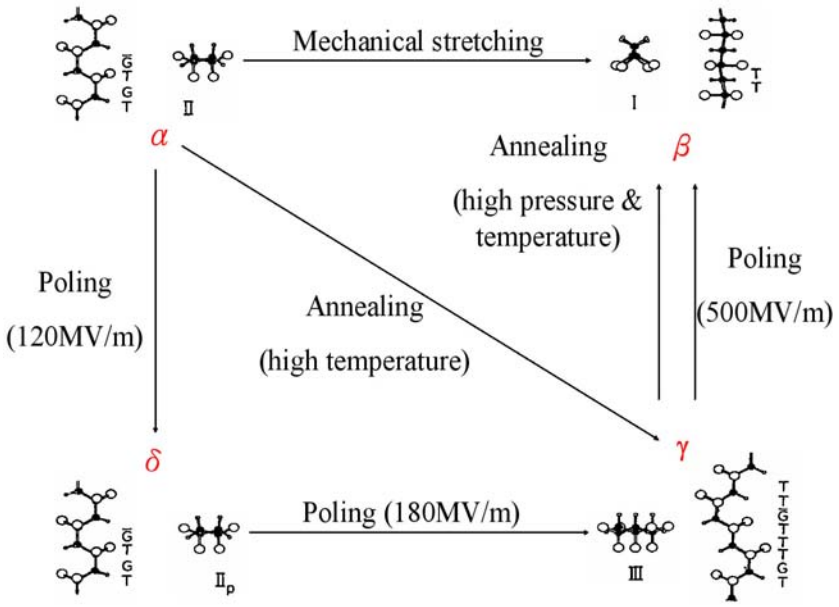


Figure 1.2 A schematic diagram of transformations among the crystalline phases of PVDF due to electrical, mechanical and thermal treatments [Furukawa, 1989; Tashiro et al., 1981].

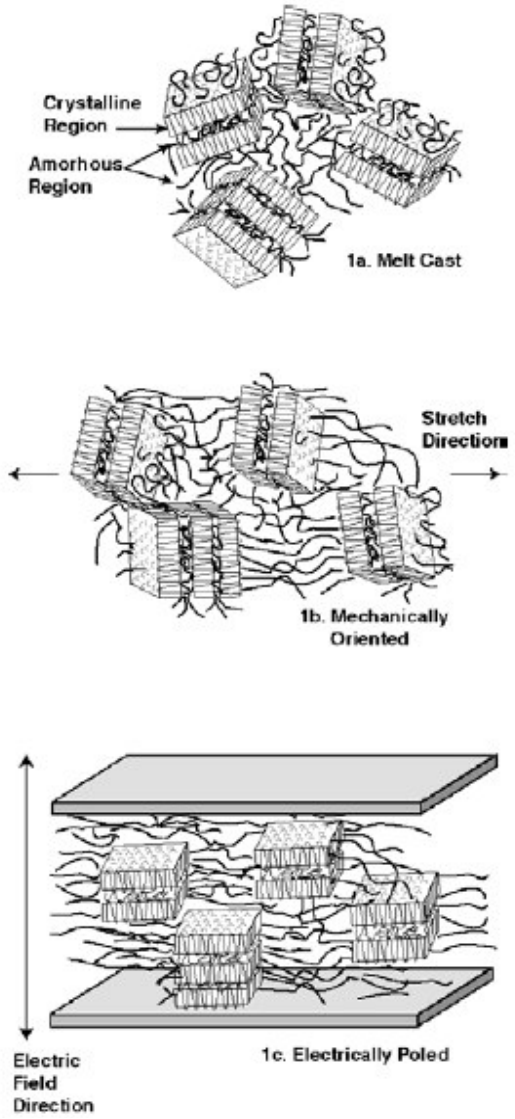


Figure 1.3 Schematic illustration showing random stacks of amorphous and crystalline lamellae in PVDF polymer. (a) morphology of α-PVDF consists of crystallites dispersed within amorphous regions after the film is melt cast; (b) orientation of the film by mechanical stretching to several times its original length aligns the amorphous strands in the plane of the film; (c) electrical poling is accomplished by applying an electric field across the thickness of the polymer to effect crystalline orientation [Harrison et al., 2001].

As PVDF must be mechanically drawn in order to achieve a piezoelectric polar structure, hence it cannot be used in thin film fabrication using the spin-coating technique. Lando et al. [1968] reported in their early work that the introduction of 93 mol% TrFE in PVDF can induce direct crystallization with a somewhat expanded β cell. Later on, Yagi et al. [1980] synthesized P(VDF-TrFE) copolymers over the entire range of compositions. Because of similarity in the size of hydrogen and fluorine atoms, VDF and TrFE units are randomly distributed along the molecular chain to form a random copolymer and cocrystallized into a single crystalline phase analogous to β-PVDF without mechanical drawing. A ferroelectric to paraelectric phase transition exists in copolymers containing 50-85 mol% VDF. The structures and behaviours of these copolymers are strongly influenced by the mol% of VDF. Figure 1.4 shows the phase diagram of P(VDF-TrFE) copolymer.

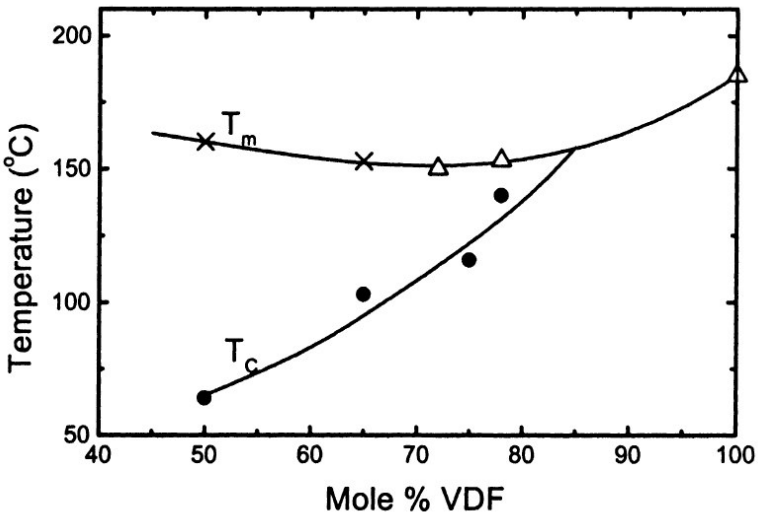


Figure 1.4 Phase diagram of P(VDF-TrFE) copolymer, where $T_m$ and $T_c$ are the melting temperature and ferroelectric to paraelectric (F-P) phase transition temperature, respectively [Cheng et al., 2001].

Electrostriction of P(VDF-TrFE) has been reported by Furukawa et al. [1990], who has revealed that electrostriction is the origin of piezoelectricity and it is the most fundamental mechanism for electromechanical coupling phenomena. Under high field measurement, a butterfly-shape strain-E loop with a D-E hysteresis loop of PVDF and 65/35 mol% P(VDF-TrFE) are observed and shown in Figure 1.5 and Figure 1.6, respectively. The mechanical strain $S$ in the direction of the applied field $E$ and the electric displacement $D$ are described in terms of $S$ against $D^2$, where $Q$ is the electrostrictive coefficient. From Figure 1.7, the slope gives an electrostrictive coefficient $Q_{33}$ of -2.4 $m^4/C^2$ for drawn PVDF and -2.5 $m^4/C^2$ for undrawn 65/35 copolymer. It has been shown that piezoelectricity arises from the electrostriction coupled with the remnant polarization.

$$g_{33} = 2Q_{33}P_r \tag{1. 5}$$

$$d_{33} = 2\varepsilon Q_{33}P_r \tag{1. 6}$$

The origin of piezoelectricity in electrostriction enables us to control the piezoelectric coefficients by an external electric field. Hence, the giant electrostriction in the relaxor ferroelectric copolymers stimulated our interest in the investigation of electric-field-induced piezoelectric activity in the irradiated P(VDF-TrFE) copolymer.

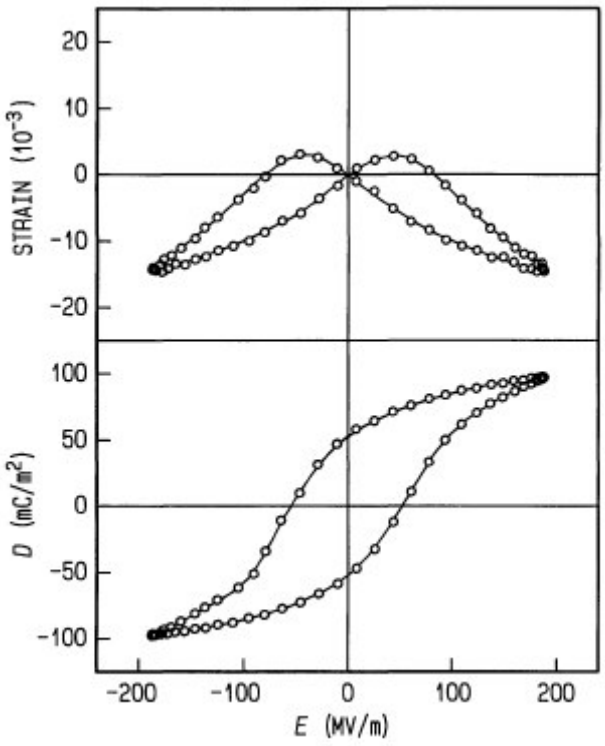


Figure 1.5 Strain-E and D-E hysteresis loops of uniaxially drawn PVDF [Furukawa, 1990].

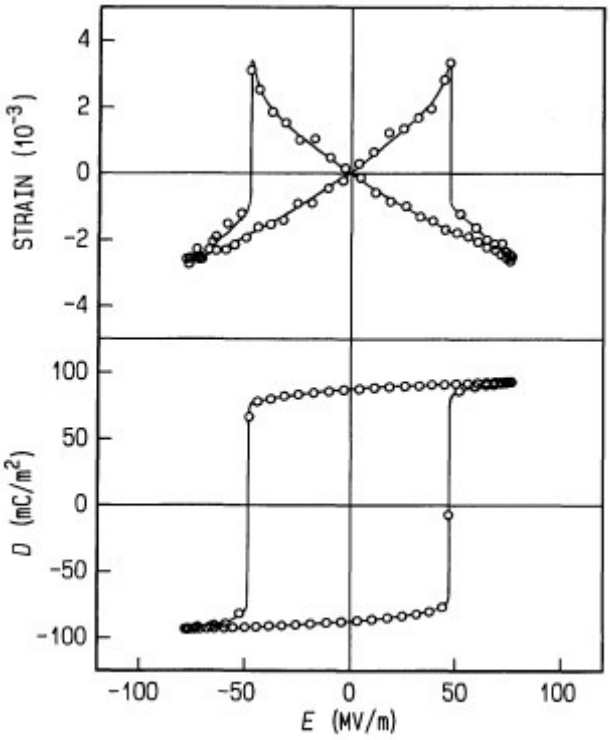


Figure 1.6 Strain-E and D-E hysteresis loops of undrawn 65/35 mol% P(VDF-TrFE) copolymer [Furukawa, 1990].

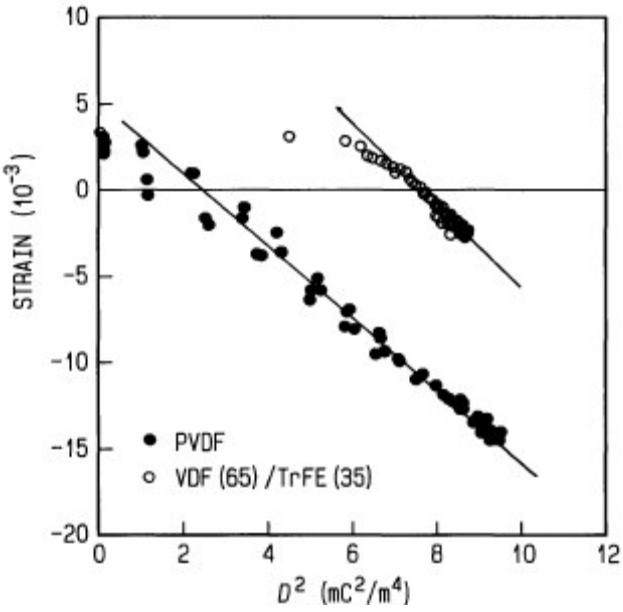


Figure 1.7 Plots of strain S as a function of $D^2$ for PVDF and 65/35 mol% P(VDF-TrFE) copolymer [Furukawa, 1990].

The discovery of electron-induced structural transformation in P(VDF-TrFE) copolymers was reported by Lovinger [1985]. Several research groups have studied the influence of high energy electron or γ-ray irradiation on P(VDF-TrFE) copolymers [Legrand et al., 1995; Bharti et al., 1998; Welter et al., 2003; Tang et al., 2000]. This unique irradiated P(VDF-TrFE) copolymer actuator material has been described in detail in two recent review papers [Cheng et al. 2000; Zhang et al., 1998]. It shows that suitable high-energy electron irradiation treatment can change the polarization as demonstrated in Figure 1.8. The associated longitudinal electrostrictive strain, which accompanies the polarization is shown in Figure 1.9. The resulting material is no longer piezoelectric but rather exhibits a large electric field-induced strain (4% strain) due to electrostriction. The cause of such large electrostriction is the large change in

the lattice constant as the polymer changes from a ferroelectric to a paraelectric phase and because of field-induced expansion and contraction of the polar regions. After irradiation, the material exhibits behaviour analogous to that of a relaxor ferroelectric system in inorganic materials. Dispersion observed in the dielectric response followed the Vogel-Fulcher relation analogous to that in inorganic relaxor systems (Figure 1.10). By drawing the analogy with the structures of the relaxor systems in inorganic materials, Zhang et al. [1998] suggested that electron irradiation introduced defects in the copolymer and broke up the coherent macro-polar regions (the all trans conformation) in the normal ferroelectric phase into nano-polar regions, thereby transforming the copolymer into a relaxor ferroelectric material.

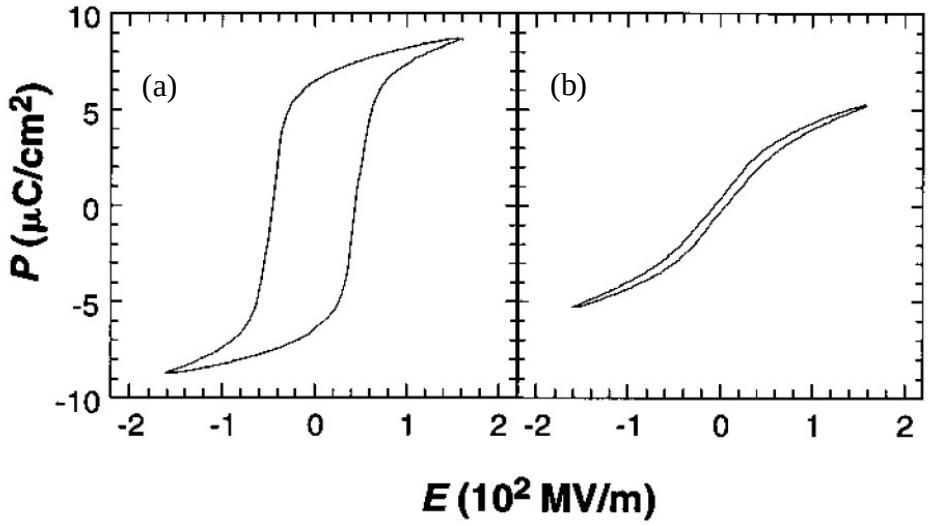


Figure 1.8 The polarization hysteresis loops of P(VDF-TrFE) 50/50 copolymer measured at room temperature: (a) before irradiation and (b) after irradiation with $4 \times 10^5$ Gy at 120 $^{o}$C. $P$ is the polarization and $E$ is the electric field [Zhang et al., 1998].

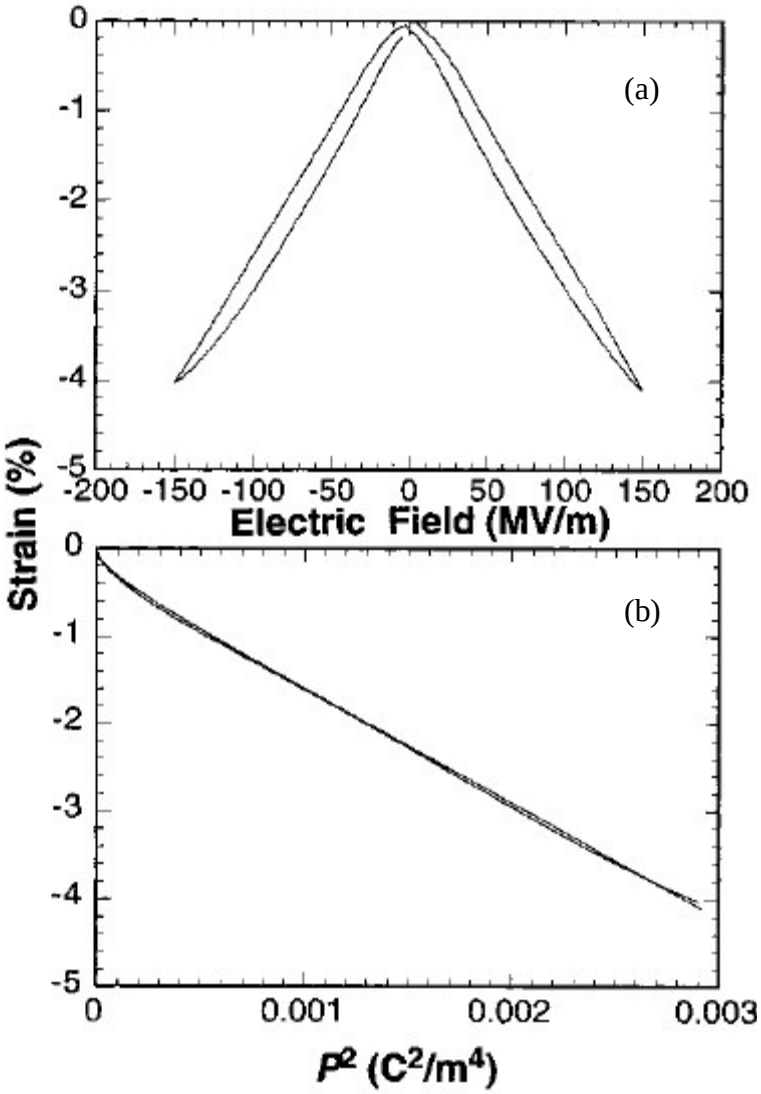


Figure 1.9 (a) The strain-field dependence of P(VDF-TrFE) 50/50 copolymer after irradiation with $4 \times 10^5$ Gy at 120 $^{o}$C. (b) The electrostrictive relation between the strain and polarization, where the strain at $P>0$ and $P<0$ regions are overlapped as a result of the dependence of $P^2$ on the strain. The deviation of the data from a straight line at strain near zero is due to the zero point uncertainty of the measuring set-up [Zhang et al., 1998].

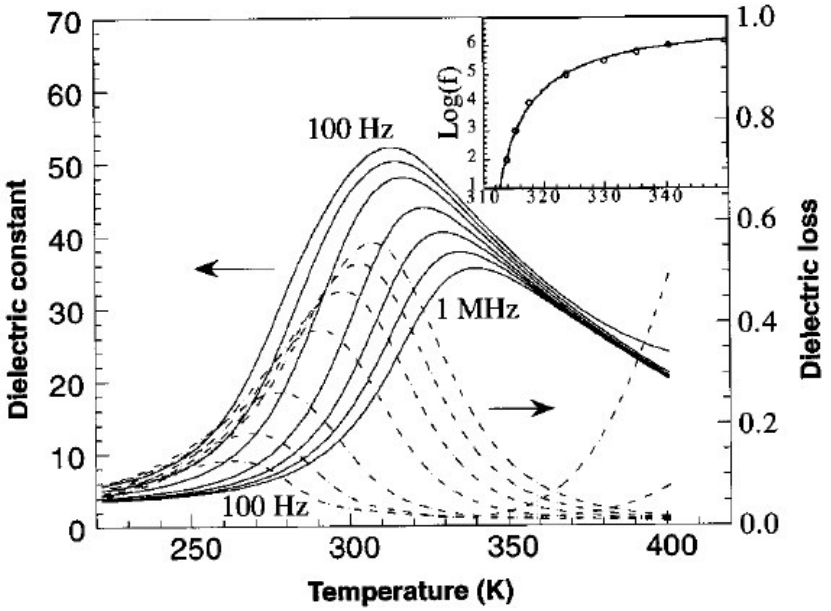


Figure 1.10 The dielectric constant (solid lines) and dielectric loss (dashed lines) as a function of temperature for P(VDF-TrFE) 50/50 copolymer after irradiation with $4 \times 10^5$ Gy at 120 $^{o}$C. The frequency is (from top to bottom curves for dielectric constant and from bottom to top curves for dielectric loss): 100 Hz, 1 kHz, 10 kHz, 100 kHz, 300 kHz, 600 kHz and 1 MHz. The inset shows the fitting of the Vogel-Fulcher law, where the solid line is the fit and the circles are the data [the horizontal axis in the inset is temperature (in Kelvin), and $f$ is the frequency] [Zhang et al., 1998].

The widely available 70/30 mol% P(VDF-TrFE) is quite difficult to soften under irradiation [Cheng, 2000]. Irradiation is typically accomplished in a nitrogen atmosphere at elevated temperatures with irradiation doses up to 120 Mrad. Cheng et al. found that it was difficult to change the properties of P(VDF-TrFE) copolymers with

VDF content higher than 70 mol%. Lau et al. [2002, 2003, 2004] have shown that protons are more effective than electrons and γ-rays since irradiation with protons in the MeV range at room temperature can readily convert a copolymer with 70 mol% or higher VDF content into a ferroelectric relaxor. Some results on the structural changes in 56/44 mol% P(VDF-TrFE) upon proton irradiation at doses from 43 to 200 Mrad have been reported. It was observed that even at a low dose of 43 Mrad, the 56/44 mol% copolymer was almost completely converted to a relaxor. This shortened the expensive and time-consuming irradiation step in preparing the polymer.

It has been shown that the field-induced piezoelectricity in the relaxor ferroelectric P(VDF-TrFE) copolymer is enhanced in comparison to the normal ferroelectric copolymer and the effective piezoelectric coefficients can be tuned by the applied dc biasing field as shown in Figure 1.11. Such tunable piezoelectricity may provide useful technological applications in smart structures.

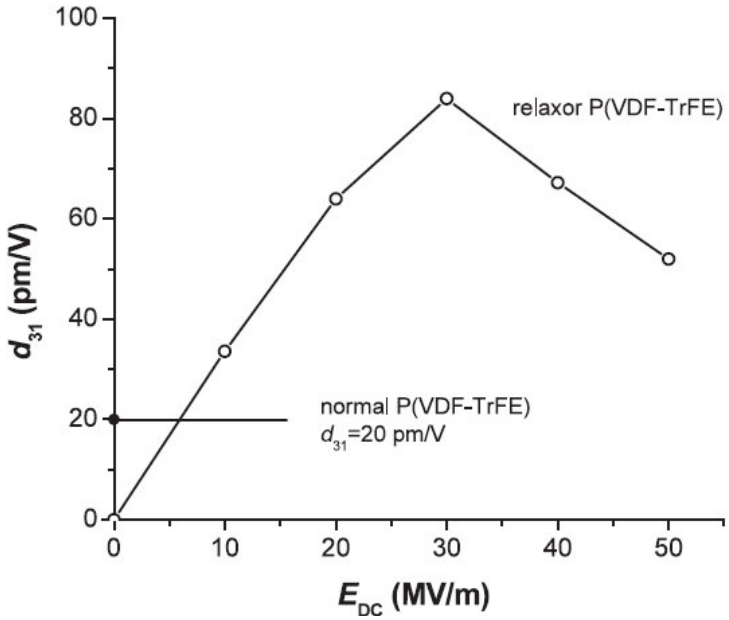


Figure 1.11 Effective piezoelectric coefficient $d_{31}$ versus $E_{DC}$ in the electron-irradiated P(VDF-TrFE) copolymer. The typical $d_{31}$ value (20 pm/V) for the normal 50/50 mol% P(VDF-TrFE) is shown for comparison [Ma et al., 2005].

## 1.4 Scope of Thesis

The objectives of this work are to study the potential for modifying the properties of 56/44 mol% P(VDF-TrFE) with low proton doses of 10-50 Mrad, and to use a Si membrane structure to fabricate a micromachined acoustic transducer.

Following the introduction in this chapter, there are five chapters including:

- Characterization of Proton Irradiated 56/44 mol% P(VDF-TrFE) Copolymer
- Fabrication of P(VDF-TrFE) MEMS
- Performance of P(VDF-TrFE) MEMS
- Study of Clamping Effect on the Electrostrictive Coefficient of 56/44 mol% P(VDF-TrFE)
- Conclusions

In Chapter 2, the fabrication process of 56/44 mol% P(VDF-TrFE) thick film is first introduced. The structural and ferroelectric properties of proton-irradiated copolymers are then described. X-ray diffraction (XRD) technique is used to confirm the crystalline phase of the copolymer. The phase transition behaviour is studied by differential scanning calorimetry (DSC). The ferroelectric and dielectric properties of copolymer are measured and discussed. Also, the investigation of electrostrictive strain response in proton-irradiated copolymer is reported.

The fabrication process of polymer micro-electromechanical systems (MEMS) is presented in Chapter 3. Bulk micromachining has been used to fabricate the deformable membrane, which oscillates in response to acoustic signals.

Performance of 70/30 mol% P(VDF-TrFE) copolymer MEMS at 40 kHz is described in Chapter 4. A Mach-Zehnder type heterodyne laser interferometer has been used to measure the displacement of the membrane. Acoustic responses of both the transmitting and receiving sensitivity of the copolymer MEMS has been studied.

In Chapter 5, the clamping effect of proton irradiated 56/44 mol% P(VDF-TrFE) copolymer thin film spin-coated on silicon membrane are studied by comparing their effective electrostrictive coefficient $M_{33}$ and the $M_{33}$ of free bulk P(VDF-TrFE) thick films.

Conclusions and suggestions for future work are given in Chapter 6.

# Chapter 2

# Characterization of Proton Irradiated 56/44% P(VDF-TrFE) Copolymer

## 2.1 Introduction

As mentioned in Chapter 1, there are some preliminary results reported on the structural changes in 56/44 mol% poly(vinylidene fluoride-trifluoroethylene) P(VDF-TrFE) upon proton irradiation at doses ranged from 43 to 200 Mrad [Lau et al., 2004]. It was reported that at a proton dose of ~ 75 Mrad, 56/44 mol% copolymer has completely converted to a relaxor. However, it was observed that even at a low dose of 43 Mrad, the 56/44 mol% copolymer was almost completely converted to a relaxor. Hence, it is of interest to find out what is the minimum proton dose that could induce this conversion.

In this Chapter, 56/44 mol% P(VDF-TrFE) thick films were fabricated and undergone proton irradiation treatment. The present work studied the variation of properties in the copolymer irradiated with proton doses of 10-50 Mrad. Changes of the polarization hysteresis loop, relative permittivity, XRD spectra, DSC thermograms and electrostrictive coefficient with proton dosage were studied.

## 2.2 Fabrication of P(VDF-TrFE) Copolymer Films

### 2.2.1 Film Fabrication

P(VDF-TrFE) copolymer pellets with 56 mol% of VDF, supplied by Piezotech Co., Saint Louis, France, were used in the present study. Films of thickness of ~ 30 μm and diameter of ~ 25 mm were fabricated by hot compression moulding. The copolymer pellets were placed in a circular steel mould (Constant Thickness Film Maker, SPECAC P/N 15620), on which two pieces of polyimide films were placed between the copolymer pellets and the steel mould. The use of polyimide film was to prevent the copolymer film from sticking on the mould after the hot pressing process and also to produce a smoother surface. The mould was then placed on a hot-press machine (CARVER 2699-127) set at a temperature of 210 °C. After 10 min of preheating, a pressure of ~50 MPa was applied for 15 min. The mould was then taken out and cooled naturally to room temperature in air. The films were then annealed at 120 °C for 2 h to achieve higher crystallinity and then slowly cooled to room temperature.

### 2.2.2 Proton Irradiation Process on P(VDF-TrFE) Copolymer Films

In order to quantify the irradiation energy deposited on a material, the dose is measured by a unit called Gray (Gy). In terms of energy relationship, one Gray equals to one joule of energy deposited per kilogram of material being irradiated, which can be expressed in terms of eV:

$$1\ \text{Gy} = 6.24 \times 10^{18}\ \text{eV/kg} \qquad (2.\ 1)$$

However, in most of the studies involving irradiation process on P(VDF-TrFE) copolymer, the unit of rad was used to describe the dose:

$$1\ \text{Gy} = 100\ \text{rad} \qquad (2.\ 2)$$

In this study, the proton irradiation treatment was carried out in an accelerator (High Voltage Engineering Europa B.V., Netherlands) at ambient temperature with a 3 MeV proton ($H^+$ ion) beam at the Department of Electronic Engineering, The Chinese University of Hong Kong. The linear energy transfer (LET) for 3 MeV proton irradiation of P(VDF-TrFE) copolymer, which is generally used to describe the energy deposition by a charge particle per unit length of trajectory, is ~ 20 eV/nm. According to the effect of energy on the penetration depth for different ions, which is examined

using a Monte Carlo simulation code 'Transport of Ions in Matter' (TRIM) [Ziegler et al., 1985], the penetration depth for a 3 MeV $H^+$ proton ion is 92.1 μm. Thus, all thick copolymer films were fabricated with thickness of ~30 μm to ensure that the protons could pass through instead of implanting in the copolymer film.

The proton fluence applied to the sample was in the range of 0.59 to 6.35 × $10^{17}$ ions/$m^2$. The irradiation dose (rad) was the product of the fluence (ions/$m^2$) and the LET (eV/nm) divided by the density (~ 1900 kg/$m^3$) of the copolymer, and using the conversion factors shown in Eqs. (2.1) and (2.2). The proton dose was calculated to be in the range of 10 to 50 Mrad.

During irradiation, the beam current was set at a low level of ~ 3.8 nA to prevent excessive temperature increase in the films. After irradiation treatment, aluminum electrodes with thickness of ~ 0.1 μm were sputtered on the surfaces of both the unirradiated and irradiated samples for subsequent electrical measurements.

## 2.3 Structure Characterization of Proton-irradiated P(VDF-TrFE) Copolymer

### 2.3.1 XRD Characterization

X-ray diffractometry (XRD) is a common method to reveal information about the physical structure of various materials, such as crystalline phases in materials, the extent of crystallinity and crystallite structures. In this study, the X-ray diffraction pattern of the copolymer was obtained at room temperature using an X-ray diffractometer (X'pert System, Philips Electronic Instruments) equipped with nickel-filtered CuKα radiation. The scanning speed was 0.005 $^{o}$/s

Figure 2.1 shows the X-ray diffraction patterns for the copolymers irradiated with various proton doses at room temperature. For the unirradiated film, two closely-spaced peaks associated with the (200) and (110) reflections are observed, which suggests a distortion from the hexagonal type lattice [Tashiro et al., 1983; Davis et al., 1982]. Upon irradiation, the two peaks are shifted to lower angles, indicating the expansion of the crystal lattice presumably due to the presence of double-bonds and crosslinkings caused by the irradiation. [Welter et al., 2003; Daudin et al., 1991] These defects lead to a decrease in the dipole concentration of VDF and TrFE monomers, thereby giving rise to a reduced ferroelectric ordering. With further increase in the irradiation dose, the two peak merges into a single peak at $2\theta = 18.2^{o}$, corresponding to a lattice spacing of 4.87 Å which is close to that of the high-temperature phase

(paraelectric phase) of the unirradiated copolymer [Tashiro et al., 1983]. This XRD result indicates that the normal ferroelectric (polar) phase has been transformed to a paraelectric-like (non-polar) phase by the proton irradiation.

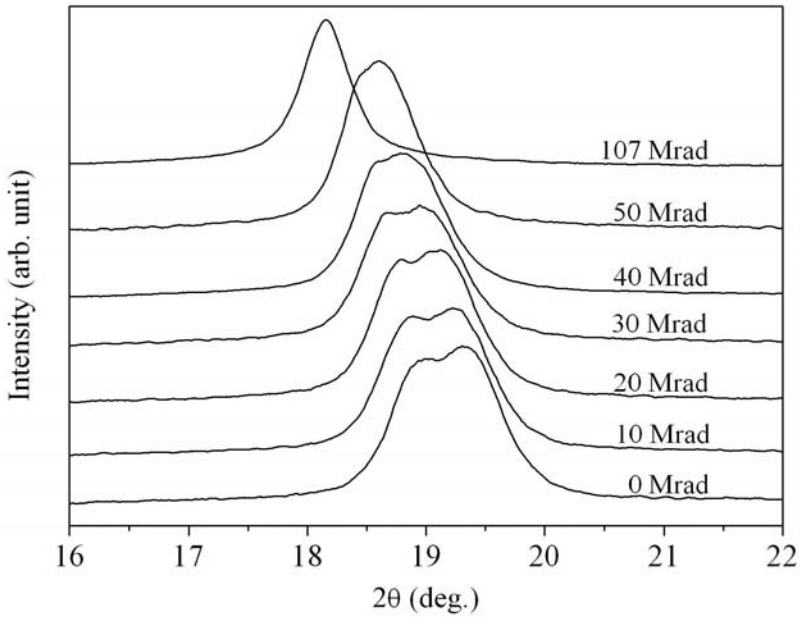


Figure 2.1 X-ray diffraction patterns of 56/44 mol% P(VDF-TrFE) copolymer films irradiated with different proton doses measured at room temperature. Data of the 107 Mrad irradiated copolymer were taken from Lau et al. [2004].

### 2.3.2 DSC Thermal Analysis

Differential scanning calorimetry (DSC) is a technique widely used to study the transitions in the sample material such as melting, glass transitions, solid-state transitions or crystallization. DSC based on measuring the energy involved between a sample and a reference material, so as to keep identical temperature in an environment while heated or cooled at a controlled rate. The continuous adjustment of the heater power provides a varying electrical signal equivalent to the varying thermal behaviour of the sample. In this study, the thermal measurement was performed using a differential scanning calorimeter (Perkin Elmer DSC 7) at a scanning rate of 10 °C/min from 0 $^{o}$C to 200 $^{o}$C under a nitrogen atmosphere. About 10 mg of sample was encapsulated in an aluminum pan and an empty aluminum pan served as the reference.

The DSC data in Figure 2.2 shows an obvious change in the phase transition behaviour as the proton dose increases. For the unirradiated film, two well-defined peaks are observed, one at 156.3 $^{o}$C and the other at 64.3 $^{o}$C, corresponding to the melting and ferroelectric-paraelectric (F-P) phase transition in the crystalline regions, respectively [Tanska et al., 1987]. The peak associated with the F-P transition becomes very broad and diffuse and almost disappears when the dose is increased to 40 Mrad, but the change in the melting peak is not significant. This indicates that the polar ordering is more seriously affected than the crystal ordering upon the irradiation treatment. When the dose is further increased to 107 Mrad (data taken from Lau et al. [2004]), the

melting peak broadens and shifts to a lower temperature, indicating a broad distribution of crystallite sizes. The melting enthalpy decreases substantially, indicating a significant decrease in crystallinity.

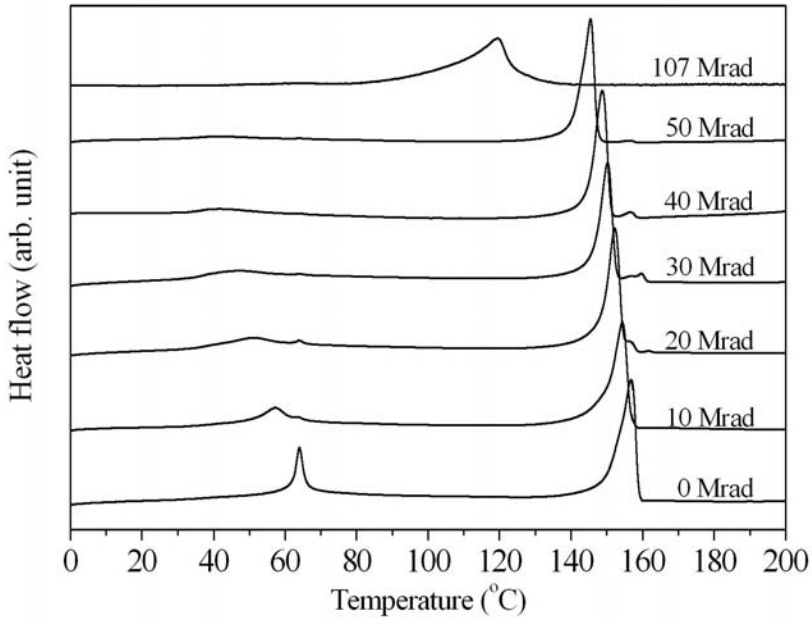


Figure 2.2 DSC thermogram of copolymer films irradiated with different proton doses. Data of the 107 Mrad irradiated copolymer were taken from Lau et al. [2004].

## 2.4 Properties of Proton-irradiated 56/44 mol% P(VDF-TrFE) Copolymer

### 2.4.1 Polarization-Electric Field (P-E) Hysteresis

The behaviour of polarization reversal can be described by a hysteresis loop, and the P-E loop can be measured using a Sawyer-Tower circuit [Sawyer et al., 1930] . In this study, the hysteresis loops were obtained by a computer-controlled system based on a modified Sawyer-Tower circuit as shown in Figure 2.3. A sinusoidal electric voltage $V$ at a frequency of 10 Hz, supplied by a function generator (HP 8116A) and then amplified 100 times by a power amplifier (KEPCO BOP1000) was applied to the sample at room temperature. The voltage $V$ across the sample was connected to the horizontal plate of an oscilloscope, from which the electric field $E$ applied to the sample was calculated. The polarization charge $Q$ generated on the sample was transferred to a reference capacitor $C_{ref}$ connected in series with the sample. Thus, by measuring the voltage across the reference capacitor $V_{ref}$, which is connected to the vertical plate of the oscilloscope, the electric displacement $D$ of the sample could be calculated by:

$$Q = V_{ref} C_{ref} \tag{2. 3}$$

$$D = \frac{Q}{A} = \frac{V_{ref} C_{ref}}{A} \tag{2. 4}$$

where $A$ is the area of the electrode. In order to ensure the full application of $V$ across the sample, a 1 μF reference capacitor which is much larger than the capacitance of the sample, was used in the measurement.

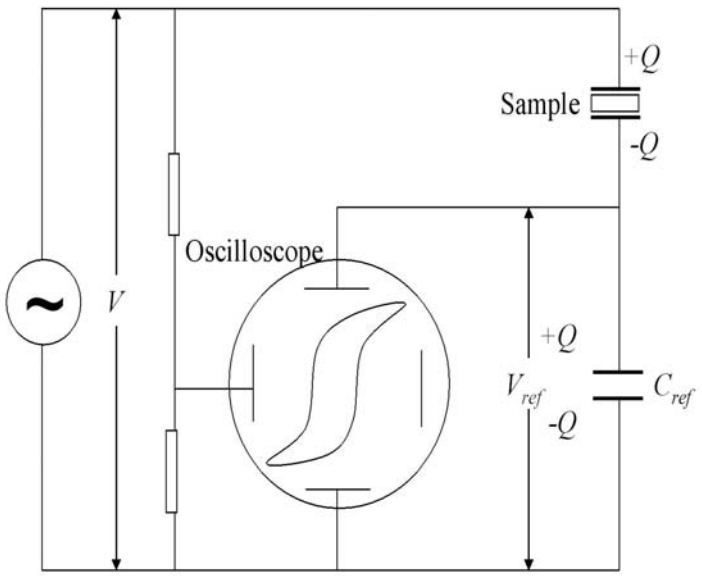


Figure 2.3 Schematic diagram of a modified Sawyer-Tower circuit.

The polarization hysteresis loops for the copolymer films irradiated with different proton doses measured at room temperature and 10 Hz are presented in Figure 2.4. All the hysteresis loops were obtained under an a.c. electric field of ±100 MV/m. The unirradiated sample exhibits a well-defined square hysteresis loop with a maximum induced polarization $P_s$ of 6.0 μC/cm$^2$, remanent polarization $P_r$ of 5.0 μC/cm$^2$ and coercive field $E_c$ of 59 MV/m. Such a large hysteresis loop observed in a normal ferroelectric copolymer is caused by the high nucleation barrier for the polarization switching in coherent macroscopic domains. P(VDF-TrFE) is a semicrystalline

polymer which consists of about 70 % of crystalline region embedded in an amorphous matrix. Ferroelectric domains exist only in the crystalline regions and the polarization response reflects the cooperative switching of the dipoles in the domains. Although the crystalline and amorphous regions are linked by some chains, the amorphous regions probably contribute very little to the polarization response. After irradiation, even at a low proton dose of 10 Mrad, the hysteresis loop becomes slimmer and the polarization level as well as the coercive field drops significantly. At higher proton doses (e.g. 30 Mrad), not all the microscopic ferroelectric domains have been converted into nano-regions. Therefore, the observed hysteresis loop is the combined behaviour of the ferroelectric domains (square loop) and nano-regions (almost a line), and so superficially looks like the loop of an antiferroelectric material. As the proton dose increases to 50 Mrad, $P_s$ decreases slightly to 4.5 μC/cm$^2$, while $P_r$ and $E_c$ drop nearly to zero (Figure 2.5). At 107 Mrad (data taken from Lau et al. [2004]), the hysteresis loop becomes very slim, which indicates that the normal ferroelectric phase has disappeared because the proton irradiation has broken up the macroscopic domains into nano-polar regions. [Cheng et al., 2000]

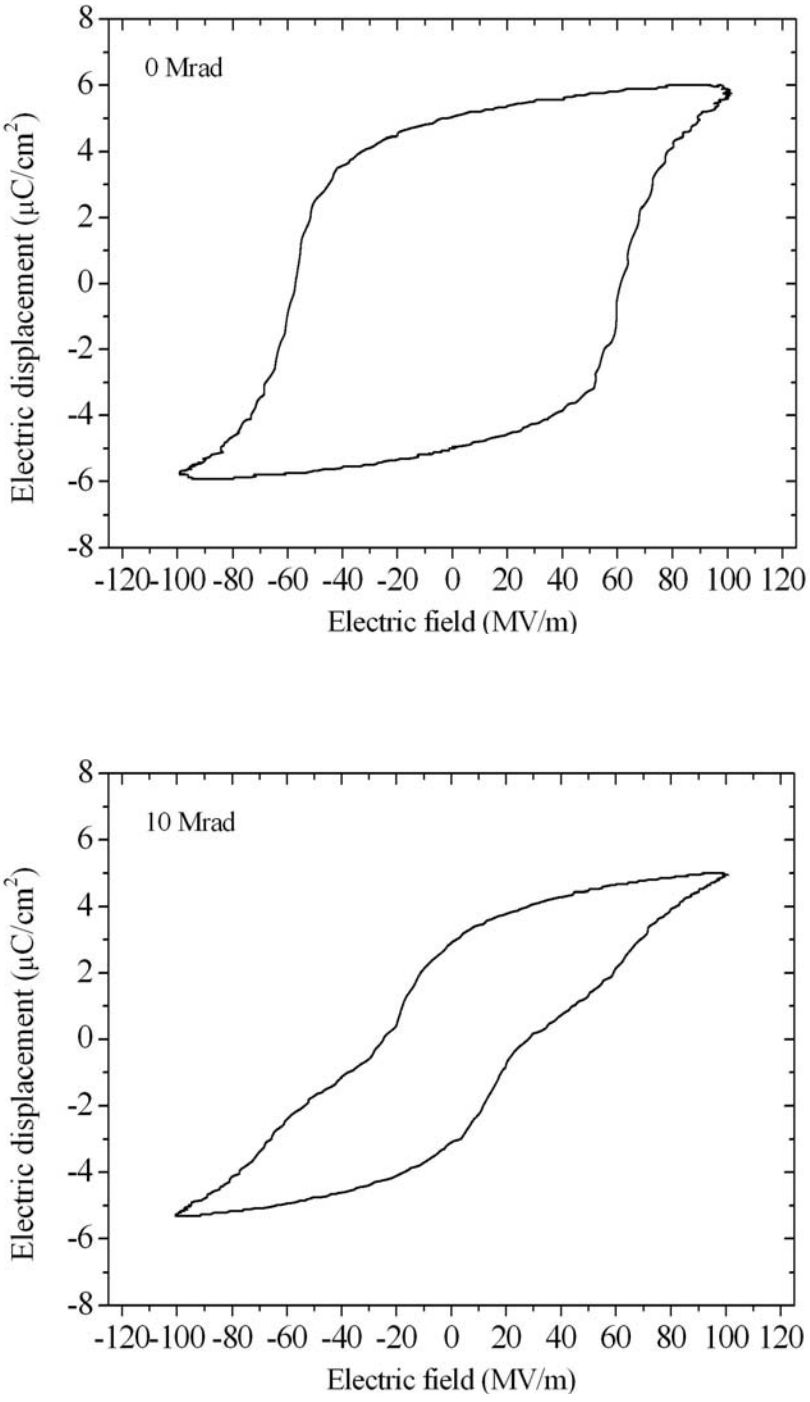


Figure 2.4 Polarization hysteresis loops measured at room temperature and 10 Hz for 56/44 mol% P(VDF-TrFE) copolymer films irradiated with different proton doses. Data of the 107 Mrad irradiated copolymer were taken from Lau et al. [2004].

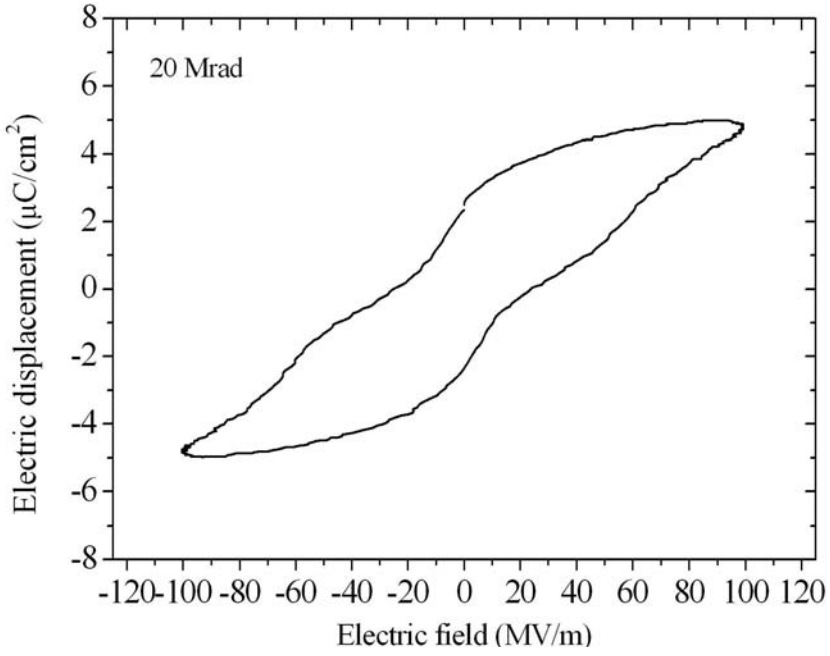


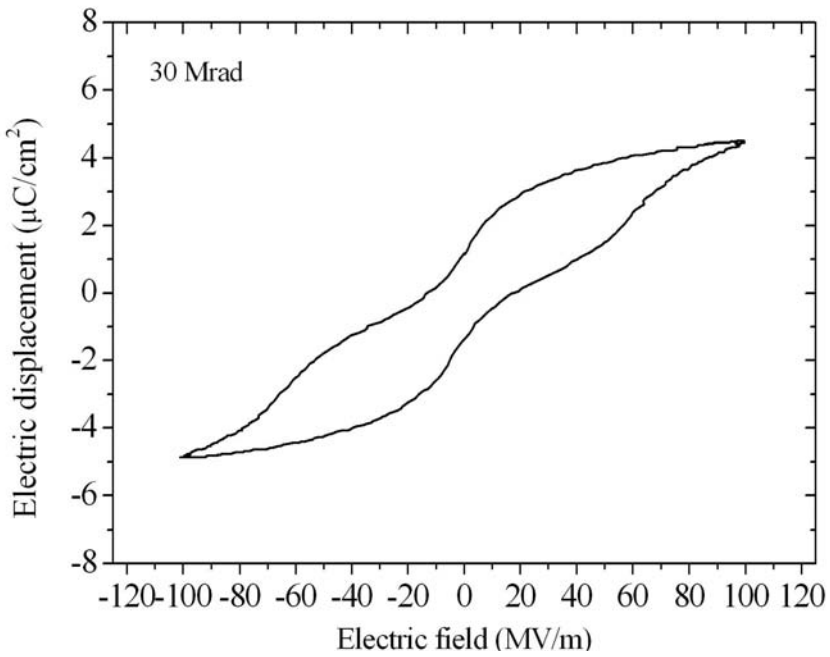


Figure 2.4 (Continued).

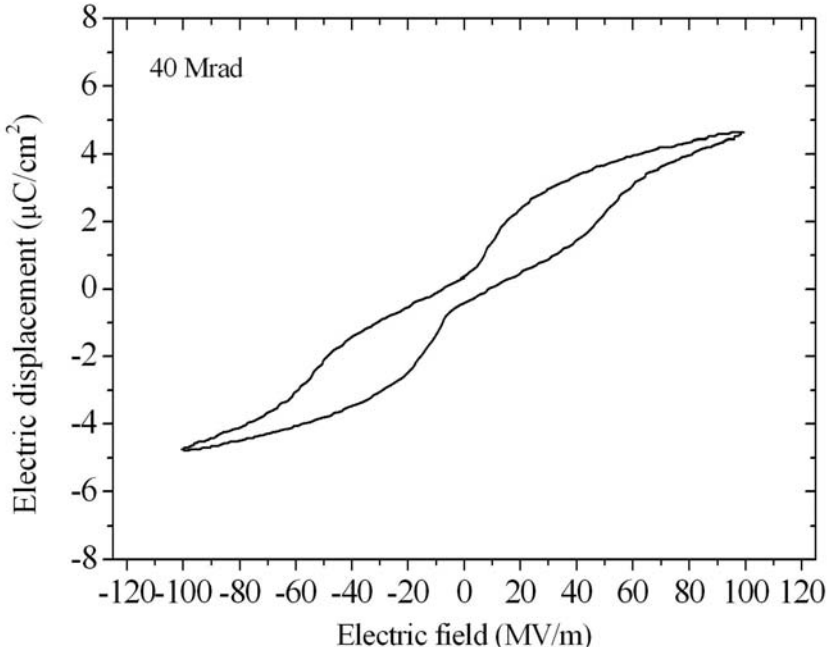


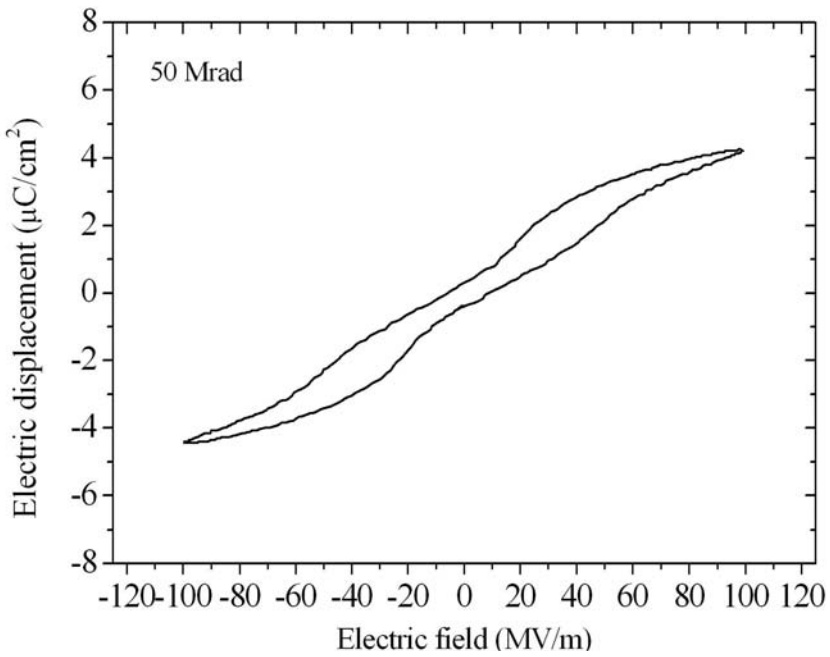


Figure 2.4 (Continued).

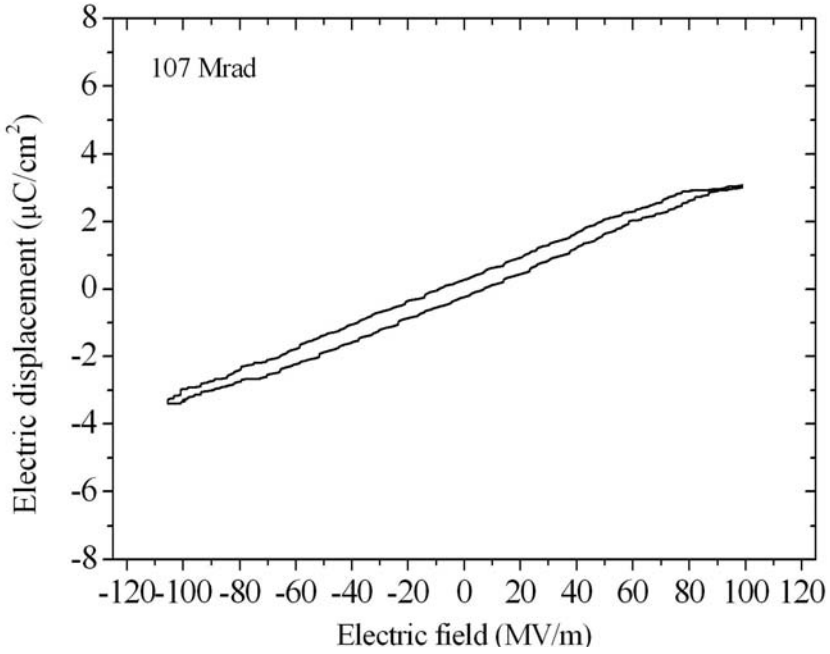


Figure 2.4 (Continued).

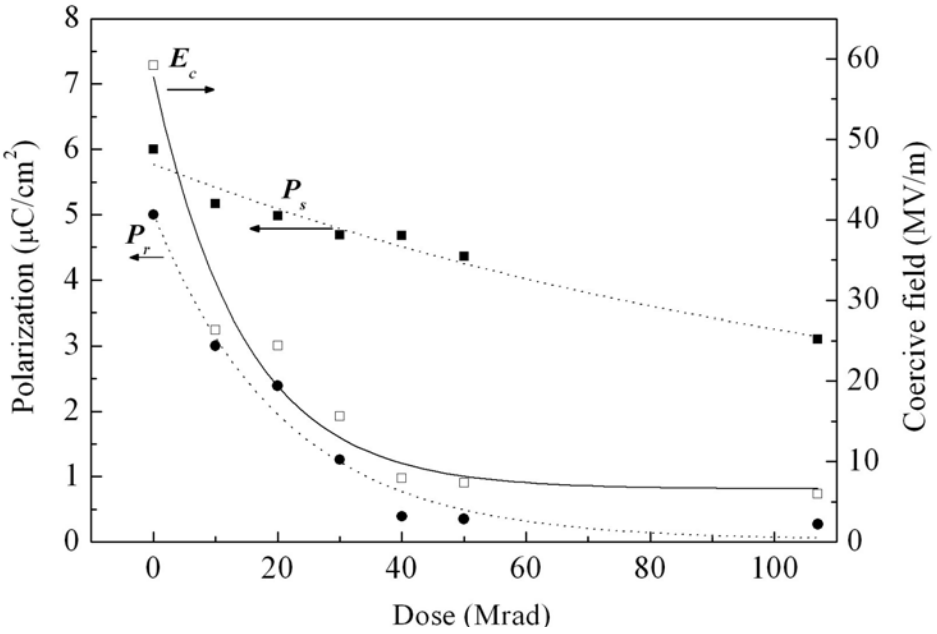


Figure 2.5 Variation of the maximum induced polarization $P_s$, remanent polarization $P_r$, and coercive field $E_c$ of the copolymer films with the proton dose. Data of the 107 Mrad irradiated copolymer were taken from Lau et al. [2004].

### 2.4.2 Relative Permittivity and Dielectric Loss

The relative permittivity and dielectric loss are important practical parameters for most applications of ferroelectric materials and studies of the dielectric properties provide information on the structure and phase transition of ferroelectric materials.

The permittivity $\varepsilon$ describes the ability of a material to resist the flow of electrical charge. It is defined as the ratio of the electric displacement in the medium to the electric field strength:

$$\varepsilon = \frac{D}{E} \tag{2. 5}$$

In defining the permittivity of a medium, a dimensionless relative permittivity $\varepsilon_r$, normalized to the absolute vacuum permittivity $\varepsilon_o = 8.854 \times 10^{-12}$ F/m is used ($\varepsilon_r = \frac{\varepsilon}{\varepsilon_o}$). For a parallel plate capacitor containing a dielectric medium, the relative permittivity $\varepsilon_r$ is given by:

$$\varepsilon_r = \frac{Cd}{A\varepsilon_o} \tag{2. 6}$$

where $C$ is the capacitance of the sample, $d$ the thickness of the sample and $A$ is the area of the electrode. In general, realistic materials are lossy to some extent and the relative permittivity is usually defined in a complex form:

$$\varepsilon_r = \varepsilon_r^{'} - i\varepsilon_r^{''} \tag{2. 7}$$

The loss factor tanδ used to express dielectric loss is given by:

$$\tan\delta = \frac{\varepsilon_r^{''}}{\varepsilon_r^{'}} \tag{2. 8}$$

In this study, the capacitance and the dielectric loss were determined by an HP4194A impedance/gain-phase analyzer equipped with a temperature chamber (ESPEC SU-240). The sample was first cooled to -20 $^{o}$C and the permittivity was measured up to 120 $^{o}$C and then down to -20 $^{o}$C at a rate of ~ 1 $^{o}$C/min as a function of temperature at frequencies varying from 1 kHz to 5 MHz.

The temperature dependence of the relative permittivity $\varepsilon_r$ and dielectric loss measured at 1 kHz for the unirradiated and irradiated copolymer films in the first heating run is shown in Figure 2.6. The unirradiated sample exhibits a ferroelectric-paraelectric transition peak at $T_m$ ~ 70 °C with a maximum value of the relative permittivity $\varepsilon_{r(max)}$ of 64. After irradiation, the peak broadens and shifts to a lower temperature. The value of $\varepsilon_{r(max)}$ also decreases with increasing proton dose. Moreover, the irradiated copolymer shows a feature common to all relaxor ferroelectrics, namely that the peak amplitude decreases and the peak temperature $T_m$ shifts progressively towards higher temperature with increasing frequency $f$ (Figure 2.7). Proton irradiation leads to the formation of double bonds and crosslinkings and breaks up the ferroelectric domains into nano-polar regions, thereby converting the normal ferroelectric copolymer into a relaxor ferroelectric material.

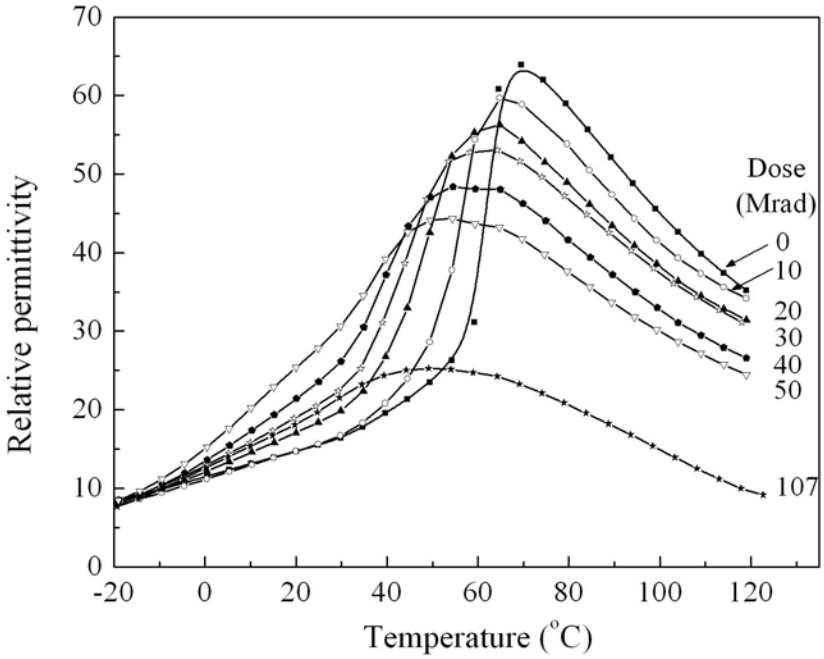


Figure 2.6 Relative permittivity $\varepsilon_r$ measured at 1 kHz as a function of temperature for the 56/44 mol% P(VDF-TrFE) copolymer films irradiated with different proton doses in the first heating run. Data of the 107 Mrad irradiated copolymer were taken from Lau et al. [2004].

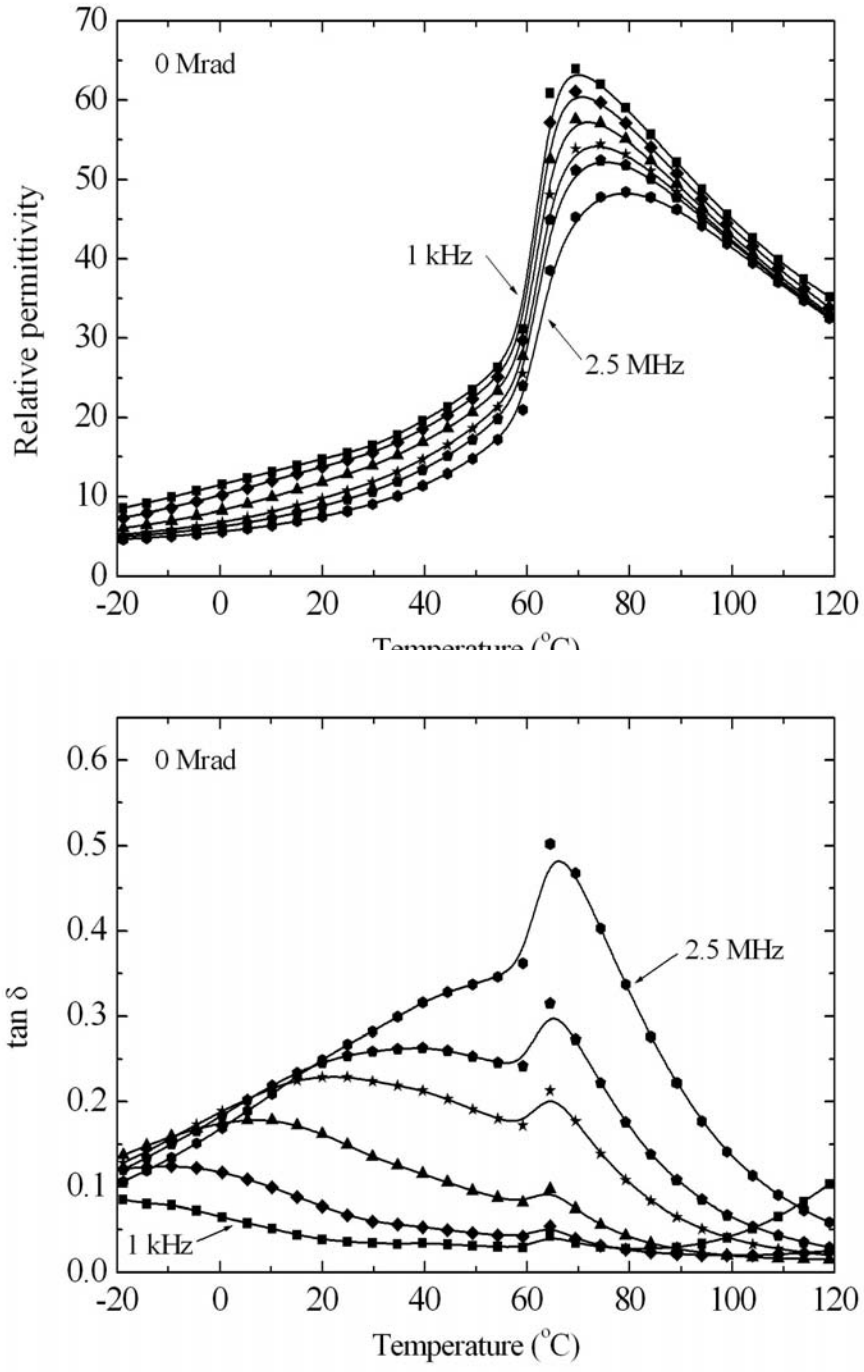


Figure 2.7 Relative permittivity $\varepsilon_r$ as a function of temperature for the irradiated copolymer films in the first heating run. The measuring frequencies are: 1 kHz, 10 kHz, 100 kHz, 500 kHz, 1 MHz and 2.5 MHz.

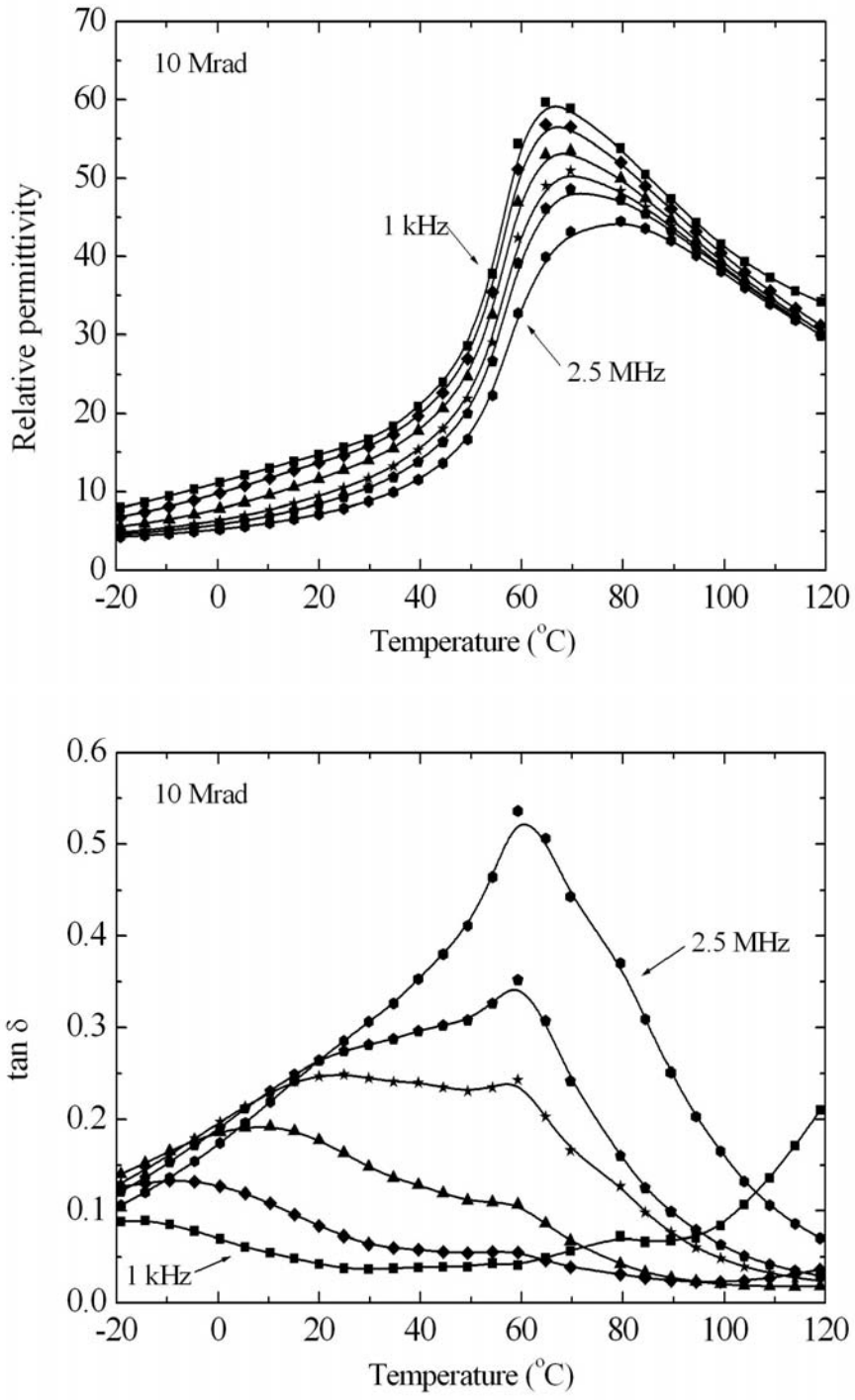


Figure 2.7 (Continued).

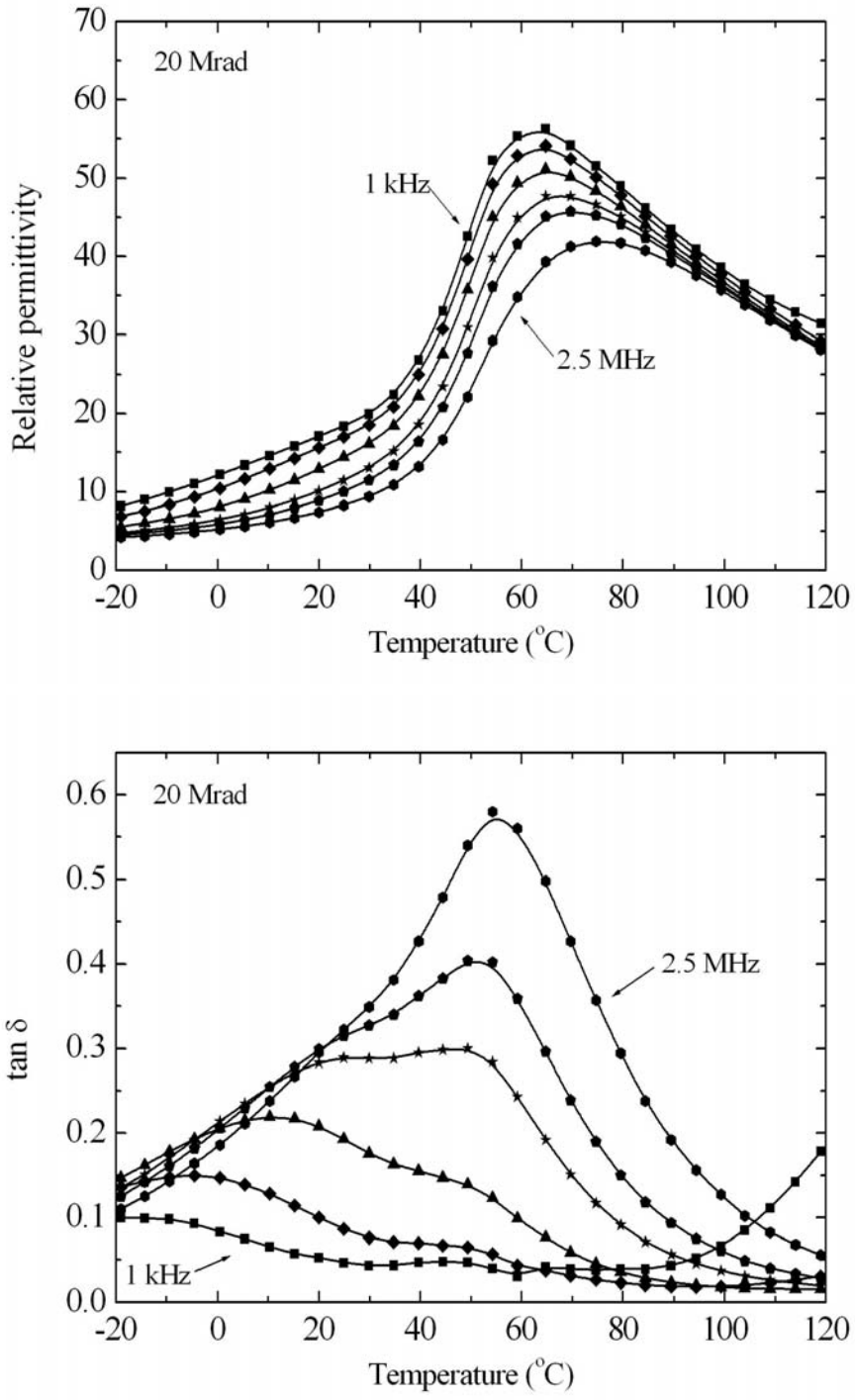


Figure 2.7 (Continued).

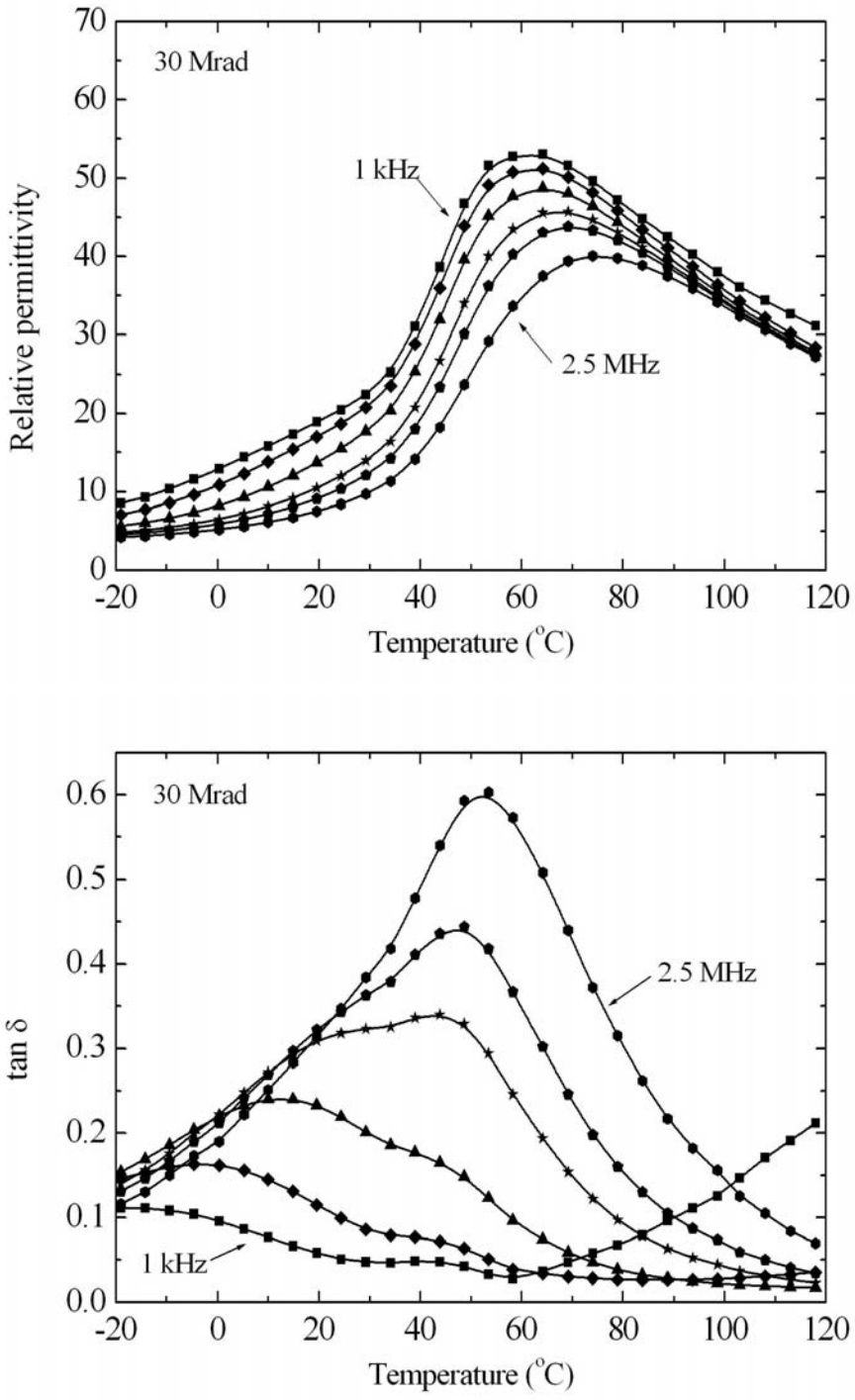


Figure 2.7 (Continued).

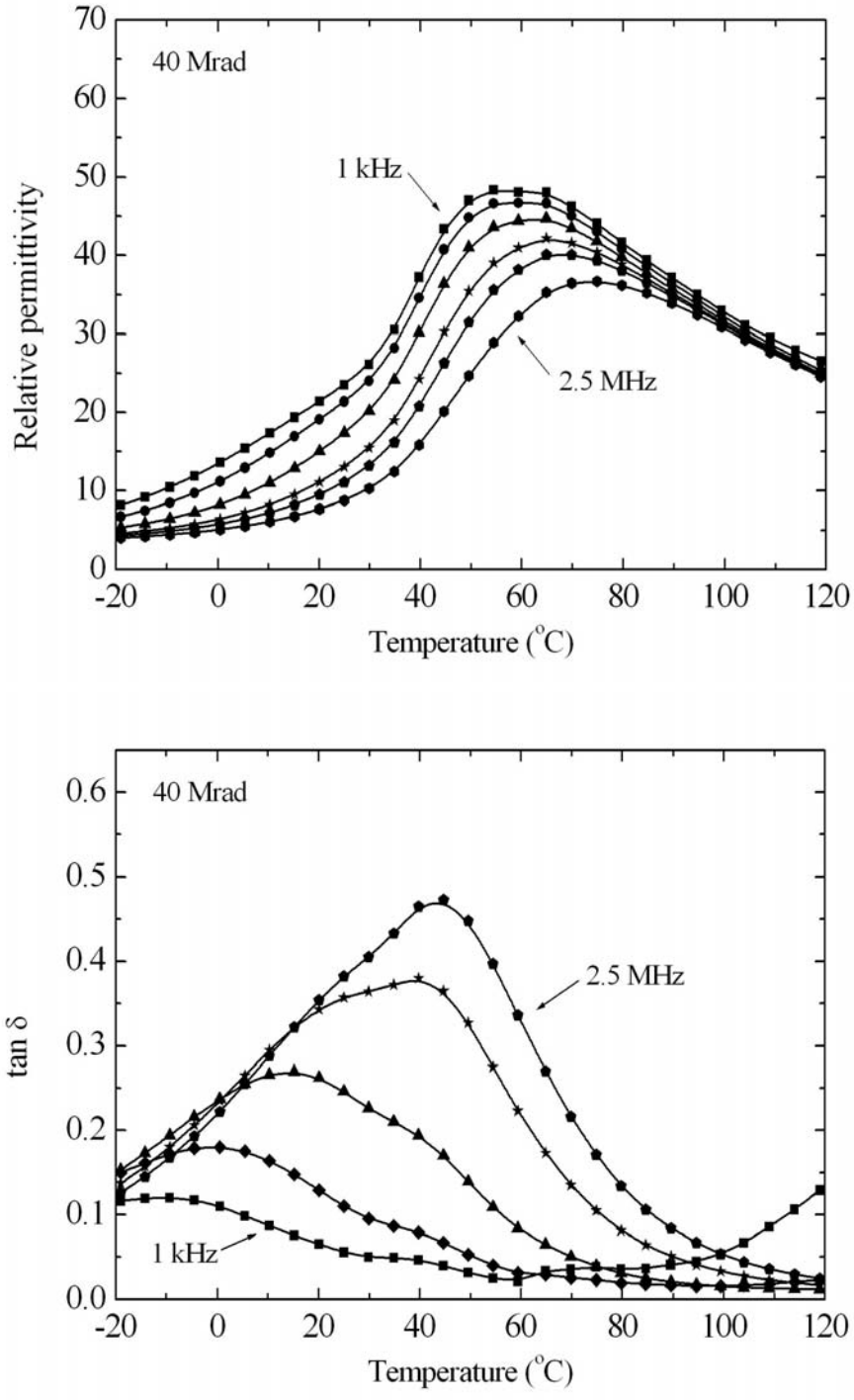


Figure 2.7 (Continued).

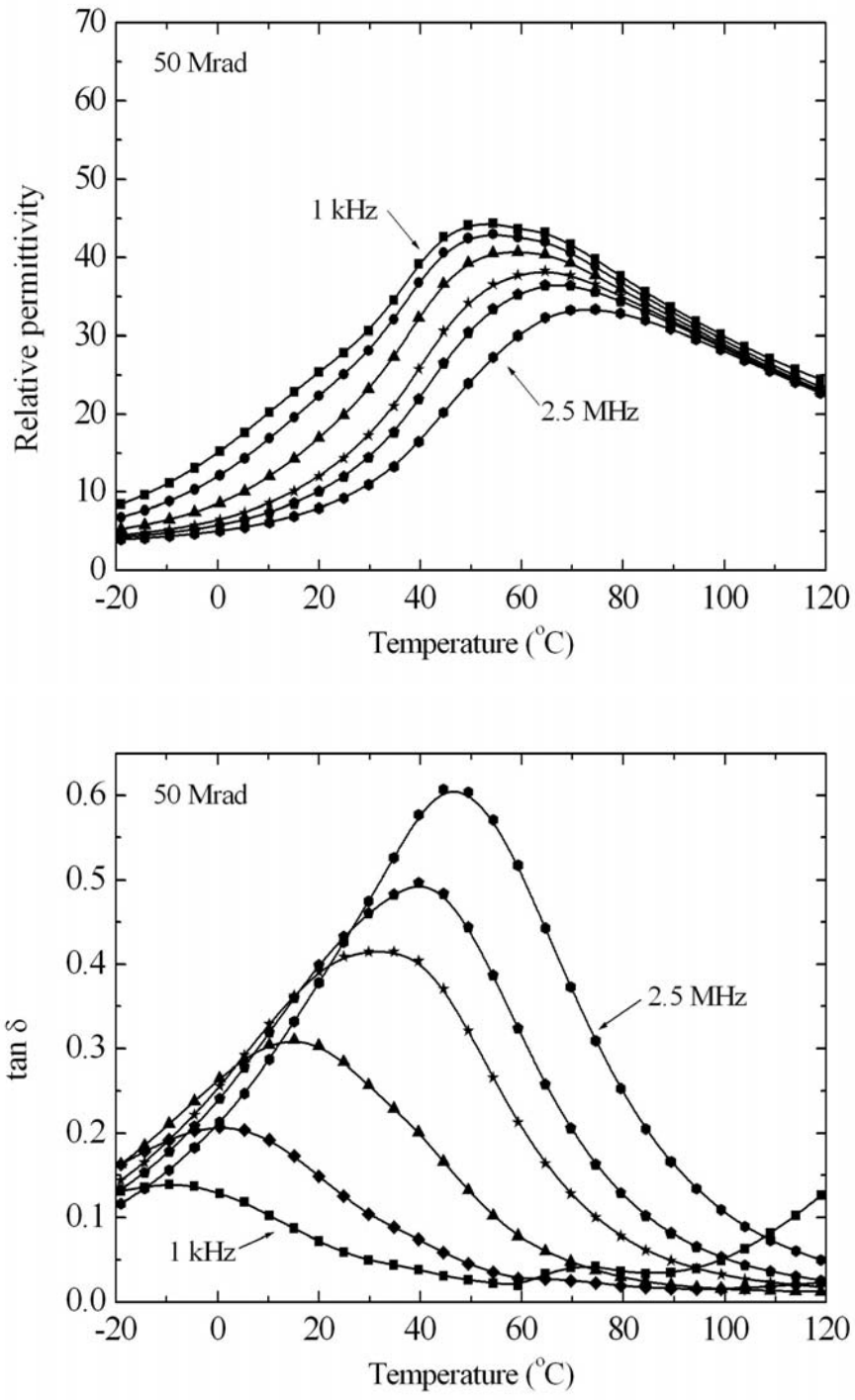


Figure 2.7 (Continued).

As shown in Figure 2.8, the relationship between $T_m$ and $f$ can be described by the Vogel-Fulcher (V-F) law that holds for relaxor ferroelectrics:

$$f = f_o \exp\left(\frac{-U}{k(T_m - T_f)}\right) \quad (2.9)$$

where $U$ is the activation energy, $k$ the Boltzmann's constant, $T_f$ the freezing temperature and $f_o$ is the Debye frequency. [Cross et al., 1994; Viehland et al., 1990] The parameters obtained by fitting the V-F law to the data for the copolymer films irradiated with different doses are summarized in Table 2.1. The increasing value of $U$ and $f_o$ indicates that the dielectric behaviour depends more strongly on frequency as the dose increases. [Cheng et al., 2002]

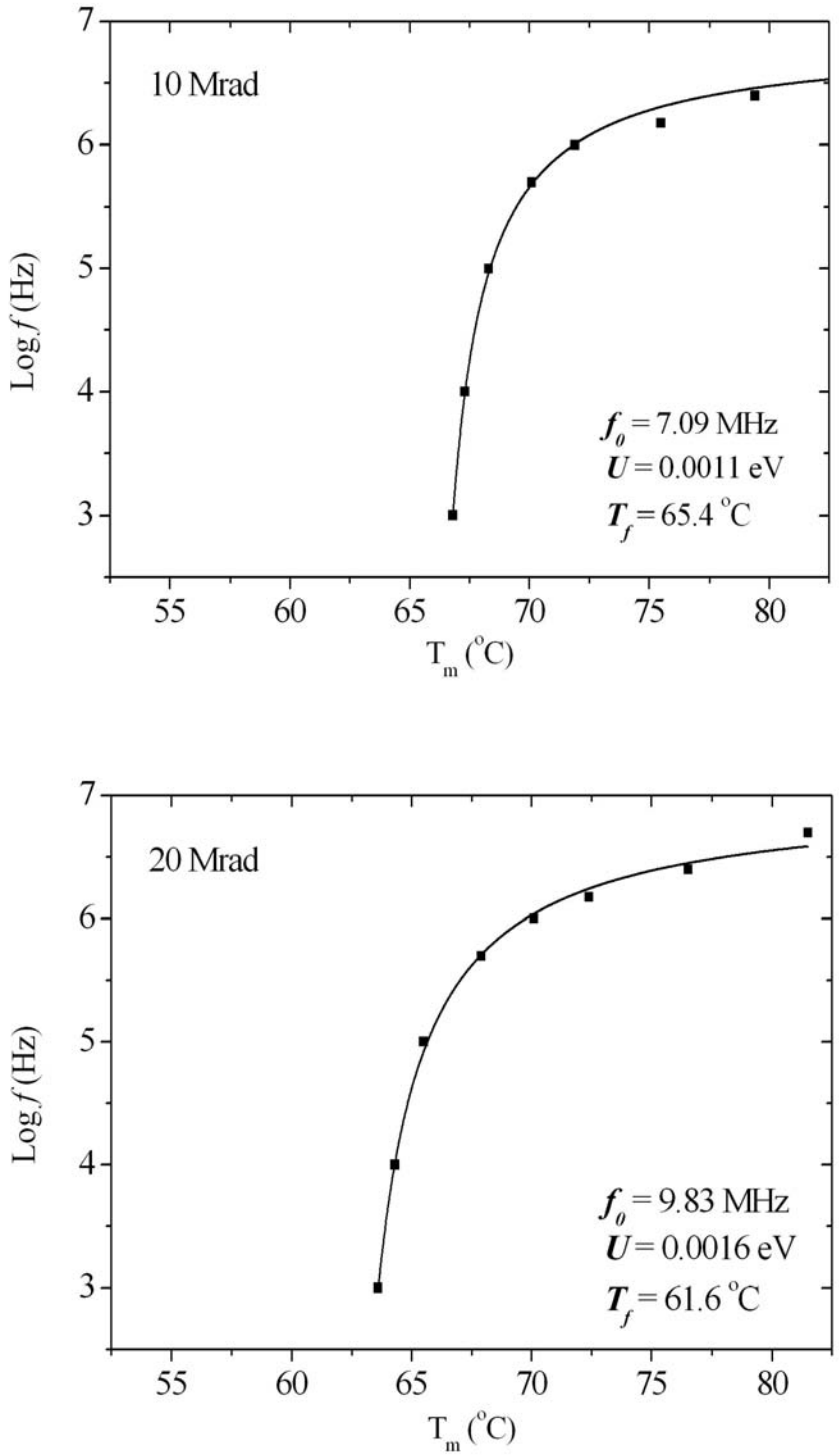


Figure 2.8 Fitting of the Vogel-Fulcher law to the relative permittivity data for irradiated copolymer film. The symbols are the experimental data and the solid line is the fitted curve.

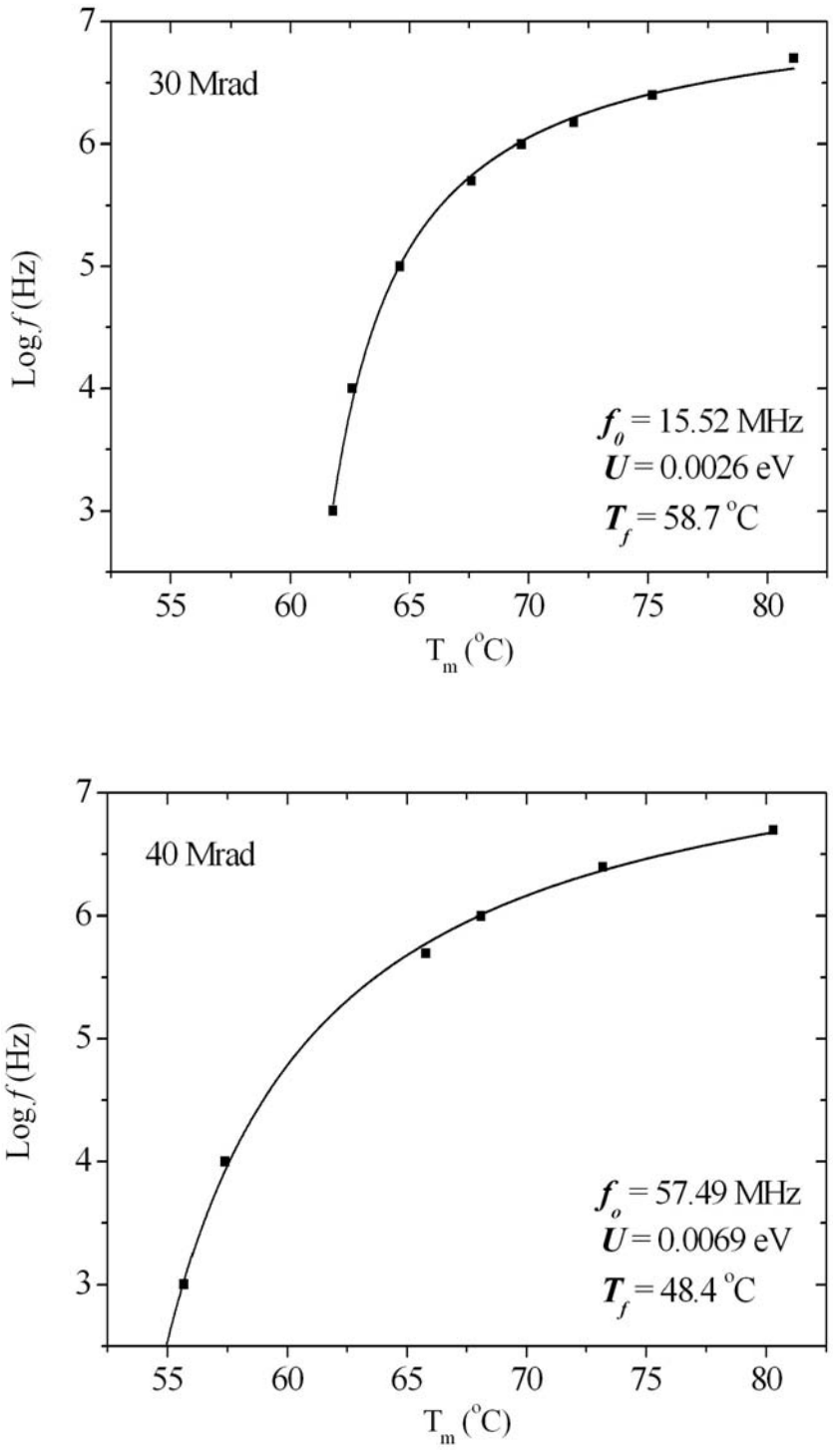


Figure 2.8 (Continued).

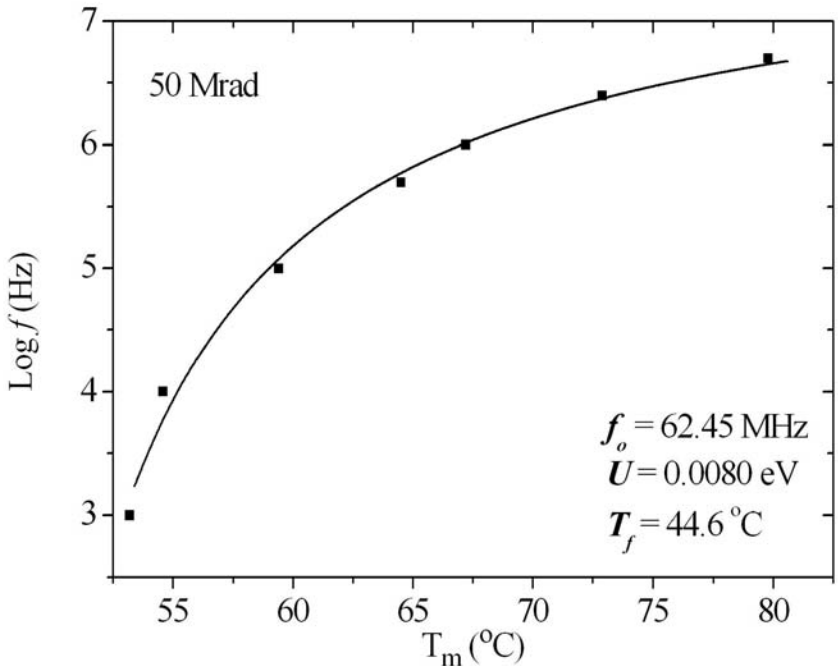


Figure 2.8 (Continued).

Table 2.1 Fitting parameters in the Vogel-Fulcher law for proton irradiated 56/44 mol% P(VDF-TrFE) copolymer films.

| **Dosage (Mrad)** | $f_o$ **(MHz)** | $T_f$ **(°C)** | $U$ **($10^{-3}$ eV)** |
|---|---|---|---|
| 10 | 7.1 | 65.4 | 1.1 |
| 20 | 9.8 | 61.6 | 1.6 |
| 30 | 15.5 | 58.7 | 2.6 |
| 40 | 57.5 | 48.4 | 6.9 |
| 50 | 62.5 | 44.6 | 8.0 |

### 2.4.3 Electrostrictive Strain Response

Electrostriction is a secondary coupling in which the relationship between an applied electric field and resulting strain in the material is quadratic.

In a piezoelectric material, both the piezoelectric and electrostrictive responses will be present. The total electromechanical strain, under an electric field $E$ is expressed as:

$$S_{ij} = d_{ijk} E_k + M_{ijkl} E_k E_l \qquad (2.\ 10)$$

where the subscripts $i$, $j$, $k$ and $l$ can have values ranging from 1 to 3. The first term in Eq. (2.10) represents the converse piezoelectric effect with piezoelectric coefficient d, and the second term corresponds to the electrostriction and $M$ is the electrostrictive strain coefficient. In this study, the electric field is applied in the thickness direction and the field-induced strain is also measured in this direction. Thus, it can be simply written as:

$$S = dE + ME^2 \qquad (2.\ 11)$$

For the signal of the sample attributed to the electrostrictive effect, the strain becomes:

$$S = ME^2 \qquad (2.\ 12)$$

When a sinusoidal field $E = E_o \cos(\omega t)$ is applied, then the strain is given by:

$$S = M[E_o \cos(\omega t)]^2 \quad (2.\ 13)$$

Expanding and regrouping Eq. (2.13) leads to:

$$S = \frac{1}{2} M E_o^2 + \frac{1}{2} M E_o^2 \cos(2\omega t) \quad (2.\ 14)$$

where the first term is a constant and is compensated by the feedback arrangement used in the present interferometry technique. Thus, the final expression of electrostrictive coefficient $M$ (measured at a frequency of 2ω) is:

$$M = \frac{2S}{E_o^2} \quad (2.\ 15)$$

where the electrostrictive coefficient $M$ can also be determined from the slope of a straight line plotting the strain $S$ against the square of the applied field $E_o^2$.

In this study, the electrostrictive coefficient $M_{33}$ was measured using a Mach-Zehnder type heterodyne interferometer (SH-120 from B.M. Industries, France) for studying the electro-mechanical responses of the copolymer samples. The

schematic diagram of the experimental setup is shown in Figure 2.9. A function generator (HP8116A) was used to generate an a.c. voltage, which was then amplified by a high voltage amplifier (Trek 662) across the sample.

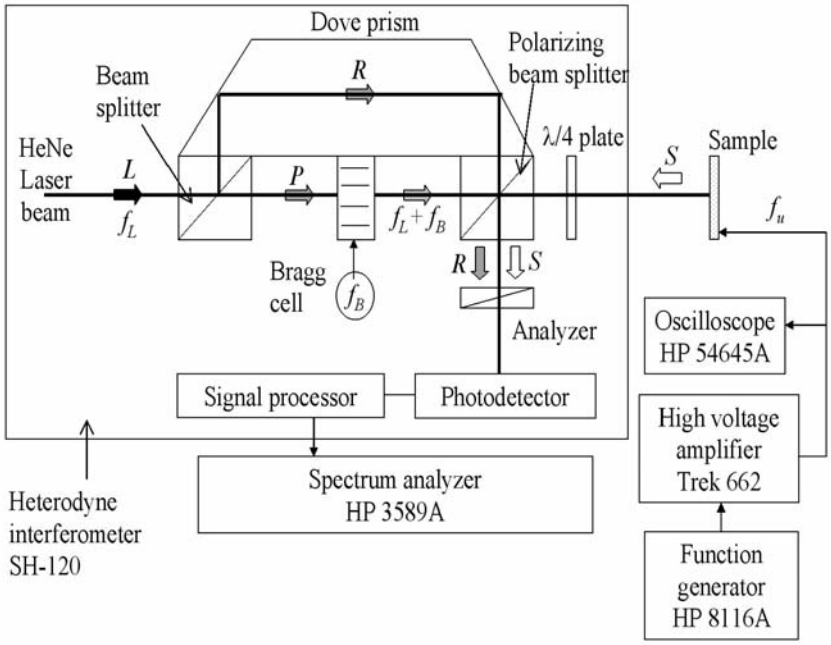


Figure 2.9 Schematic diagram of the experimental setup for electrostrictive measurement.

Refer to Figure 2.9, the linearly polarized laser beam ***L(t)*** with frequency $f_L$ and wavelength $\lambda_L$ (632.8 nm) is delivered by a He-Ne laser to the Mach-Zehnder interferometer. The complex amplitude of the laser beam can be written as:

$$L(t) = Le^{i2\pi f_L t} \qquad (2.16)$$

where $L$ is the amplitude of the laser beam.

The beam L is then split into two paths (reference beam $R$ and a measuring beam $P$) by the beam splitter. The reference beam $R$, after propagating through the Dove prism and the polarizing beam splitter and reaches a photodetector, has a complex amplitude:

$$R(t) = Re^{i2\pi f_L t} \tag{2. 17}$$

where $R$ is the amplitude of the reference beam.

The measuring beam $P$ is transmitted by the beam splitters. Its frequency is shifted by the Bragg cell $f_B$ (70 MHz), so that the frequency of the measuring beam is modulated to $f_L + f_B$. The mechanical displacement of the sample surface generates a modulation of phase of the measuring beam by $\phi(t)$, the measuring beam $P$ reflected by the sample is then label as S:

$$S(t) = Se^{i[(2\pi f_L + 2\pi f_B)t + \phi(t)]} \tag{2. 18}$$

where $S$ is the amplitude of the phase modulated beam $S(t)$ and

$$\phi(t) = \frac{4\pi}{\lambda_L} u \sin(2\pi f_u t) \tag{2. 19}$$

where $u$ is the amplitude of the displacement, and $f_u$ is the vibration frequency.

The interference of the beams $R$ and $S$ on the photodetector delivers a current $I$ beat signal at the frequency of the Bragg cell $f_B$, phase modulation by the mechanical displacement of the sample to the spectrum analyzer:

$$I(t) \propto \cos[2\pi f_B t + \frac{4\pi}{\lambda_L} u \sin(2\pi f_u t)] \quad (2.\ 20)$$

In this study, the current signal $I$ was measured using a spectrum/network analyzer (HP3589A). The current is expanded into a Bessel function series as follows:

$$I \propto \mathrm{Re}\{e^{i2\pi f_B t}[J_0(\frac{4\pi u}{\lambda_L}) + 2iJ_1(\frac{4\pi u}{\lambda_L})\sin(2\pi f_u t) + 2iJ_2(\frac{4\pi u}{\lambda_L})\sin(4\pi f_u t)...]\} \quad (2.\ 21)$$

where $J_n(x)$ is the Bessel function of order $n$, which can be represented in a frequency spectrum as shown in Figure 2.10. The amplitudes of the sidebands represent the phase modulation of the carrier signal at frequency $f_B$ by the vibration at $mf_u$, ($m$ = 1, 2, 3……).

For electrostrictive measurement, signal is attributed to $2f_u$. Therefore, the displacement $u$ can be approximately calculated from recording the ratio value $R_2$ (in dBm) of the current component at $f_B$ and $f_B \pm 2f_u$ providing that u<< λ:

$$R_2 \cong \frac{J_2(\frac{4\pi u}{\lambda_L})}{J_0(\frac{4\pi u}{\lambda_L})} \qquad (2.\ 22)$$

where $J_o$ and $J_2$ are the Bessel functions of the zeroth and the second order, respectively.

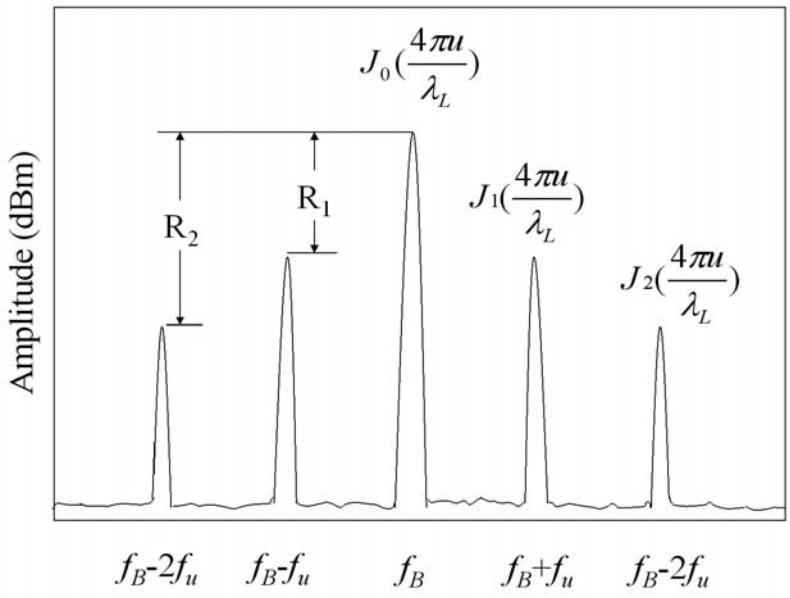


Figure 2.10 The current signal $I$ in the frequency domain as represented in Eq. (2.21).

In the present work, an a.c. field with a frequency of 5 kHz was applied to the sample, the field-induced longitudinal strain was then measured at 10 kHz and the results were plotted as a function of the square of the applied field $E^2$ (Figure 2.11). As expected, the strain is proportional to $E^2$ according to Eq. (2.15). Table 2.2 summarizes the electrostrictive response of the unirradiated and irradiated copolymer films, which shows that the copolymer has a higher electrostrictive coefficient $M_{33}$ after irradiation.

The sample irradiated with a proton dose of 50 Mrad has an electrostrictive coefficient which is six times higher than that of the unirradiated sample. As shown by X-ray diffraction, the crystalline regions in the irradiated sample are in a non-polar phase which has a lattice spacing quite different from that of the polar phase. The transformation between the non-polar and polar phase induced by an electric field gives rise to a large lattice strain and hence a high electrostrictive coefficient. However, as the dose is further increased to 107 Mrad, the crystallinity of the irradiated copolymer decreases, resulting in a reduction in the electrostrictive coefficient.

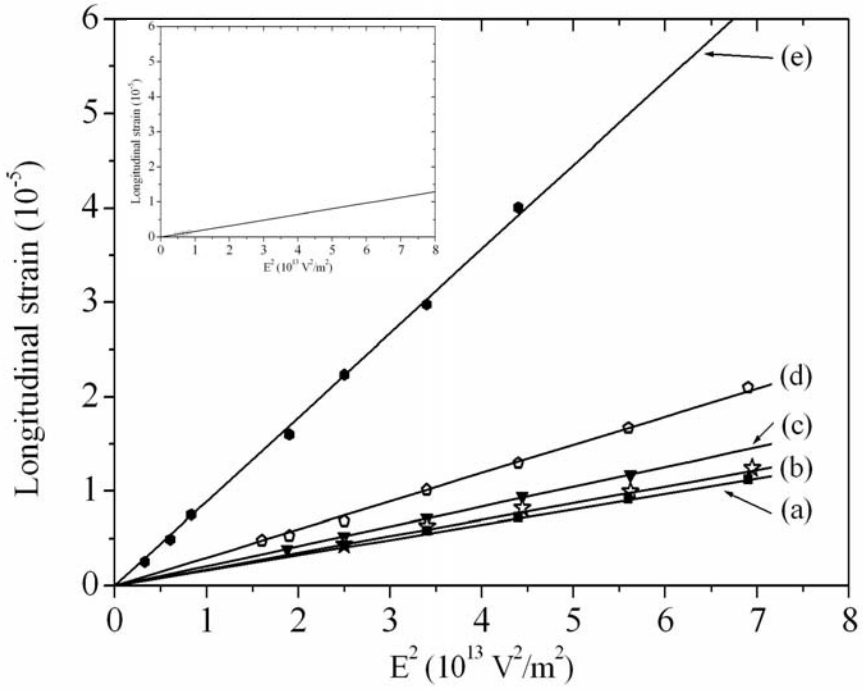


Figure 2.11 Longitudinal strain as a function of the square of the applied field: (a) 10 Mrad, (b) 20 Mrad, (c) 30 Mrad, (d) 40 Mrad, (e) 50 Mrad.
Inset: 0 Mrad (for comparison).

Table 2.2 Electrostrictive coefficient $M_{33}$ of proton irradiated 56/44 mol% P(VDF-TrFE) copolymer films.

| **Proton Dose (Mrad)** | $M_{33}$ **($10^{-18}$ $m^2/V^2$)** |
|---|---|
| 0 | 0.30 |
| 10 | 0.30 |
| 20 | 0.43 |
| 30 | 0.44 |
| 40 | 0.58 |
| 50 | 1.76 |
| 75 | 1.53 * |
| 107 | 0.72 * |
| 150 | 0.40 * |
| 200 | 0.38 * |

* from Lau et al. [2004]

## 2.5 Summary

In this Chapter, the structures and properties of 56/44 mol% P(VDF-TrFE) with low proton doses have been studied in detail. The disappearing of ferroelectric behaviour and the well-fitted V-F law show that a dose of about 50 Mrad of proton irradiation is required to induce a relaxor behaviour without significantly decreasing the crystallinity in 56/44 mol% P(VDF-TrFE) copolymer. Moreover, at a proton dose of 50 Mrad, the copolymer exhibits the highest strain response with an electrostrictive coefficient of $1.76\times10^{-18}$ $m^2/V^2$. From the DSC and XRD data, it is suggested that the formation of defects induced by the irradiation leads to the break-up of the coherent macroscopic domains into nano-regions. As the nano-regions are in the non-polar phase which has a lattice spacing significantly different from that of the polar phase, transformation between the non-polar and polar phase induced by an electric field gives rise to the high electrostrictive strain.

# Chapter 3

# Fabrication of P(VDF-TrFE) MEMS

This Chapter presents a brief description of the fabrication process of polymer microelectromechanical systems (MEMS). A suspended silicon dioxide/silicon membrane was prepared by back-etching the silicon (Si) substrate using potassium hydroxide (KOH). Both 70/30 mol% and 56/44 mol% P(VDF-TrFE) copolymer thin film with thickness of ~2.5 μm was spin-coated on the suspended membrane and poled in situ. When an electric field was applied to the poled copolymer film, it produced displacements in the membrane.

## 3.1 Membrane Fabrication

### 3.1.1 Micromachining

Micromachining is a technique for fabricating microstructures usually by silicon etching techniques. There are two types of etching processes: isotropic and anisotropic. For isotropic etching, the etchant has no preferential etching direction and etches in all crystallographic directions at the same rate. Hydrofluoric acid (HF) used for etching silicon dioxide ($SiO_2$) and silicon nitride ($Si_3N_4$) is a typical etchant used for the isotropic etching process.

On the contrary, anisotropic etching is a process in which the etching rate in a particular direction is substantially higher than those in other directions. Wet etching of silicon using KOH is commonly used for micromachining application, which slows down markedly along the (111) plane of silicon relative to the etch rates along other planes. Figure 3.1 shows the difference between isotropic and anisotropic wet chemically etched cavity geometries using a (100) wafer.

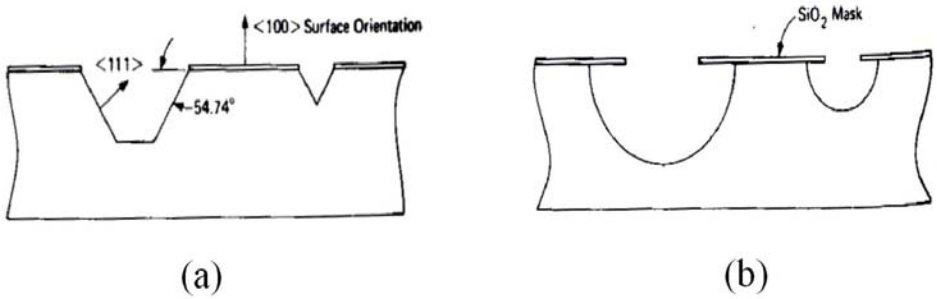


Figure 3.1 A summary of wet chemically etched cavity geometries which are commonly used in micromechanical devices. (a) Anisotropic etching. (b) Isotropic etching with agitation [Petersen, 1982].

It is found that anisotropic etching is a more important technique to shape desired structures with perfectly-defined etched faces which meet at predictable angles in the fabrication of semiconductor devices. The intersection angle $\theta$ between ($hkl$) and ($h_1k_1l_1$) can be found from:

$$\theta = \cos^{-1}\left(\frac{hh_1 kk_1 ll_1}{\sqrt{hh + kk + ll)(h_1h_1 + k_1k_1 + l_1l_1)}}\right) \qquad (3.\ 1)$$

For (100) and (111) planes, this angle is $\tan^{-1}(\sqrt{2}) \approx 54.7^{\circ}$. [Reed et al., 2001]

Because of the slanted (111) planes, the size of the etch mask opening determines the final size of the etched cavity. Figure 3.2 shows geometrically a membrane with side length $x_b$ and desired membrane thickness $h$. The backside window opening length $x$, bounded on the four sloping sides by (111) can be calculated as:

$$x = x_b + 2(T_{Si} - h)\cot 54.7^{\circ} \qquad (3.\ 2)$$

where $T_{Si}$ is the thickness of wafer.

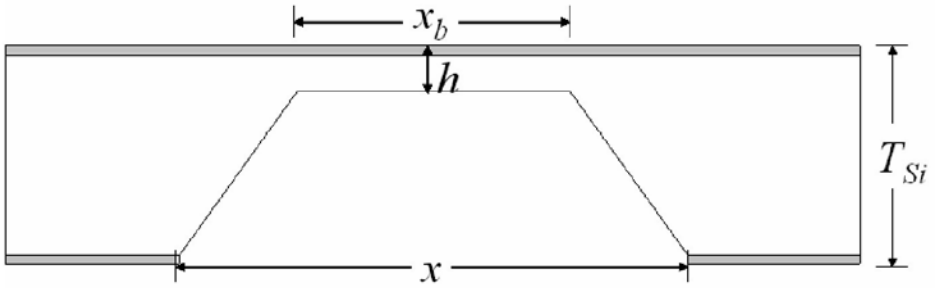


Figure 3.2 Relationship between the dimension of the backside window and thickness of membrane.

### 3.1.2 Etch Mask

The use of etch masks that can selectively prevent regions of silicon from being etched. Silicon dioxide, silicon nitride, and some metallic thin films such as chromium and gold, provide good etch masks for typical anisotropic etchants.

Kendall et al have interpolated KOH etch rates for (100) wafers ($R_{100}$) from various data at different temperatures and KOH concentrations in terms of the hydration model of Glembocki et al. [Glembocki et al., 1991] to relate them by the following equation which applies to ~ 20% over the full range of temperature and KOH concentration [Kendall et al., 1997]:

$$R_{100} = 2.6\times10^{6} W^{2.5} e^{\frac{-(\frac{W}{300}+0.48)}{k(T+273)}} \qquad (3.3)$$

where $R_{100}$ is the etch rate of (100) Si in micrometers per hour, $W$ the actual wt% of KOH in water, $k$ the Boltzmann's constant ($8.617\times10^{-5}$ eV/K) and $T$ is the temperature in degrees Celsius.

Since KOH etches $SiO_2$, an appropriate KOH solution concentration and temperature are chosen to produce an approximate membrane thickness of 20-50 μm and the $SiO_2$ on the backside is thick enough so after the designated etching time, there is still some $SiO_2$ left. Kendall et al also examined various published data for KOH etch

rates of $SiO_2$ at various temperatures and developed an empirical relation that is reported to be about 20% accurate over a very wide range of temperature and KOH concentration:

$$R_{SiO_2} = 2.2\times10^{9} W (1.5\times10^{-4} W^{2.15} + 1) e^{\frac{-(0.795+6\times10^{-6} W^{2.5})}{k(T+273)}} \qquad (3.4)$$

where $R_{SiO_2}$ is the etch rate of $SiO_2$ in micrometers per hour and the other variables are the same as before [Kendall et al, 1997].

Based on the fact that the etch rate for silicon dioxide ($R_{SiO_2}$ = 0.073 μm/h) is considerably smaller than that of silicon ($R_{100}$ = 43.03 μm/h) using 35 wt% KOH etchant at 75 $^{o}$C, a less costly wafer with a silicon dioxide layer as the protective layer during wet etching can be used.

### 3.1.3 Fabrication Process

The fabrication started with silicon wafers covered with 1.3 μm thick silicon dioxide films. A square backside window frame pattern was opened in the silicon dioxide by scratching (Figure 3.3(a)). The patterned-oxide wafer was then anisotropically etched in aqueous 35 wt% KOH solution. The sample was immersed in KOH solution with a water bath controlled at 75 $^{o}$C to remove the Si from the backside to form the desired membrane structure (Figure 3.3(b)). After anisotropic etching of the silicon substrate, the wafer was then thoroughly rinsed in deionized water. Figure 3.4 shows the results of the top view and cross-sectional view of the KOH etched membrane.

## 3.2 Spin-Coating and Fabrication of Electrodes

After releasing the membrane, a 0.1 μm thick aluminum (Al) bottom electrode was deposited by magnetron sputtering onto the top surface of the Si membrane at room temperature (Figure 3.3(c)). Then, ~ 2.5 μm thick P(VDF-TrFE) copolymer (Piezotech Co., Saint Louis, France) film was spun on the top surface of the membrane using a spinner at a rotation speed of 1200 rpm for 30s (Figure 3.3(d)). The copolymer solution used in the spin-coating was formed by dissolving P(VDF-TrFE) pellets in methyl-ethyl-ketone (MEK) solvent at room temperature. The concentration of the solution was ~13 wt%. In order to make contact to the bottom electrode, MEK was

used to remove a small area of the copolymer to expose the bottom electrode. Annealing at 120 $^{o}$C for 2 h was necessary to increase the crystallinity of the copolymer. The sample was irradiated by 3 MeV protons at ambient temperature. After the irradiation treatment, an Al top electrode was deposited by sputtering forming a capacitor structure (Figure 3.3(e)).

Finally, two wires were bonded for subsequent measurements (Figure 3.3(f)). Besides the proton irradiated copolymer MEMS, the piezoelectric copolymer-based membrane has also been prepared. P(VDF-TrFE) films were poled in-situ under an 100 MV/m electric field at room temperature through the capacitor structure, so as to elicit the desired piezoelectric effect of in the copolymer thin films. Figure 3.3 shows the process of MEMS fabrication.

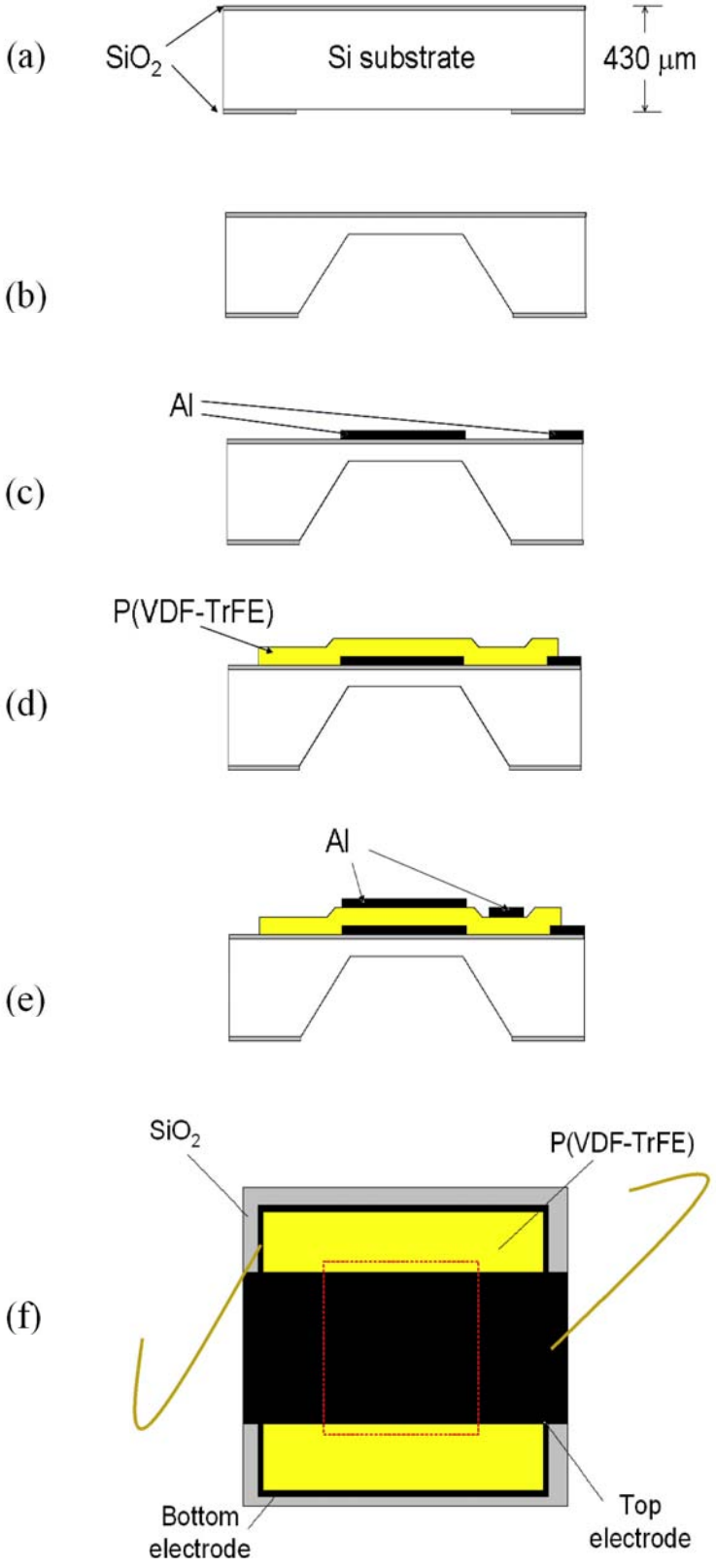


Figure 3.3 Summary of the MEMS fabrication process.

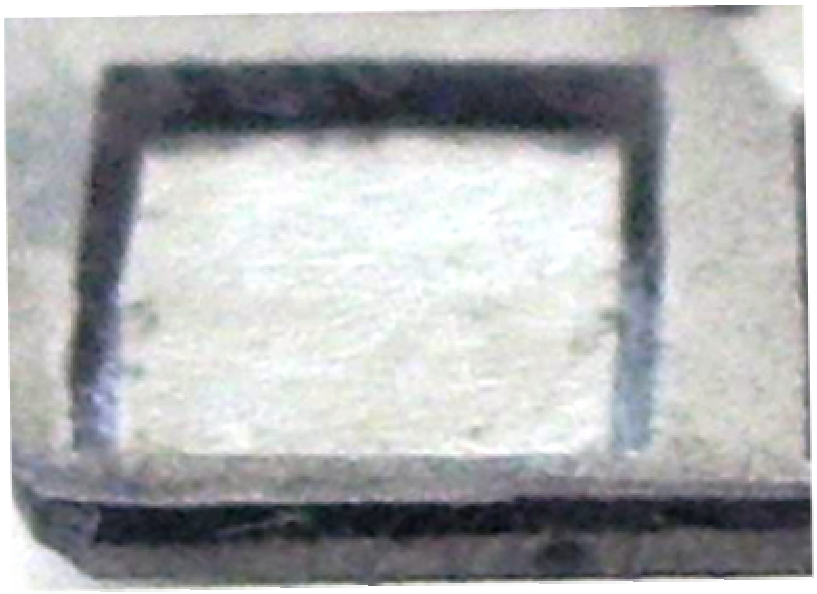

(a)


(b)

Figure 3.4 (a) View of the backside of a membrane. (b) The cross section of a MEMS diaphragm with a 54.7 $^{o}$ angle inclination between the (111) and (100) planes.

# Chapter 4

# Performance of P(VDF-TrFE) MEMS

## 4.1 Introduction

State-of-the-art air-borne ultrasonic transducers radiating ultrasonic energy into air consist mainly of active piezoelectric elements in the form of a disc or ring. The key problem in the design and construction of such transducers is the acoustical coupling of the vibrations from the driving element to the surrounding medium, i.e., air. An obvious method for improving the radiation efficiency of an air-borne ultrasonic transducer is the use of impedance matching layers made of materials with low acoustical impedance. An alternative approach to improve the transducer coupling to air is to use a vibrating membrane.

## 4.2 Electro-Mechanical Measurements

### 4.2.1 Laser Interferometer System

To evaluate the performance of the membrane, the MEMS was driven by an electric field and its surface displacement was measured with a Polytec Laser Doppler Vibrometer (Controller: OFV-3001; Sensor: OFV-303). Figure 4.1 shows a schematic

diagram of the experimental setup for the displacement measurement. The signal from the vibrometer is connected to a digital oscilloscope for recording. Vibration amplitude of the MEMS was detected by the OFV-303 sensor which could be decoded as a voltage signal by the controller and then recorded by the oscilloscope.

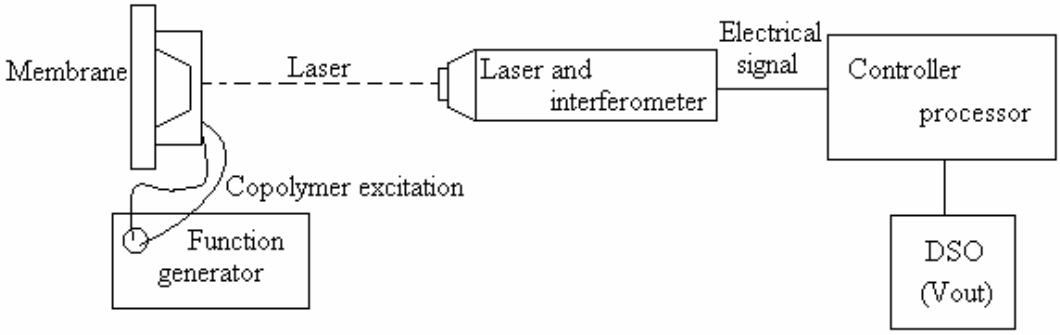


Figure 4.1 Schematic diagram of the experimental setup for the displacement measurements.

The peak displacement $d$ of the vibrating object can be calculated from the equation for a harmonic vibration:

$$d = \frac{V_p s}{2\pi f} \qquad (4.1)$$

where $f$ is the driving frequency, $V_p$ the peak voltage recorded by the oscilloscope and $s$ is the velocity range of the controller.

In the present study, the displacement of the MEMS was measured under different a.c. driving voltages. The frequency response of the MEMS, which covers the resonance frequency and higher order frequency regions were measured, together with their displacement profiles.

### 4.2.2 Identification of Resonance Frequency

The resonance frequency of the membrane-type P(VDF-TrFE) MEMS can be estimated using the equation for a square plate under the mechanical boundary conditions that the four sides are fixed. The fundamental mode frequency for flexural vibrations can be expressed as [Rossing et al., 1994]:

$$f_r = 1.654 \frac{t}{L^2} \sqrt{\frac{Y}{\rho(1-\upsilon^2)}} \qquad (4.2)$$

where $\rho$ is the density, $t$ the thickness, $L$ the length, $Y$ the Young's modulus and $\upsilon$ is the Poisson's ratio. Listed in Table 4.1 are properties of the thin-film materials of the membrane and their material properties.

Table 4.1 Materials properties of thin films in the P(VDF-TrFE) MEMS [Wang et al., 1993; Kim, 1996; Bharti et al., 1998; Xu et al., 1999; Cheeke, 2002; Setter et al., 2002; Lau, 2004].

| **Materials** | **$i^{th}$ layer** | **Thickness (μm)** | **$Y$ (GPa)** | **$\rho$ (kg/m$^3$)** | **$\upsilon$** |
|---|---|---|---|---|---|
| Aluminum (top) | 1 | 0.1 | 68 | 2700 | 0.36 |
| PVDF-TrFE | 2 | 2.5 | 0.7 | 1900 | 0.43 |
| Aluminum (bottom) | 3 | 0.1 | 68 | 2700 | 0.36 |
| Silicon dioxide | 4 | 1.3 | 70 | 2200 | 0.17 |
| Silicon | 5 | 50 | 150 | 2500 | 0.172 |

Assume that the various layers are mechanically connected in series and perfectly bonded, the effective Young's modulus, density and Poisson's ratio can be expressed as:

$$Y = \frac{\sum Y_i t_i}{\sum t_i} \tag{4. 3}$$

$$\rho = \frac{\sum \rho_i t_i}{\sum t_i} \tag{4. 4}$$

$$\upsilon = \frac{\sum \upsilon_i t_i}{\sum t_i} \tag{4. 5}$$

where $t_i$ is the thickness of the $i^{th}$ layer.

According to Eq. (4.2), the resonance frequency of the membrane can be decreased to the audible range (<20 kHz) by either increasing the size of the membrane or decreasing the thickness. The resonance frequency depends heavily on the membrane thickness. For a 3.2 mm square membrane, if the thickness of the membrane is decreased from 60 μm to 40 μm, the resonance frequency will decrease from 75 kHz to 50 kHz as shown in Figure 4.2.

Results of measured values are compared with the value calculated by Eqs. (4.2-4.5). It is found that the measured values are quite close to the calculated values (Figure 4.2).

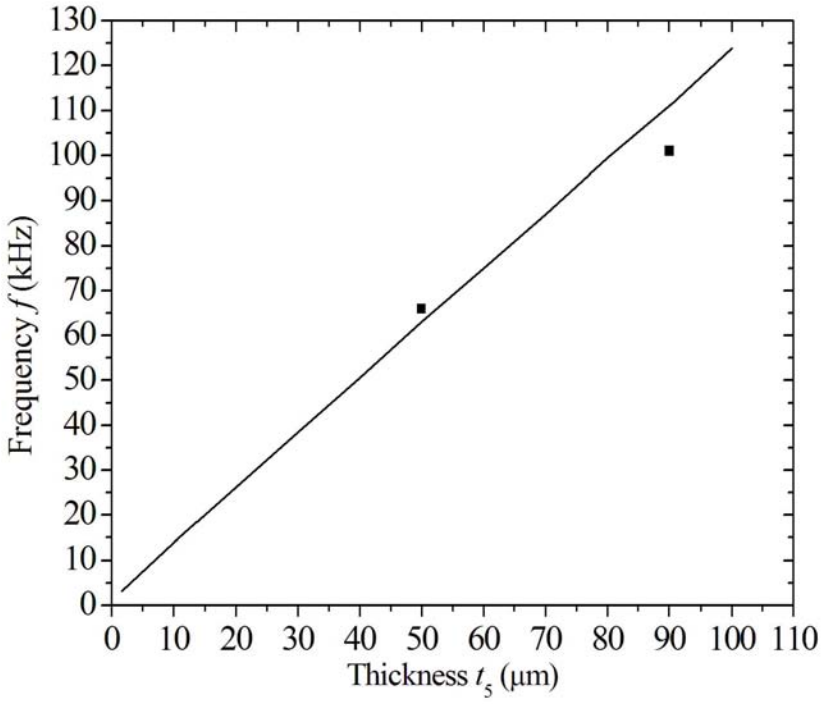


Figure 4.2 Fundamental mode resonance frequency of a 3.2 mm square membrane versus Si membrane thickness. Solid line are values calculated using Eqs. (4.2-4.5). The symbols are measured data.

### 4.2.3 Measurement of Vibrational Amplitude Patterns

#### 4.2.3.1 Study of Frequency Response

70/30 mol% P(VDF-TrFE) MEMS samples with different dimensions have been prepared as listed in Table 4.2. Figure 4.3 shows the displacement at the centre of the membrane as a function of frequency measured using a laser vibrometer. Each MEMS has been driven by a 10 V sinusoidal signal. The vibrational profile depends on the membrane size and thickness. It has been observed that the thicker the membrane, the

higher the resonance frequency, but the smaller the vibration displacement, and it needs higher driving voltage to excite the membrane. The larger the membrane, the easier to drive the membrane, but the resonance frequency becomes lower. For example, the resonance characteristics of sample S6_30 as shown in Figure 4.3(b) has the largest and thinnest membrane, resulting in the lowest resonance frequency.

After the fundamental resonance peak, the MEMS becomes much less efficient at higher frequency resonances. These higher frequency peaks are much weaker. The MEMS thus becomes relatively less efficient at higher frequency regions, especially in a thicker membrane.

Table 4.2 Dimensions of the 70/30 mol% P(VDF-TrFE) MEMS.

| **Sample** | **Square membrane size $L^2$ (mm × mm)** | **Si membrane thickness $t_5$ (μm)** | **Calculated fundamental response frequency $f_r$ (kHz)** |
|---|---|---|---|
| S40 | 2.3 × 2.3 | 18 | 45 |
| S6_30 | 6 × 6 | 30 | 11 |
| S6_50 | 5.8 × 5.8 | 50 | 19 |
| S3_50 | 3.2 × 3.2 | 50 | 63 |
| S3_90 | 3.2 × 3.2 | 90 | 111 |

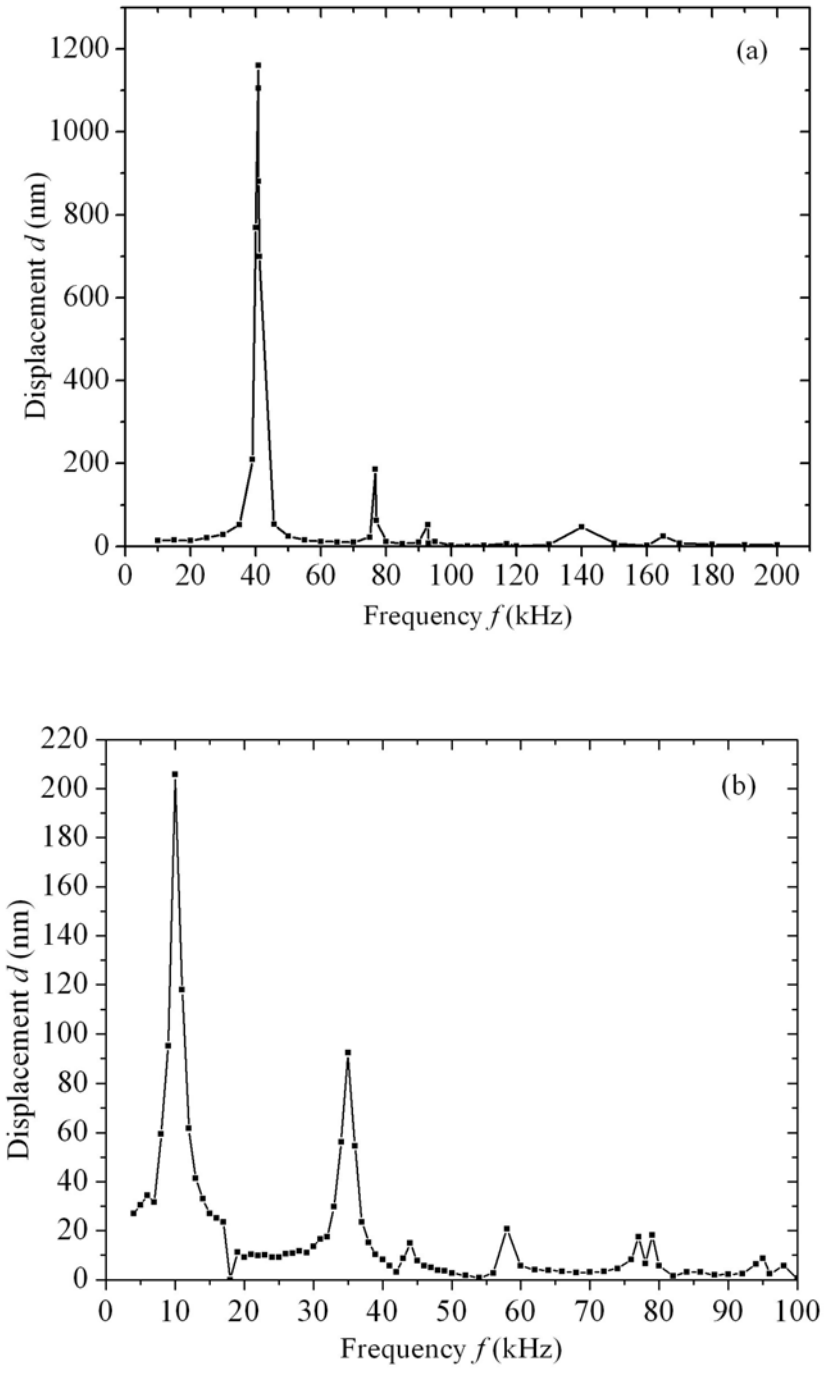


Figure 4.3 Variation of vibrational amplitude with frequency at the centre of membranes with different membrane sizes and thicknesses: (a) S40, (b) S6_30, (c) S6_50, (d) S3_50 and (e) S3_90.

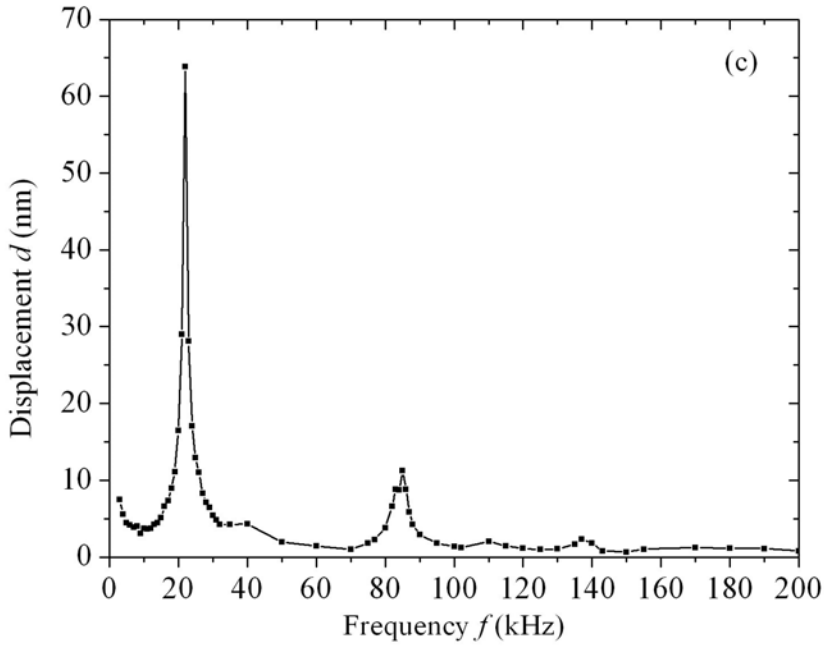


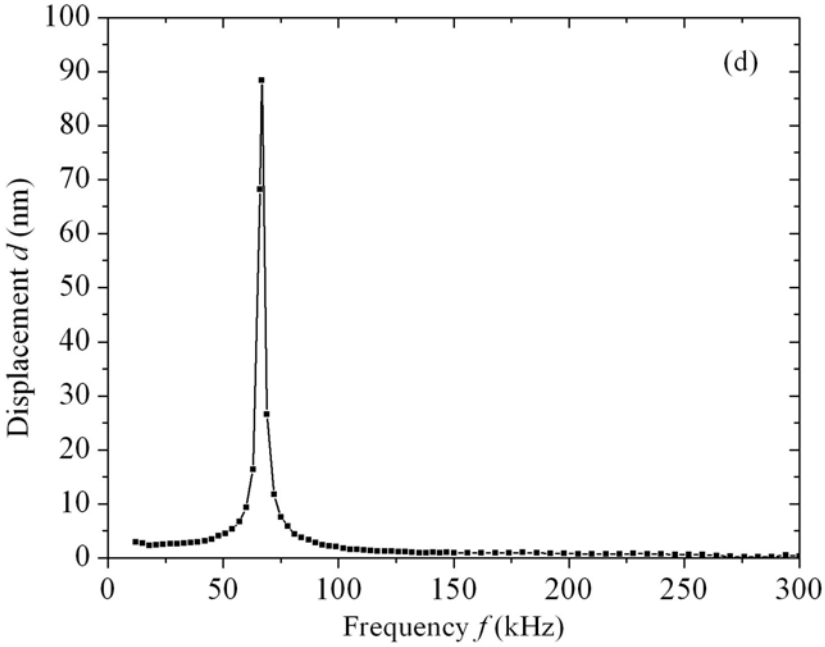


Figure 4.3 (Continued).

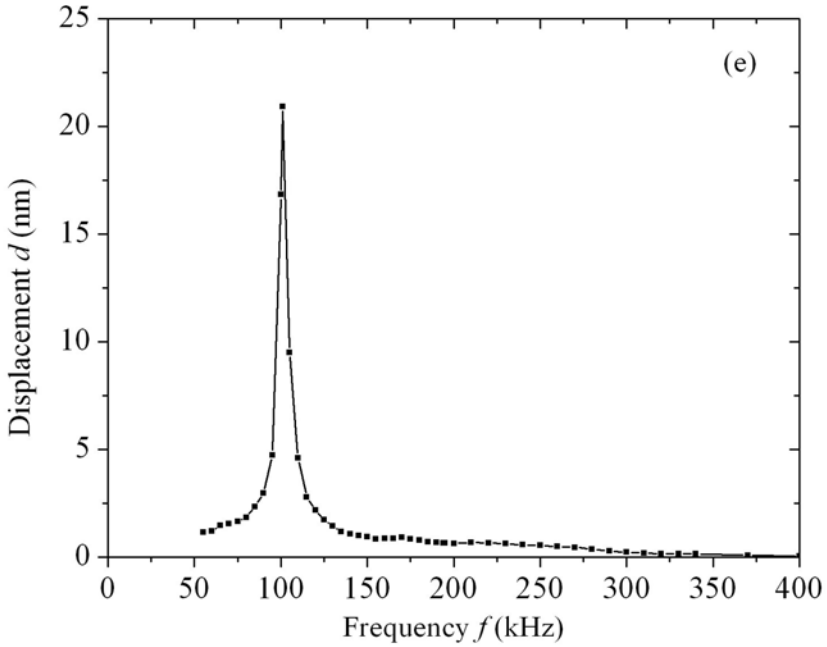


Figure 4.3 (Continued).

### 4.2.3.2 Study of Displacement Profiles

Figure 4.3(a) shows a fundamental resonance peak of sample S40 at 40.8 kHz. The excitation voltage is 10 V. Distribution of the vertical (or out-of-plane) displacement amplitude across the membrane of S40 has been studied at different resonance peaks corresponding to the fundamental resonance (at 40.8 kHz) and the second and third harmonics (92.9 kHz and 140 kHz), respectively (Figure 4.4).

A.c. voltages were used to excite the membrane. At each frequency, the amplitude of the a.c. voltage increased from 4 V to 10 V. It is clearly seen that the displacement increases quite linearly with increasing voltage as shown in Figures 4.5 and 4.6. The centre displacements per unit voltage are 110 nm/V, 0.8 nm/V and 5 nm/V at 40.8 kHz,

92.9 kHz and 140 kHz, respectively. The displacement at the centre of the membrane at 92.9 kHz becomes very small as the centre is a displacement antinode at the second harmonic resonance.

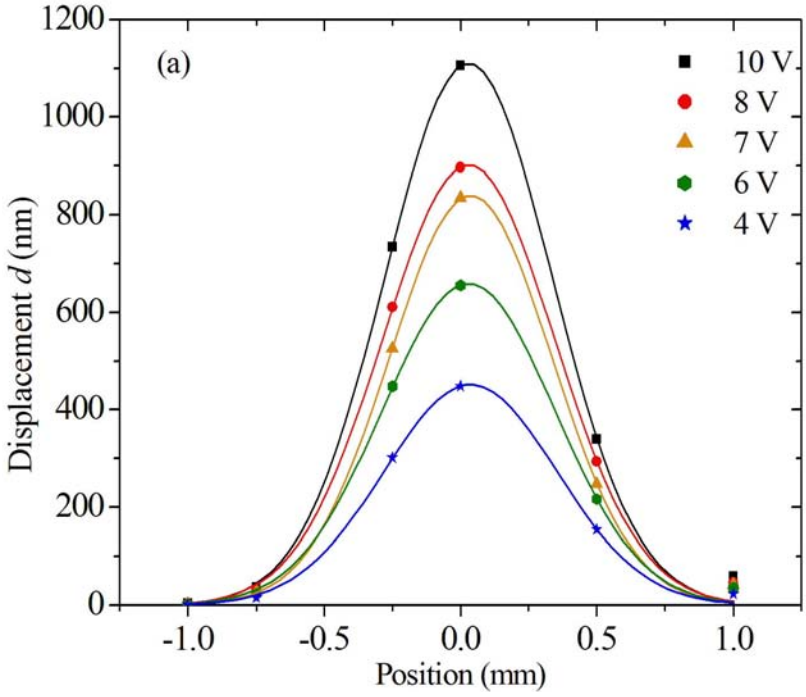


Figure 4.4 Vibration of amplitude profiles on membrane S40 at (a) 40.8 kHz, (b) 92.9 kHz and (c) 140 kHz.

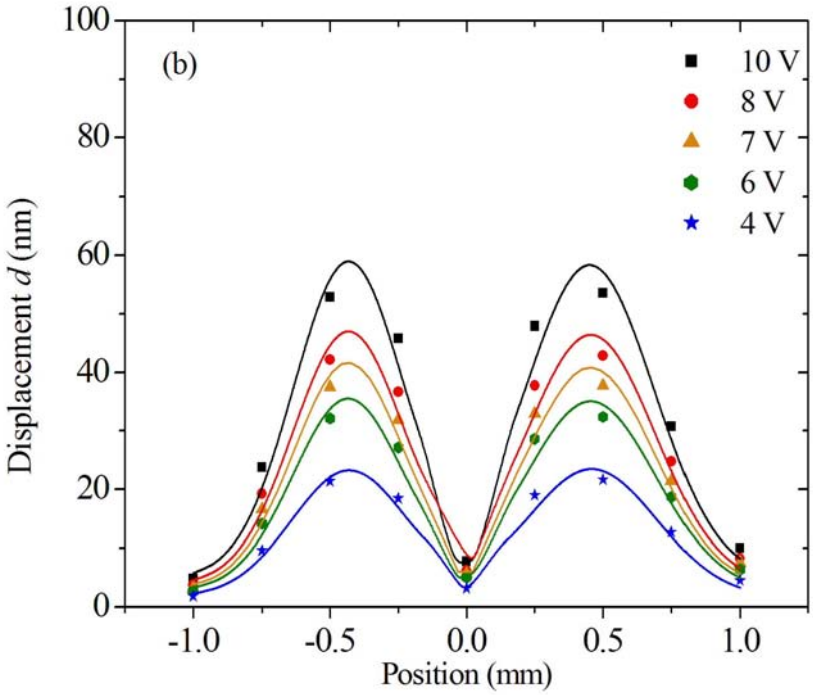


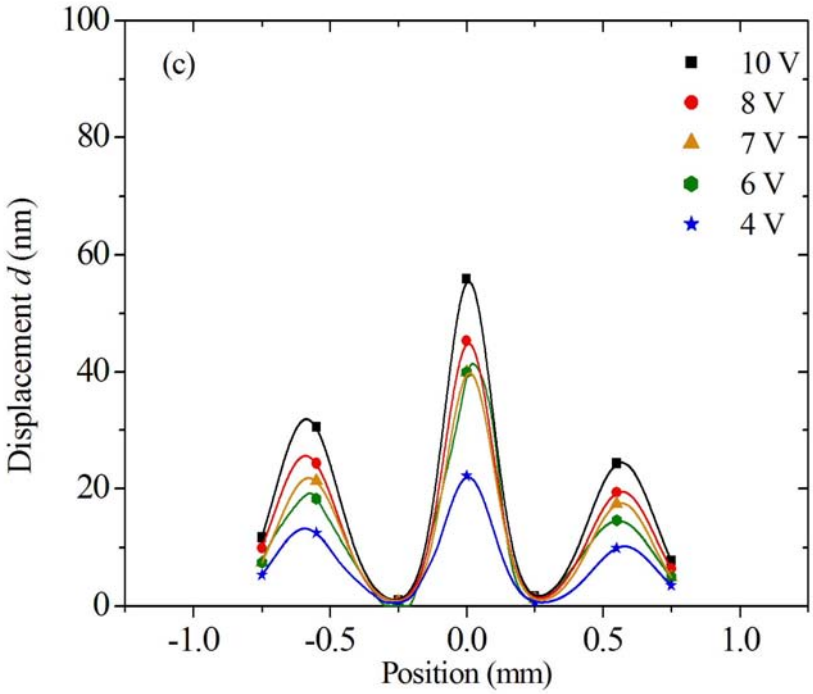


Figure 4.4 (Continued).

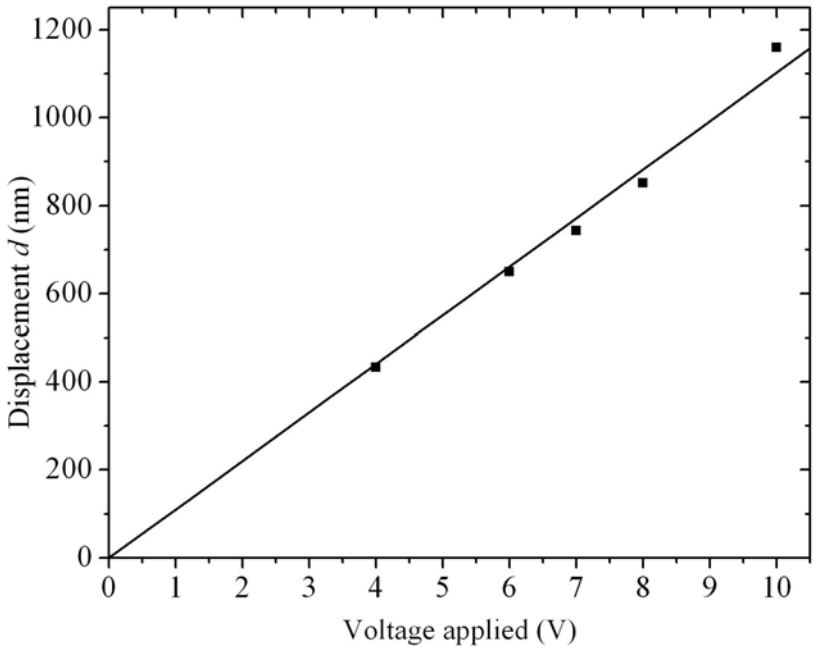


Figure 4.5 Vibration in amplitude of the MEMS as a function of excitation voltage at 40.8 kHz.

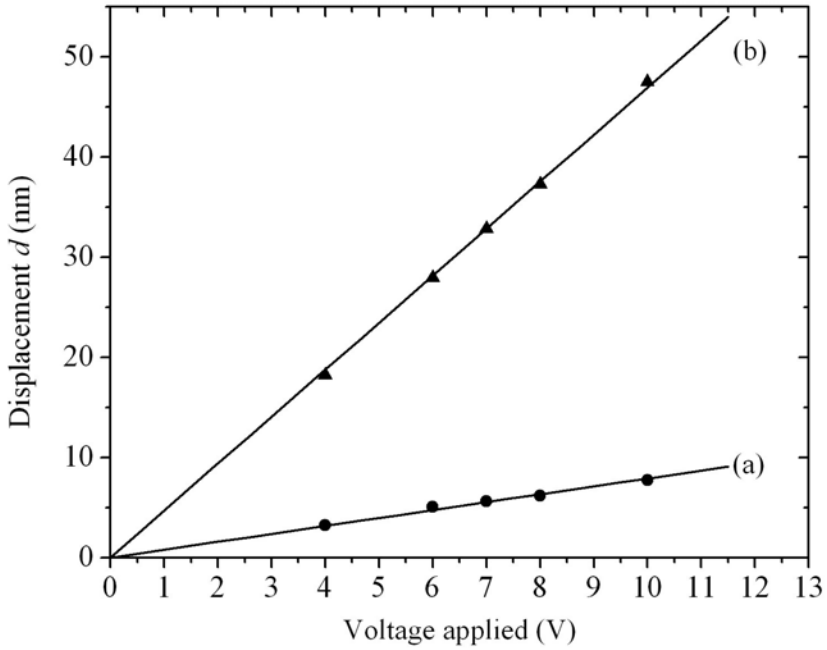


Figure 4.6 Vibration in amplitude of the MEMS as a function of excitation voltage at (a) 92.9 kHz and (b) 140 kHz.

### 4.2.4 Acoustic Pressure Transmitted by the P(VDF-TrFE) MEMS

The acoustic pressure transmitted by the MEMS was studied using a B&K microphone (Type 4135) having an outer diameter of 6.35 mm (1/4 in) with a known sensitivity of 3.8 mV/Pa (supplied by the manufacturer). The microphone was connected to a B&K measuring preamplifier (Type 2633). The MEMS and the microphone were positioned to face one another on an optical bench.

Variation of acoustic pressure with frequency has been studied at a far field axial point *z* of the MEMS:

$$z = \frac{a^2}{\lambda} \tag{4. 6}$$

and

$$a = \frac{L}{2} \tag{4. 7}$$

where *z* marks the transition between the near and the far zones, *L* is the length of the MEMS and $\lambda$ is the wavelength at the operating frequency. For the sample S40 with 2.3 mm square membrane, it is calculated that the transition between the near and the far zones operating at 40.8 kHz is at 0.16 mm. The acoustic pressure vs frequency of S40 at an axial distance of 13 mm is shown in Figure 4.7. The MEMS, driven by 10 V, produces the maximum pressure at 40.8 kHz, which is consistent with that obtained in the displacement pattern. Electro-mechanical response of the MEMS agrees with the

pressure in giving a maximum response at resonance. The peak pressure level generated as a function of excitation voltage at an axial distance of 13 mm from the MEMS surface shows a linear relationship as shown in Figure 4.8. From the slope of the line, it is found that the transmitting response of the MEMS at 40.8 kHz is ~ 0.1 Pa/V.

In the far field, the intensity of the acoustic waves along the axis varies as the inverse of the square of the distance from the transducer. Axial variation of acoustic pressure generated by the MEMS is shown in Figure 4.9. It is found that the pressure falls with distance following the inverse square law (shown by the solid line).

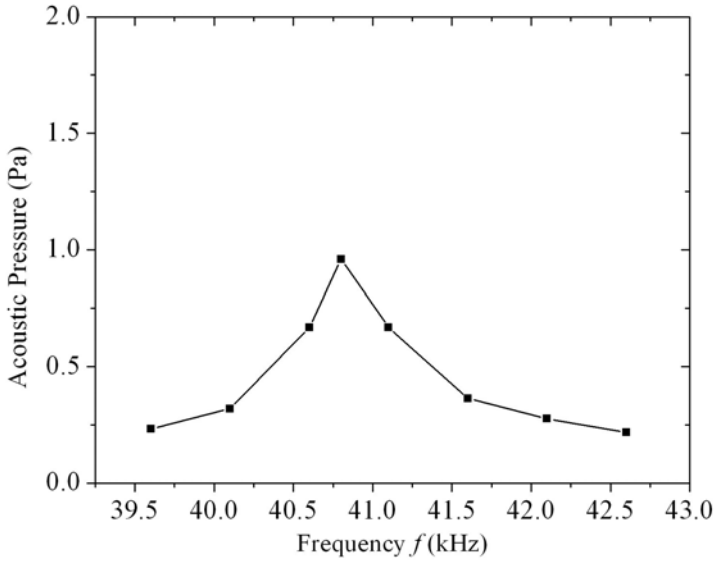


Figure 4.7 Acoustic pressure of the MEMS driven by 10 V at an axial distance of 13 mm.

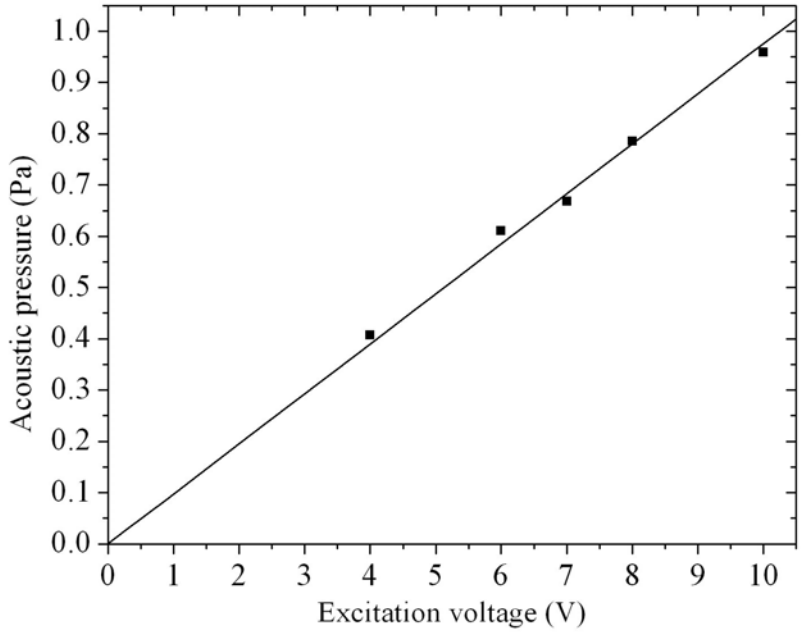


Figure 4.8 Acoustic pressure generated at 40.8 kHz under different excitation voltages measured with a B&K microphone at 13 mm from the MEMS.

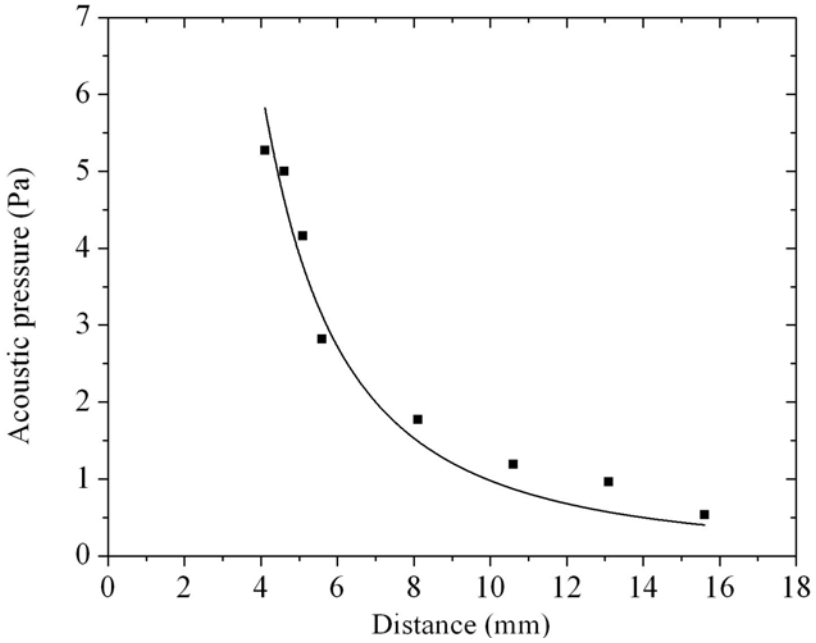


Figure 4.9 Axial distribution of acoustic pressure (symbols) of the MEMS driven by a 10 V sinusoidal source (the solid line corresponds to the inverse square law).

## 4.3 Receiving Sensitivity of the P(VDF-TrFE) MEMS

Characteristics of the output voltage of the S40 MEMS when used as a receiver and subjected to an input ultrasonic acoustic pressure has been studied. Sensitivity of the copolymer based MEMS as an ultrasonic sensor can then be evaluated.

The receiving response of the MEMS is measured by a comparison method using a B&K microphone (Type 4135) having an outer diameter of 6.35 mm (1/4 in) with a known sensitivity of 3.8 mV/Pa (supplied by the manufacturer). The microphone was connected to a B&K measuring preamplifier (Type 2633). Figure 4.10 shows the test equipment of the MEMS mounted on an optical bench facing an air-borne ultrasonic transducer.

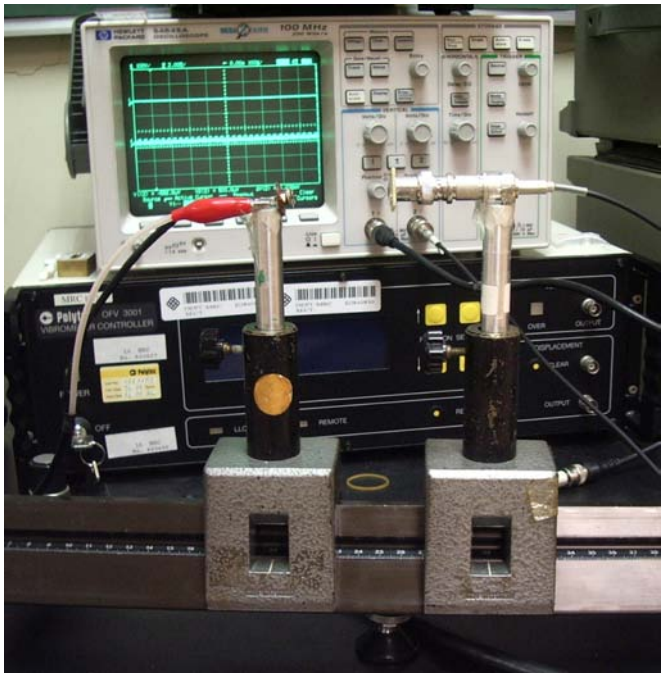

Figure 4.10 Schematic setup of the MEMS (right) facing the air-borne ultrasonic transducer (left) aligned on an optical bench.

The air-borne ultrasonic transducer has a resonance frequency of ~ 40 kHz and was used as the emitter. It is driven by a 5 cycle tone burst signal of 10 ms duration with a driving voltage of 10V at 40.8 kHz provided by an HP8116A function generator to produce an acoustic pressure. The B&K microphone was placed in front of the ultrasonic transducer at 4 cm, where the variation of acoustic pressure as a function of input voltage was recorded and shown in Figure 4.11.

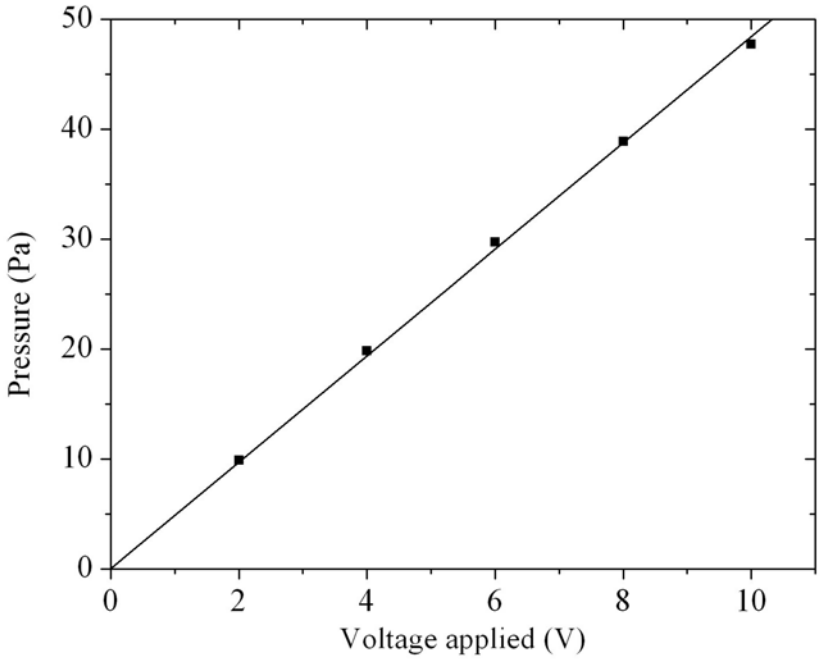


Figure 4.11 Acoustic pressure of the ultrasonic transducer (source) driven at 40.8 kHz and under different voltages at an axial distance of 4 cm.

With the above setup, acoustic pressure at 40.8 kHz on the axis of the MEMS 4 cm from the microphone was measured. The response of the MEMS transducer at different input acoustic pressure was tested.

Figure 4.12 shows the voltage output of the membrane as a function of acoustic pressure generated by the transducer at 40.8 kHz. As acoustic pressure increases from 10 Pa to 48 Pa, the voltage output increases from about 0.8 mV to 3.6 mV. Figure 4.13 shows the unamplified output voltage from the S40 MEMS acoustic sensor and the corresponding frequency spectrum. It shows that the ringdown time of the MEMS is quite long and the frequency of the signal is predominantly 40.8 kHz.

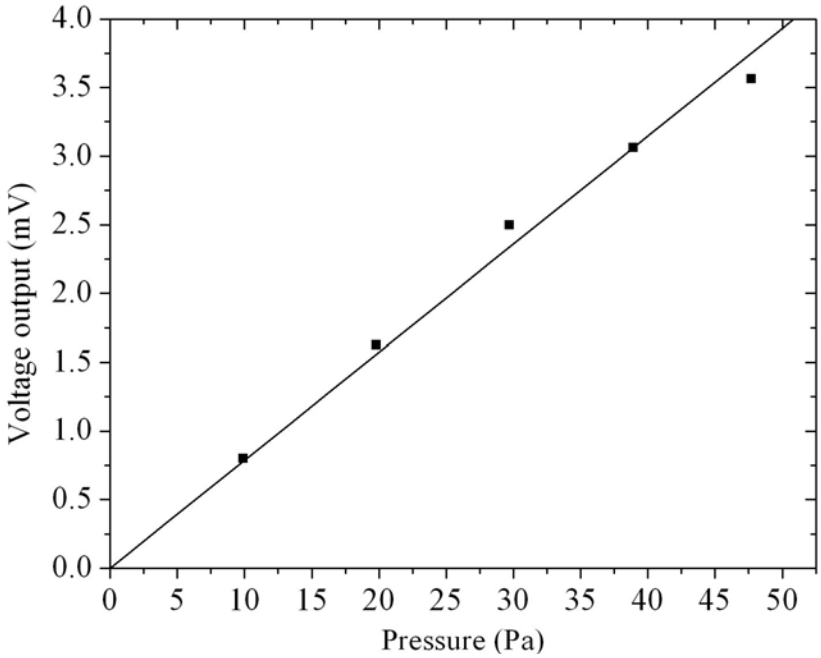


Figure 4.12 Voltage output of the S40 MEMS as a function of acoustic pressure generated by a transducer at 40.8 kHz at an axial distance of 4 cm.

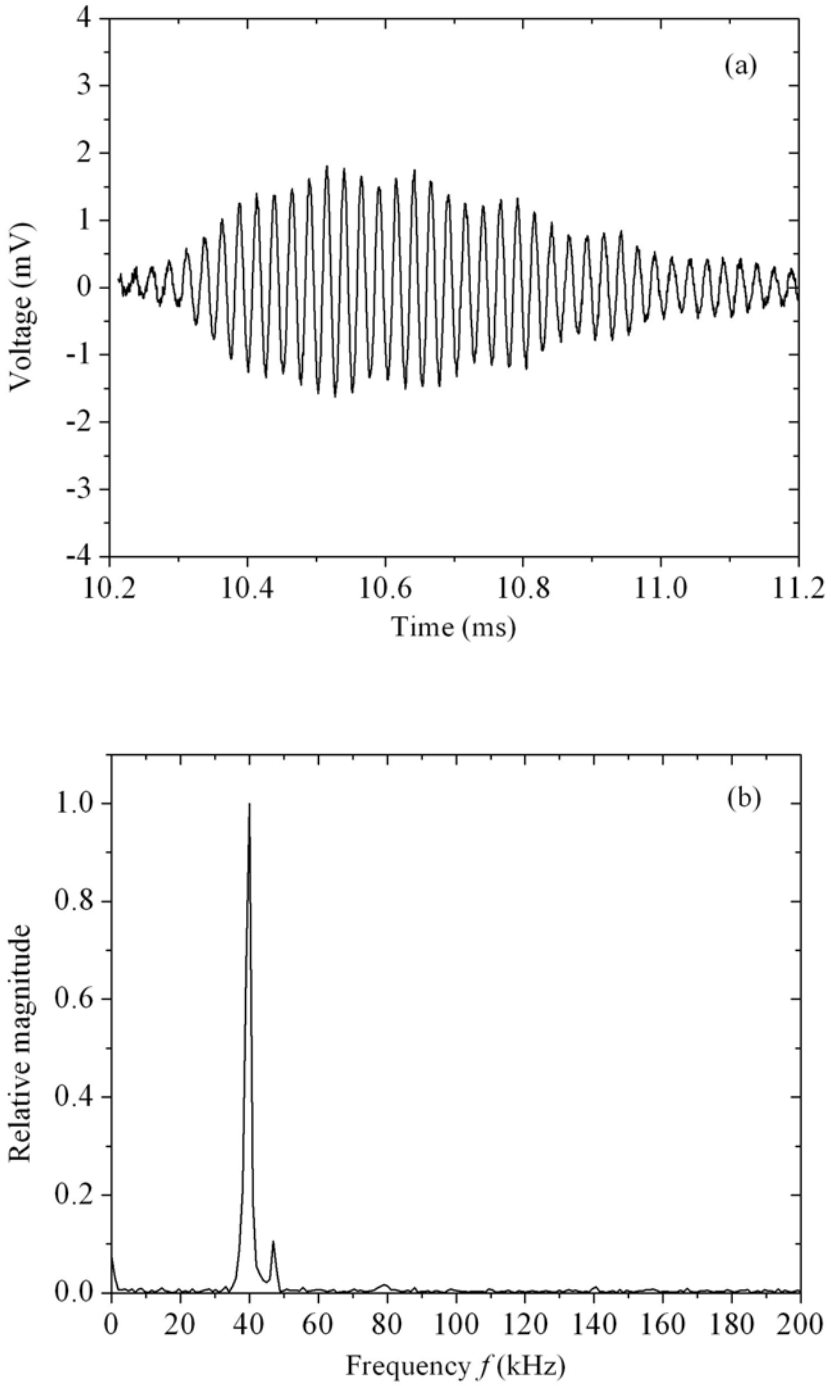


Figure 4.13 (a) Temporal response and (b) frequency domain response of the S40 MEMS when the transmitting transducer is subjected to a 5-cycle tone-burst signal at 40.8 kHz.

The B&K microphone was first used to measure the acoustic pressure generated by the transducer. The S40 MEMS transducer was then substituted for the microphone, with the acoustic centre placed in the field exactly at the position of the microphone. The unamplified output voltage of the S40 MEMS, corresponding to the known acoustic pressure, is then measured, and the acoustic transducer sensitivity is calculated and shown in Figure 4.14. It is noted that the response is quite linear under various acoustic pressure. At the resonance frequency of 40.8 kHz, sensitivity of the S40 MEMS transducer under different pressure is ~ 84 μV/Pa.

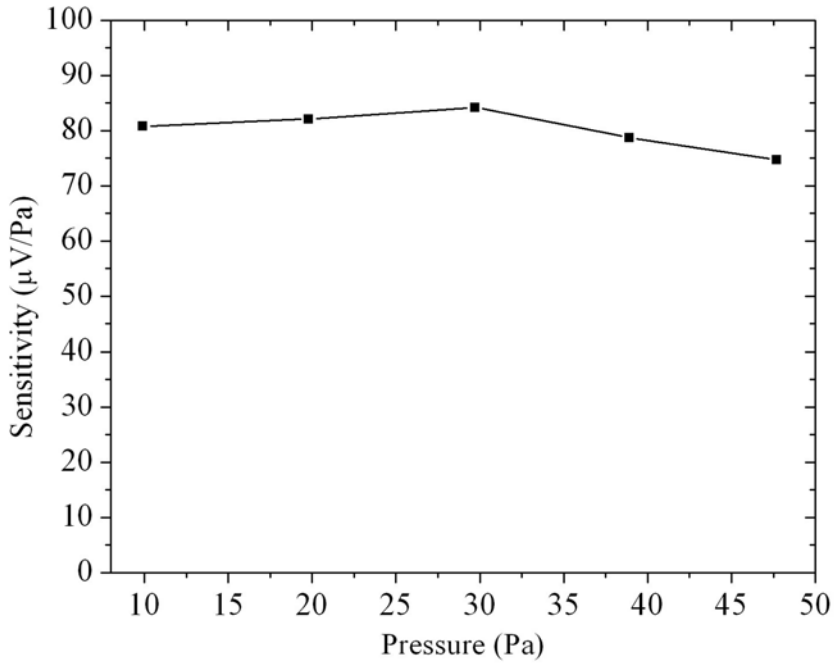


Figure 4.14 Receiving sensitivity of the S40 MEMS under various acoustic pressure at 40.8 kHz.

# Chapter 5

# Study of Clamping Effect on the Electrostrictive Coefficient of 56/44 mol% P(VDF-TrFE)

A film mounted on a substrate is constrained in the plane of the substrate. Due to this clamping effect, the strain in the thickness direction is reduced and thus the measured $M_{33}$ is smaller than the true value of the bulk material.

Unirradiated and irradiated 56/44 mol% P(VDF-TrFE) copolymer thin films deposited on Si substrates were studied to reveal the effect of clamping. Following the process described in Chapter 3 on MEMS Fabrication, a set of 6 MEMS were spin-coated with ~ 2.1 μm copolymer thin film on silicon substrates and by back-etching a 3 mm × 3 mm square Si membrane was formed in each MEMS. The thickness of the Si left on the membrane was controlled to ~ 55 to 60 μm for all the MEMS samples and the calculated resonance frequency using Eqs. (4.2-4.5) is ~ 80 to 87 kHz. In order to ensure the consistency for direct comparison between the unclamped and clamped $M_{33}$, the irradiation conditions were identical to those of bulk film samples studied in Chapter 2. The proton doses were in the range of 10 to 50 Mrad.

Similar to the measurement in bulk samples, a Mach-Zehnder type heterodyne laser interferometer (SH-120 from B.M. Industries, France), as shown in Figure 2.9, was used

to measure the electrostrictive strain of the thin films. The field-induced longitudinal strain was measured at 10 kHz with an a.c. driving voltage of 5 kHz applied to the copolymer thin film. The effective electrostrictive coefficient $M_{33}$ was calculated according to Eq. (2.15), which can be determined by 2 times the slope of the straight line plotting the strain $S$ against the square of the applied filed $E^2$.

For the measurement of the electrostrictive coefficient $M_{33}$ of thin films one has to keep in mind that the film is clamped to a substrate. Therefore, the ratio of strain $S$ and electric field $E$ does not represent the $M_{33}$ of the free sample but gives only an effective coefficient (effective $M_{33}$).

Effective $M_{33}$ was measured as a function of frequency at the centre of the membrane $M_{membrane}$ and at the side on the silicon substrate $M_{Si}$ as shown in Figure 5.1. Near the centre of the membrane, some Si has been etched away, hence $M_{membrane}$ represents a partially clamped boundary condition while $M_{Si}$ represents a state in which the P(VDF-TrFE) thin film is completely clamped.

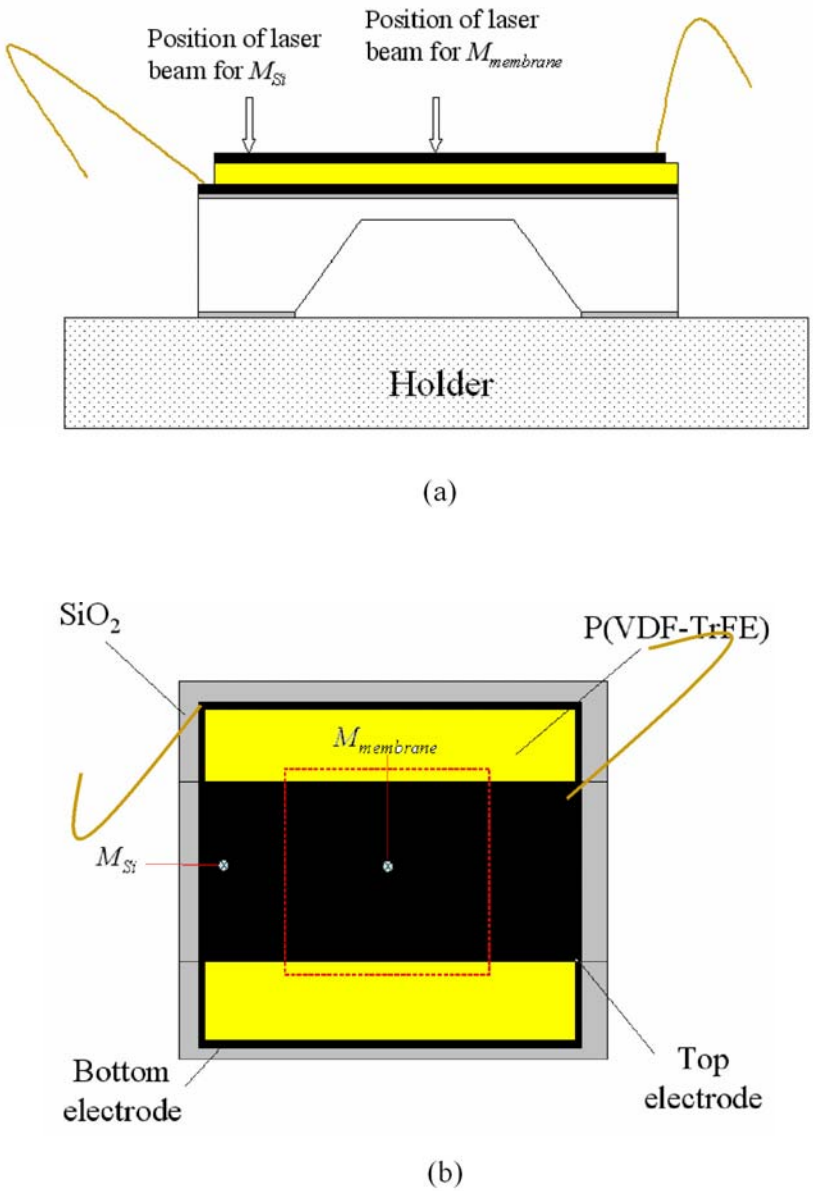


Figure 5.1 Schematic diagram of (a) side view and (b) top view, showing the measurement of effective $M_{Si}$ and $M_{membrane}$ with the Mach-Zehnder type heterodyne laser interferometer.

Figure 5.2 shows the displacement at the centre of the unirradiated 56/44 mol% P(VDF-TrFE) membrane as a function of applied frequency $f$. For electrostrictive measurement, signal is attributed to $2f$. The amplitude of the driving a.c. voltage is 20 V. It is found that the displacements remain almost unchanged as the applied frequency $f$ increases from 5 kHz to 20 kHz at 20 V excitation voltage. At $f$ ~ 40 kHz, the displacement reaches a maximum value of 0.54 nm. It may be due to the resonance of the membrane at $2f$ ~ 80 kHz, and the bending of membrane amplifying the 'measured' effective $M_{33}$. To stay away from the resonance frequency of the membrane, the electrostrictive strain was measured at 5 kHz which is far below the resonance frequency. Figure 5.3 shows the electrostrictive strain $S$ as a function of the square of the applied field $E^2$ obtained in the unirradiated and irradiated 56/44 mol% P(VDF-TrFE) MEMS sample. The $M_{Si}$ and $M_{membrane}$ are calculated by 2 times the slope.

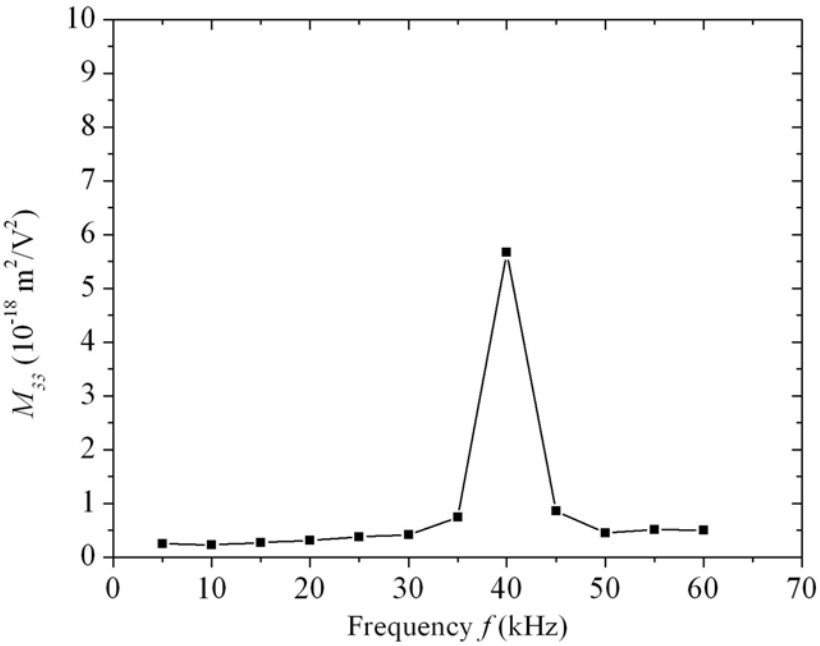


Figure 5.2 The displacement at the centre of the unirradiated sample as a function of frequency at 20 V excitation voltage.

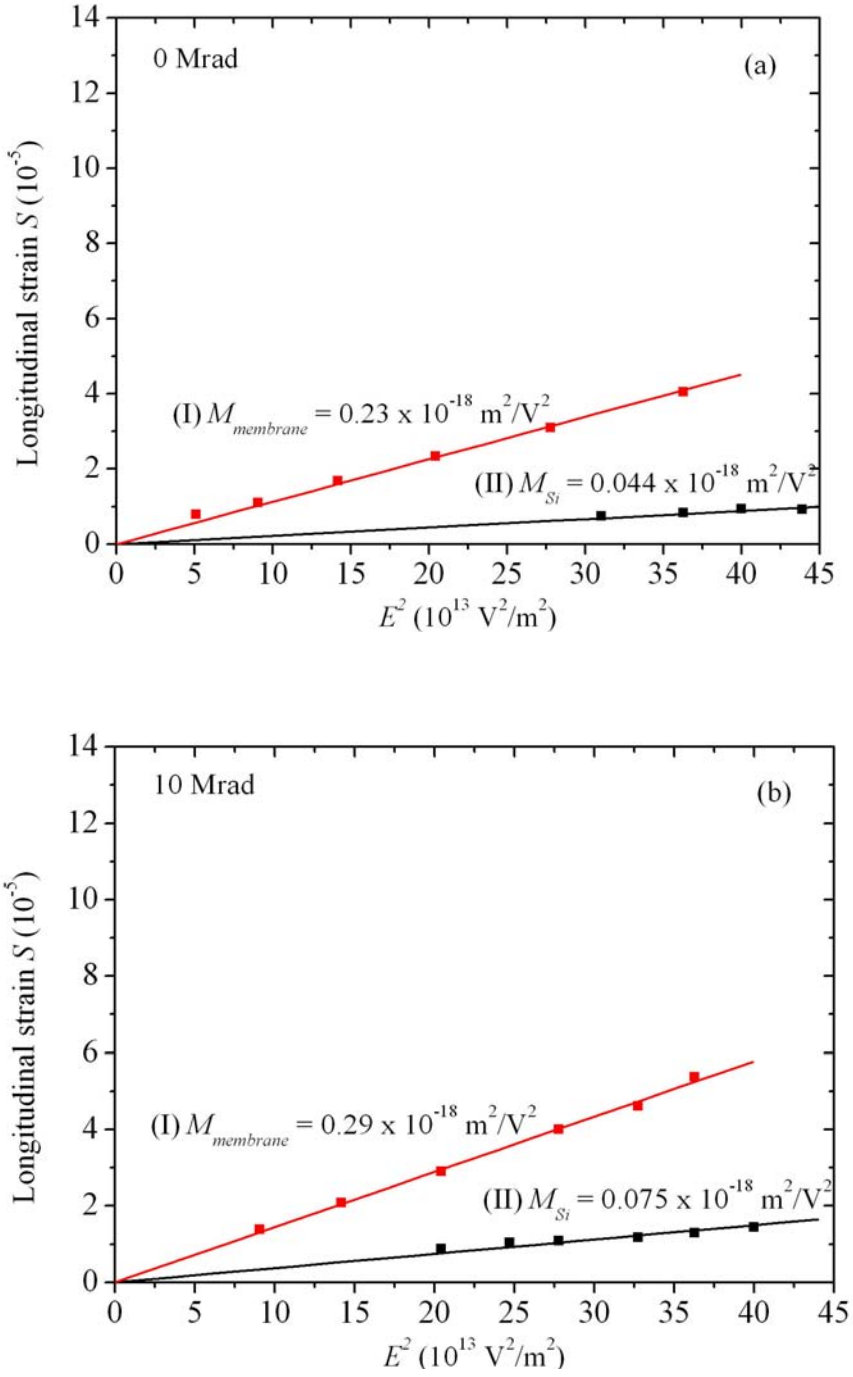


Figure 5.3 Longitudinal strain as a function of the square of the applied field of (a) unirradiated, (b) 10 Mrad, (c) 20 Mrad, (d) 30 Mrad, (e) 40 Mrad and (f) 50 Mrad proton irradiated 56/44 mol% P(VDF-TrFE) at position (I) at the centre of the membrane and (II) at the side on the Si substrate.

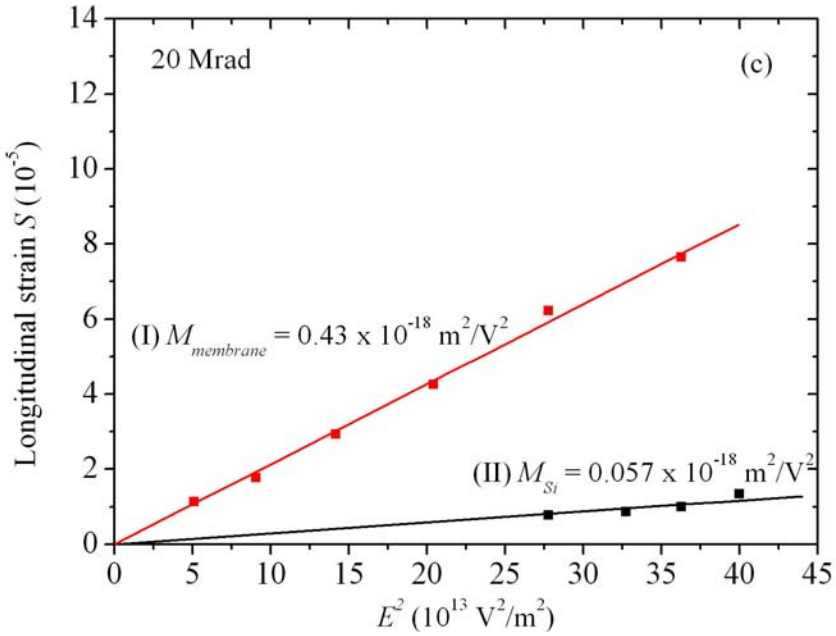


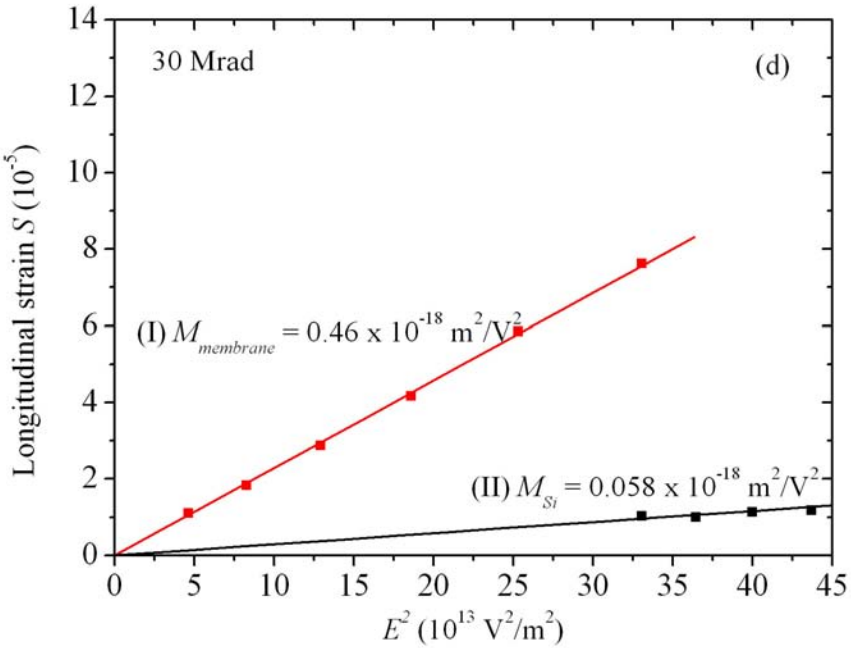


Figure 5.3 (Continued).

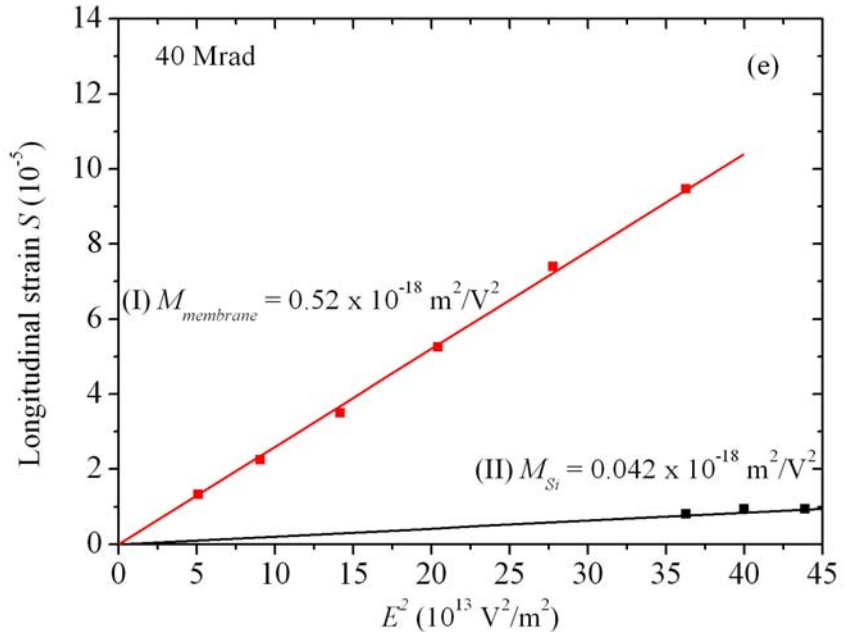


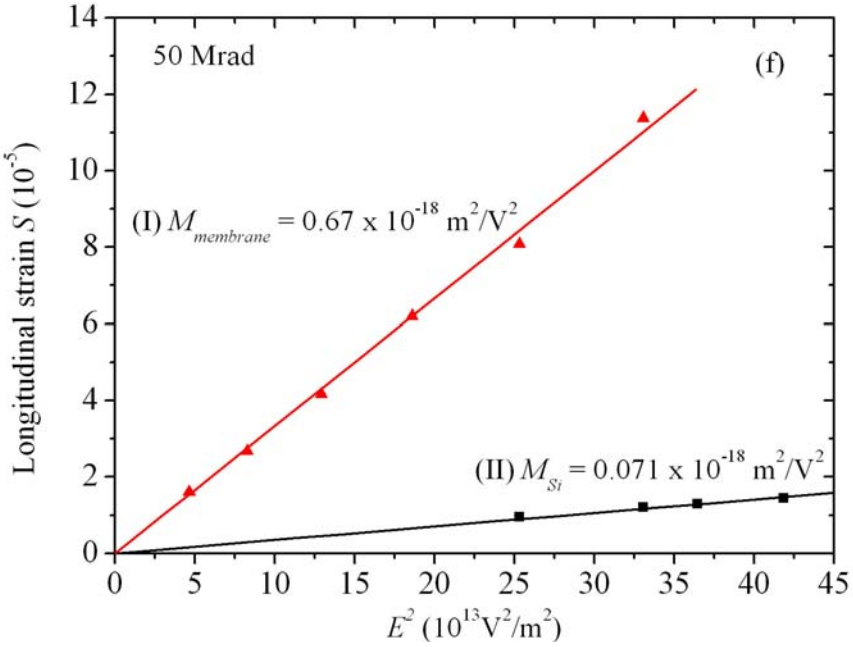


Figure 5.3 (Continued).

The $M_{33}$ of the free bulk samples and the effective $M_{33}$ of MEMS of unirradiated and irradiated copolymers are summarized in Figure 5.4. It is observed that $M_{membrane}$ is increased by about an order magnitude when the Si substrate is thinner. It can be observed that $M_{membrane}$ increases gradually as proton dose increases, but does not exhibit significant increases at 50 Mrad as in the bulk free sample. This may probably be due to the existence of a thin layer (~ 50 to 60 μm) of Si substrate, which imposes partial clamping to the soft copolymer film and impedes the free vibration of the membrane. Although the applied field is in the thickness direction, the film movement in the thickness direction also causes bending of the membrane. In this case, the bending of the membrane may dominate the substrate clamping effect.

Therefore, $M_{Si}$ reveals the actual strain response in the thickness direction, as the Si substrate is fixed to the holder of the electrostrictive measurement setup. Comparing the effective $M_{Si}$ with the $M_{33}$ of the free bulk films, the $M_{Si}$ is reduced by one order of magnitude, as one face of the film is rigidly clamped to a thick Si substrate. This constraint limits the movement of the copolymer layer as it attempts to expand or contract when a voltage is applied.

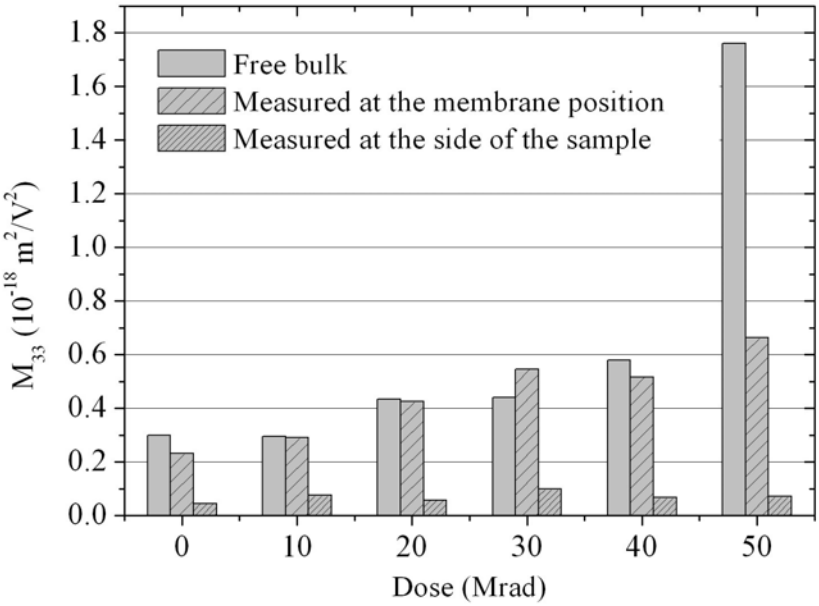


Figure 5.4 Comparison of the values of clamped and free bulk $M_{33}$. *(Remark: The unusual behaviour at 30 Mrad may be due to the variation in irradiation dose received by the two samples.)*

# Chapter 6

# Conclusions

The effect of 3 MeV proton irradiation at a low proton dose range from 10 to 50 Mrad on the structure and property of 56/44 mol% poly(vinylidene fluoride-trifluoroethylene) copolymers [P(VDF-TrFE)] have been studied. At low doses, the high energy proton irradiation has already induced changes on the relative permittivity, polarization hysteresis, electrostrictive strain response and phase transition behaviour.

The proton irradiation, even at a low proton dose of 10 Mrad, changes the polarization hysteresis loop of the copolymer from one with a large hysteresis to a slimmer loop. Also, the well-fitted V-F law showed that a low dose (10 Mrad) of proton irradiation is sufficient to induce a partial relaxor behaviour without significantly decreasing the crystallinity in 56/44 mol% P(VDF-TrFE) copolymer.

From the DSC and XRD data, it is suggested that the formation of defects induced by the irradiation leads to the break-up of the coherent macroscopic domains into nano-regions. As the nano-regions are in the non-polar phase which has a lattice spacing significantly different from that of the polar phase, transformation between the non-polar and polar phase induced by an electric field gives rise to the high

electrostrictive strain. In previous work [Lau et al., 2004], the maximum $M_{33}$ obtained at a dose of 75 Mrad is $1.53 \times 10^{-18}$ $m^2/V^2$. Hence, 50 Mrad is the optimum proton dose as it can produce an electrostrictive strain of $1.76 \times 10^{-18}$ $m^2/V^2$, which is higher than that reported in the previous work.

The substrate clamping effect of 56/44 mol% P(VDF-TrFE) copolymers irradiated with proton doses ranged from 10 to 50 Mrad films was investigated. The effective $M_{33}$ of copolymer spin-coated on the substrate shows an order of magnitude reduction compared with the free bulk thick film. At the centre of the freely vibrated membrane, the effective $M_{membrane}$ becomes higher than the $M_{Si}$ for P(VDF-TrFE) film on a Si substrate. This is because in the Si membrane, only a thin layer of Si substrate is left which greatly reduces the clamping on the soft copolymer film.

As the copolymer possesses a high degree of flexibility, with the use of a thin Si backing plate, it can generate a considerable displacement, especially at resonance. In this work, suspended membrane-type MEMS has been fabricated and studied. Micromachined piezoelectric 70/30 mol% P(VDF-TrFE) MEMS for air transducer application is reported. The mechanical behaviour of the MEMS has been analysed by means of a laser vibrometer. The resonance frequency and the amplitude of vibration depend on the membrane size and thickness. The larger and the thinner the membrane, the easier it is to drive the membrane and the lower the resonance frequency.

A copolymer MEMS transducer with 2.7 μm thick poled 70/30 mol% P(VDF-TrFE) as the transducer element has been fabricated and its performance evaluated. The membrane can be excited to vibrate effectively, showing a resonance frequency of 40.8 kHz. This is in agreement with the theoretical prediction. The vibrating displacement response at the centre of the membrane is reasonably high, showing a value of 110 nm/V at resonance. Both the transmitting and receiving responses of the MEMS transducer were studied. At resonance (40.8 kHz), the peak pressure level generated per volt is ~ 0.1 Pa/V at an axial distance of 13 mm. As a sensor, the MEMS can distinctly detect ultrasonic acoustic pressure at its resonance frequency without using any preamplifier and filter and the sensitivity of the MEMS at 40.8 kHz under different pressure is ~ 84 μV/Pa. The result suggested that the piezoelectric P(VDF-TrFE) has potential in actuator application and can monitor ultrasound emission.

# References

Bernstein, J., Houston, K., Niles, L., Finberg, S., Chen, H., Cross, L.E., Li, K. and Udayakumar, K. "Micromachined ferroelectric transducers for acoustic imaging". *International Conference on Solid State Sensors and Actuators (Transducers '97), Chicago, June 16-19*, pp. 421-424 (1997).

Bharti, V., Zhao, X.Z., Zhang, Q.M., Romotowski. T., Tito, F. and Ting, R. "Ultrahigh field induced strain and polarization response in electron irradiated poly(vinylidene fluoride-trifluoroethylene) copolymer". *Materials Research Innovations, 2*, pp. 57-63 (1998).

Cheeke, J.D.N. *Fundamentals and Applications of Ultrasonic Waves*. Montreal: CRC Press (2002).

Cheng, Z.Y., Bharti, V., Mai, T., Xu, T.B., Zhang, Q.M., Ramotowski, T., Wright, K.A. and Ting, R. "Effect of high energy electron irradiation on the electromechanical properties of poly(vinylidene fluoride-trifluoroethylene) 50/50 and 65/35 copolymers". *IEEE Transactions on Ultrasonics, Ferroelectrics, and Frequency Control, 47*(6), pp. 1296-1307 (2000).

Cheng, Z.Y., Bharti, V., Xu, T.B., Xu, H., Mai, T. and Zhang, Q.M. “Electrostrictive poly(vinylidene fluoride-trifluoroethylene) copolymers”. *Sensors and Actuators A*, 90, pp. 138-147 (2001).

Cheng, Z.Y., Zhang, Q.M. and Beteman, F.B. “Dielectric relaxation behaviour and its relation to microstructure in relaxor ferroelectric polymers: High-energy electron irradiated poly(vinylidene fluoride-trifluoroethylene) copolymers”. *Journal of Applied Physics*, *92*(11), pp. 6749-6755 (2002).

Cross, L.E. “Relaxor ferroelectrics: an overview”. *Ferroelectrics*, *151*, pp. 305-320 (1994).

Daudin,B., Legrand, J.F. and Macchi, F. “Microscopic and macroscopic effects of electron irradiation on ferroelectric poly(vinylidene fluoride-TrFe) copolymers”. *Journal of Applied Physics, 70*(8), pp. 4037-4044 (1991).

Davis, G.T., Furukawa, T., Lovinger, A.J. and Broadhurst, M.G. “Structural and dielectric investigation on the nature of the transition in a copolymer of vinylidene fluoride and trifluoroethylene (52/48 mol%)”. *Macromolecules*, *15*, pp. 329-333 (1982).

Furukawa, T. “Ferroelectric properties of vinylidene fluoride copolymers”. *Phase Transition*, *18*, pp. 143-211 (1989).

Furukawa, T. and Seo, N. “Electrostriction as the origin of piezoelectricity in ferroelectric polymers”. *Japanese Journal of Applied Physics, 29*(4), pp. 675-680 (1990).

Glembocki, P., Palik, E.D., de Guel, G.R. and Kendall, D.L. “Hydration model for the molarity dependence of the etch rate of Si in aqueous alkali hydroxides”. *The Journal of the Electrochemical Society, 138*(4), pp. 1055 (1991).

Harrison, J.S. and Ounaies, Z. “Piezoelectric polymers”. *ICASE Report No. 2001-43* (2001).

Hsieh, W.H., Hsu, T.Y. and Tai, Y.C. “A micromachined thin-film teflon electret microphone”. *Proc. Intl. Conf. on Solid State Sensors and Actuators (Transducers ’97)*, Chicago, IL, June 16-19, pp. 425-428 (1997).

Ito, Y. and Uchino, K. “Piezoelectricity”. In Webster, J.G. ed. *Wiley Encyclopedia of Electrical and Electronics Engineering*. New York: John Wiley & Sons (1999).

Jones, D.J., Prasad, S.E. and Wallace, J.B. “Piezoelectric materials and their applications”. *Key Engineering Materials, 122-124*, pp. 71-144 (1996).

Kälvesten, E., Löfdahl, L. and Stemme, G. “Small piezoresistive silicon microphones specially designed for the characterization of turbulent gas flows”. *Sensors and Actuators A, 46-47*, pp. 151-155 (1995).

Kawai, H. “The piezoelectricity of poly(vinylidene fluoride)”. *Japanese Journal of Applied Physics, 8,* pp. 975-976 (1969).

Kendall, D.L. and Shoultz, R.A. “Wet chemical etching of silicon and $SiO_2$, and ten challenges of micromachiners”. In: Rai-Choudhury, P. editor. *Handbook of Microlithography, Micromaching, and Microfabrication Volume 2: Micromachining and Microfabrication*, SPIE Optical Engineering Press, pp. 41-97 (1997).

Kim, T.M. “Influence of substrate on the elastic reaction of films for the microindentation tests”. *Thin Solid Films, 283* pp. 12-16 (1996).

Ko, S.C., Kim, Y.C., Lee, S.S., Choi, S.H. and Kim, S.R. “Micromachined piezoelectric membrane acoustic device”. *Sensors and Actuators A, 103*, pp. 130-134 (2003).

Kronast, W., Müller, B., Siedel, W. and Stoffel, A. “Single-chip condenser microphone using porous silicon as sacrificial layer for the air gap”. *Sensors and Actuators A, 87*, pp. 188-193 (2001).

Lando, J.B. and Doll, W.W. "The polymorphism of polyvinylidene fluoride 1. The effect of head-to-head structure". *Journal of Macromolecular Science: Physics, B2*, pp. 205 (1968).

Lau, S.T., Leung, K.Y., Chan, H.L.W., Choy, C.L., Sundravel, B. and Wilson, I. "Effects of proton irradiation on the structure and properties of poly(vinylidene fluoride-trifluoroethylene) 80/20 mol.% copolymer". *Ferroelectrics, 273*, pp. 9-14 (2002).

Lau, S.T., Chan, H.L.W. and Choy, C.L. "Structural and property changes in poly(vinylidene fluoride-trifluoroethylene) 70/30 mol% copolymer induced by proton irradiation". *Applied Physics A: Materials Science and Processing, 80*(2), pp. 289-294 (2003).

Lau, S.T. *Study of Proton-Irradiated Poly(vinylidene fluoride-trifluoroethylene) Copolymers*. Thesis of Degree of Doctor of Philosophy, The Hong Kong Polytechnic University (2004).

Lau, S.T., Chan, H.L.W. and Choy, C.L. "Study of the structure and electrostrictive property of proton irradiated P(VDF-TrFE) 56/44 mol% copolymer". *IEEE Transactions on Dielectrics and Electrical Insulation, 11*(2), pp. 210-217 (2004).

Legrand, J.F., Daudin, B. and Bellet-Amalric, E. “Dipolar glass behaviour of a ferroelectric polymer after irradiation”. *Nuclear Instruments and Methods in Physics Research B, 105*, pp. 225-228 (1995).

Lovinger A.J. “Polymorphic transformations in ferroelectric copolymers of vinylidene fluoride induced by electron-irradiation”. *Macromolecules, 18*, pp. 910-918 (1985).

Ma, W.H. and Cross, L.E. “Tunable electric-field-induced piezoelectricity in high strain relaxor ferroelectric P(VDF-TrFE) copolymer”. *Journal of Physics: Condensed Matter, 17*, pp. 1101-1018 (2005).

Manthey, W., Kroemer, N. and Mágorl, V. “Ultrasonic transducers and transducer arrays for applications in air”. Measurement Science and Technology, 3, pp. 249-261, (1992).

Newnham, R.E., Sundar, V., Yimnirun, R., Su, J. and Zhang, Q.M. “Electrostriction: nonlinear electromechanical coupling in solid dielectrics”. *Journal of Physical Chemistry B, 101*, pp. 10141-10150 (1997).

Ohigashi, H., Koga, K., Suzuki, M., Nakanishi, T., Kimura, K. and Hashimoto, N. “Piezoelectric and ferroelectric properties of P(VDF-TrFE) copolymers and their application to ultrasonic transducers”. *Ferroelectrics, 60*, pp. 263-276 (1984).

Petersen, K.E. “Silicon as a mechanical material”. *Proceedings of the IEEE, 70*(5), pp. 420-457 (1982).

Reed, M. L. and Fedder, G. K. “Photolithographic microfabrication”. In: Fukuda, T. and Menz, W. editors. *Handbook of Sensors and Actuators Volume 6: Micro Mechanical Systems Principles and Technology*, Elsevier, pp. 13-61 (2001).

Rossing, T.D. and Fletcher, N.H. *Vibration and Sound*. New York: Springer-Verlag (1995)

Sawyer, C.B. and Tower, C.H. “Rochelle salt as a dielectric”. *Physical Review, 35,* pp. 269-275 (1930).

Schellin, R., Heb, G., Krebmann, R. and Wabmuth, P. “Micromachined silicon subminiature microphones with piezoelectric P(VDF-TrFE)-layers and silicon-nitride-membranes”. *Proceedings of 8th International Symposium on Electrets (ISE 8), 7-9 September 1994*, pp. 1004-1009 (1994).

Setter, N. ed. *Piezoelectric Materials in Devices: Extended Reviews on Current and Emerging Piezoelectric Materials, Technology and Applications.* Lausanne: Ceramic Laboratory, EPFL (2002).

Stemme, G. "Resonant silicon sensors". *Journal of Micromechanics and Microengineering*, *1*, pp. 113-125 (1991).

Tang, Y., Zhao X.Z., Chan, H.L.W. and Choy, C.L. "Effect of electron irradiation on poly(vinylidene fluoride-trifluoroethylene) copolymers". *Applied Physics Letters*, *77*(11), pp. 1713-1715 (2000).

Tanska, H., Yukawa, H. and Nishi, T. "Effect of crystallization condition on the ferroelectric phase transition in vinylidene fluoride/trifluoroethylene ($VF_2/F_3E$) copolymers". *Macromolecules*, *21*(8), pp.2469-2474 (1987).

Tashiro, K., Tadokoro, H. and Kobayashi, M. "Structure and piezoelectricity of poly(vinylidene fluoride)". *Ferroelectrics*, *32*, pp. 167 (1981).

Tashiro, K., Takano, K., Kobayashi, M., Chatani, Y. and Tadokoro, H. "Structure and ferroelectric phase transition of vinylidene fluoride-trifluoroethylene copolymers: 2.VDF 55% copolymer". *Polymer*, *25*, pp. 195-208 (1983).

Viehland, D., Jang, S.J. and Cross, L.E. "Freezing of the polarization fluctuations in lead magnesium niobate relaxors". *Journal of Applied Physics*, *68*(6), pp. 2916-2921 (1990).

Wang, H., Zhang, Q.M. and Cross, L.E. “Piezoelectric, dielectric and elastic properties of poly(vinylidene fluoride/trifluoroethylene)”. *Journal of Applied Physics, 74*, pp. 3394-3398 (1993).

Welter, C., Faria, L.O and Moreira, R.L. “Relaxor ferroelectric behavior of g-irradiated poly(vinylidene fluoride-trifluoroethylene) copolymers”. *Physical Review B, 67*, pp. 144103 (2003).

Xu, F., Chu, F. and Trolier-Mckinstry, S. “Longitudinal piezoelectric coefficient measurement for bulk ceramics and thin films using pneumatic pressure rig”, *Journal of Applied Physics*, *86*(1), pp. 588-594 (1999).

Yagi, T., Tatemoto, M. and Sako, J. “Transition behavior and dielectric properties in trifluoroethylene and vinylidene fluoride co-polymers”. *Polymer Journal*, *12*, pp. 209 (1980).

Zhang, Q.M., Bharti, V. and Zhao, X. “Giant electrostriction and relaxor ferroelectric behavior in electron-irradiated poly(vinylidene fluoride-trifluoroethylene) copolymer”. *Science, 280*, pp. 2101-2104 (1998).

Ziegler, J.F. *The Stopping and Range of Ions in Solids*. New York: Pergamon, (1985).